UC Irvine
UC Irvine Electronic Theses and Dissertations

Title

An investigation of the diffusive resistance to air/sea gas transfer: Eddy flux measurements of soluble trace gases

Permalink

https://escholarship.org/uc/item/2b7709hd

Author

Porter, Jack Gordon

Publication Date

2018

Peer reviewed|Thesis/dissertation

UNIVERSITY OF CALIFORNIA,
IRVINE

An investigation of the diffusive resistance to air/sea gas transfer: Eddy flux measurements
of soluble trace gases

DISSERTATION

submitted in partial satisfaction of the requirements
for the degree of

DOCTOR OF PHILOSOPHY

in Chemistry

by

Jack Gordon Porter

Dissertation Committee:
Professor Eric Saltzman, Chair
Professor Annmarie Carlton
Professor Sergey Nizkorodov

2018

DEDICATION

To

My mother and father,

for giving me the opportunity to make my life extraordinary

The powerful play goes on and you may contribute a verse

Walt Whitman
"O me! O Life!"

TABLE OF CONTENTS

LIST OF FIGURES

LIST OF TABLES

ACKNOWLEDGMENTS

CURRICULUM VITAE

Jack Porter

Phone: 510-258-8574   1212 Croul Hall
jgporter@uci.edu   Irvine, CA 92697

Education	**PhD University of California, Irvine**, Atmospheric Chemistry, 2012-2018 Advisor: Dr. Eric S. Saltzman Research topic: Eddy covariance flux measurements of soluble trace gases in the marine surface layer **BS University of California Irvine**, Chemistry, Earth Systems Science, 2011
Honors and Awards	**American Chemical Society Undergraduate Award for Analytical Chemistry 2011**
Research Experience	**Graduate Student Researcher** • Develop instrumentation and methodology related to eddy covariance flux measurements • Deploy instrumentation in the field for extended periods of time (Ships/Piers) • Data analysis (Matlab) • Manuscript preparation
Teaching Experience	**Teaching Assistant**, University of California, Irvine • Chemistry 1A, General Chemistry Discussion, Fall 2012 • Chemistry 1LC, General Chemistry Lab, Winter & Spring 2013

Field Experience	**Scripps Pier** *La Jolla, CA* April 6th – April 27th (2014) Pier based eddy covariance flux measurements
	Field Research Facility *Duck, NC* March 19th – April 21st (2015) Pier based eddy covariance measurements
	North Atlantic Aerosol and Marine Ecosystems Study (NAAMES), *North Atlantic* Nov 6th -Dec 1st (2015): May 11th – June 5th (2016) Ship based eddy covariance flux measurements of DMS, acetone, water vapor, sensible heat
Publications	**Porter, J. G.,** De Bruyn, W., Miller, S. D. Saltzman, E. S. (2018). Eddy flux measurements of sulfur dioxide deposition to the sea surface: (*Manuscript in Preparation)*
	Porter, J. G., Bell, T. G., De Bruyn, W., Saltzman E. S. (2018). Eddy covariance flux measurements of acetone in the North Atlantic (*Manuscript in Preparation)*
	Sanchez K.J., Chen C., Russell L.M., Bertha R., Liu J., Price D. J., Massoli P., Ziemba L. D., Crosbie E. C., Moore R. H., Muller M., Schiller S. A., Wisthaler A. K., Lee A. K. Y., Quinn P. K., Bates T. S., **Porter J.,** Bell T. G., Saltzman E. S., Vaillancourt R. D., Behrenfeld M.J. Substantial Seasonal Contribution of Observed Biogenic Sulfate Particles to Cloud Condensation Nuclei. *Nature*. 2018;(November 2017):1-14. doi:10.1038/s41598-018-21590-9.
Poster Presentations	NASA NAAMES May Meeting, Langley Research Center, Hampton, VA, *"What Variables Control Acetone Seawater Concentrations in the North Atlantic"* May 2017.
	Science Workshop IFREMER, Brest, France *"Eddy covariance flux of sulfur dioxide to the sea surface: Air-side resistance of a highly soluble gas.* September 2016
	NASA NAAMES August Meeting, Oregon State University, Corvallis, OR, *"Sea-water and Atmospheric Acetone and DMS Measurements during May NAAMES Cruise"*. August 2016

AGU Fall Meeting, San Francisco, CA, "*Eddy covariance flux measurements of sulfur dioxide to the sea surface: Air-side resistance of a highly soluble gas*", presenter December 2014.

ABSTRACT OF THE DISSERTATION

An investigation of the diffusive resistance to air/sea gas transfer: Eddy flux measurements
of soluble trace gases

By

Jack Gordon Porter

Doctor of Philosophy in Chemistry

University of California, Irvine, 2018

Professor Eric Saltzman, Chair

The deposition of soluble gases to the sea surface is physical process that impacts the

biogeochemical cycling of sulfur, carbon, nitrogen, phosphorus and latent and sensible

heat. Soluble atmospheric gases such as SO_2, nitric acid and ammonia play key roles in

global climate and air quality through their influence on aerosol and cloud formation, and

tropospheric photochemistry. Direct air/sea flux measurements of soluble trace gases are

rare and most of what we know stems from studies of latent and sensible heat. Lack of

fundamental understanding of the physical controls of air/sea deposition of soluble gases

limits the accuracy of models simulating some global biogeochemical cycles.

This study involved direct flux measurements of SO_2, water vapor, sensible heat and

momentum from the atmosphere to the sea surface. These measurements were done at

piers located in San Diego, CA and Duck, NC. The goal of the study is to gain insight into the

physical controls on soluble trace gas fluxes by comparing these measurements to each

other and to various air/sea flux numerical parameterizations. The results of this analysis

demonstrate that SO_2 flux measurements are a viable approach to studying the physics of

soluble trace gas flux over the ocean. Furthermore, the results show the transfer velocity of

SO$_2$ is ~ 20 % lower than that of water vapor. This reduction is attributed to resistance to gas transfer due to diffusion in the interfacial layer immediately above the sea surface. This study represents the first ever in situ measurement of diffusive resistance in the interfacial layer. The magnitude of diffusive resistance calculated from these measurements is ~ 18 % larger than the current gas transfer parameterizations (Fairall *et al.,* 2000).

1. Introduction

1.1. Overview

Statement of the problem and approach

Deposition to the oceans is a major removal mechanism for soluble trace gases such as sulfur dioxide, volatile organic compounds (VOCs), ammonia and nitric acid. These gases are involved in multiple physical and chemical processes that affect climate, air quality and human health. Sulfur compounds in the atmosphere influence aerosol and cloud formation by acting as precursors for cloud condensation nuclei and contributing to particle growth (Charlson *et al.*, 1987). Clouds and aerosols can directly influence the radiative balance of the earth by reflecting radiation. Volatile organic compounds are involved in multiple processes that affect tropospheric chemistry. For example, they control the oxidative capacity of the atmosphere by acting as a sink for OH radicals. Hydrocarbons are also pre-cursers to produce tropospheric ozone. Other highly soluble gases deposited to the sea surface include the important nitrogen-containing species ammonia and nitric acid. Nitric acid is a reactive nitrogen containing compound that contributes to particle growth. Ammonia is an inorganic nitrogen containing nutrient that is thought to affect biological activity in surface waters. Ammonia is also responsible for neutralizing acidic compounds in the troposphere. The deposition of ammonia and nitric acid to the ocean is significant loss term for reactive nitrogen compounds in the atmosphere.   Air/sea fluxes of heat and water vapor are also major terms in the energy balance of the earth. These processes play

a role in the climatology of the earth by affecting how energy is stored and distributed on the planet.

Air/sea fluxes are driven by the concentration differential between the bulk atmosphere and the sea surface and the physical processes transporting material to the air/sea interface. Transport to the air/sea interface is largely controlled by the physical conditions over the ocean such as wind speed and sea state. Making accurate estimates of air/sea flux is dependent on our ability to parameterize fluxes as a function of observable environmental conditions. Numerous parameterizations exist that attempt to predict fluxes based on observable environmental conditions however, the uncertainty and variance associated with the flux estimates of these models is large. The uncertainty associated with air/sea flux estimates is mostly due to a lack of understanding of the physical processes driving the deposition of gases to the sea surface. Flux measurements of soluble trace gases to the sea surface are rare which limits our understanding of the physical controls on trace gas fluxes as well as our ability to test and verify existing flux parametrizations.

In this study air/sea flux measurements of soluble trace gases are made using the eddy covariance technique. The measurements were made during two separate field deployments over the course of three years. The study sites include two coastal sites in North Carolina and San Diego. During the coastal studies simultaneous flux measurements of SO_2, water vapor, sensible heat and momentum were made. Meteorological conditions such as wind speed, sea-surface temperature, wave height and humidity were also measured. This dataset is unique because it includes both heat (latent and sensible) and

soluble trace gas (SO_2) flux measurements. These measurements are the first simultaneous flux measurements in the marine surface layer of multiple soluble gases with different diffusion coefficients. Comparing the fluxes of water vapor and SO_2 should give insight into the role of diffusion in controlling trace gas fluxes. Additionally, the data will allow us to test current flux parameterizations of soluble trace gas fluxes.

Organization of this thesis

Chapter 1 contains a statement of the research problem and experimental approach, followed by background information on the physical controls and modeling techniques of air/sea gas transfer. Chapter 2 is a detailed description of the methods used in this study, including a general discussion of the eddy covariance flux technique and the instrumentation used to make meteorological flux measurements. Chapters 3 and 4 describe field campaigns, including methodological details specific to each campaign and the resulting data. Chapter 5 is a comparison of the data from the two field campaigns where the major consistencies between the field campaigns are identified. Chapter 6 is discussion of various bulk parameterizations of transfer velocities including a comparison to experimental data. The final chapter (Chapter 7) identifies the major conclusions of the study, the impact of this work on the field of air/sea flux and what research questions are remaining.

1.2. Background

The marine surface layer

The marine surface layer is the lowermost region of the atmosphere which is in direct contact with the ocean surface. The surface layer is characterized by turbulent eddies that transport momentum, gases and energy through the atmosphere (Kaimal *et al.,* 1972). The height of the marine surface layer is roughly tens of meters, generally defined as the lowest 10 % of the atmospheric boundary layer. The vertical transfer of material and energy is considered constant throughout the surface layer. This assumption is justified because the height of the layer is small enough that horizontal divergence of gases is negligible. The vertical profile of mean horizontal wind speed and vertical mixing length follow logarithmic vertical profiles (Monin and Obukhuv, 1954). For example,

$$u(z) = \left(\frac{u_*}{\kappa}\right) \ln z/z_o \tag{1.1}$$

Where u is wind speed and z is the height above the air/sea interface and κ is Von Karman's constant, equal to 0.4 (Equation 1.1). The friction velocity, u_*, is defined as:

$$u_* = \sqrt{\tau/\rho} \tag{1.2}$$

where τ is momentum flux and ρ is air density. The z_o term is known as the roughness length and is a function of the roughness of the sea surface. Equation 1.1 is commonly known as the Law of the Wall (Von Karman, 1930).

Close to the interface the inertial turbulent mixing is damped, and molecular viscosity dominates. In this interfacial sublayer region, the flow is thought to be laminar and the velocity profile is linear with height as follows (Liu *et al.*, 1978):

$$u(z) = \left(\frac{\tau}{\mu}\right) z \qquad (1.3)$$

where τ is momentum flux and μ is the viscosity of air. Equation 1.3 is the definition of viscosity in a laminar fluid. The height of the interfacial layer is thought to be roughly 10 x the Kolmogorov scale (Equation 1.4).

$$z_{interfacial} = 10 \left(\frac{\nu}{u_*}\right) \qquad (1.4)$$

Figure 1.1 is a depiction of the wind shear in the surface and interfacial layers.
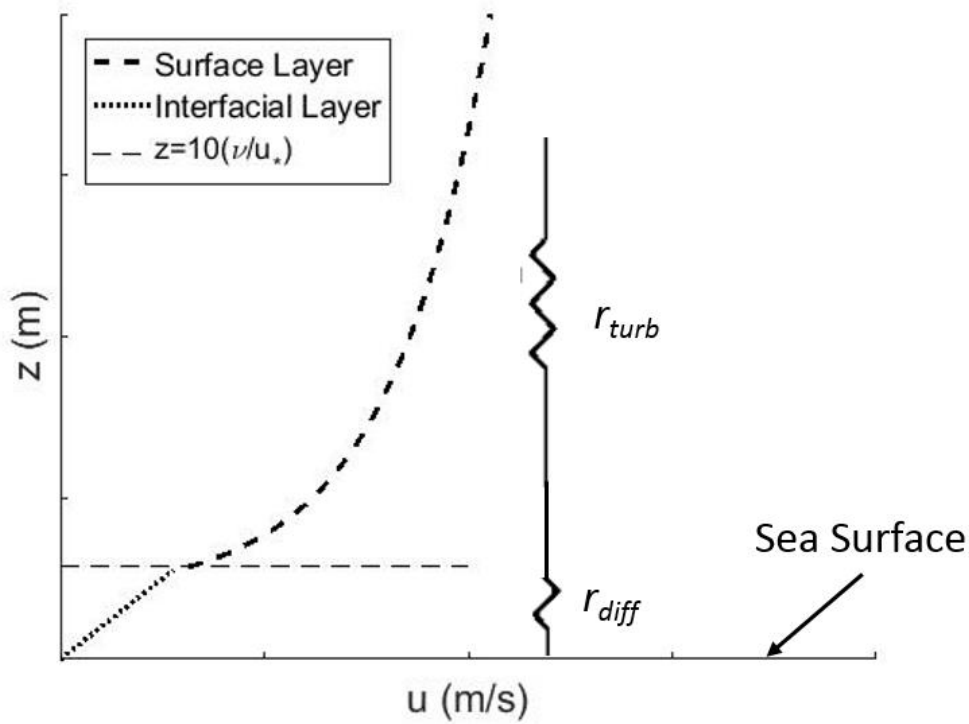
Figure 1.1 Cartoon illustrating the horizontal wind profile in the marine surface layer over the ocean. Close to the surface in the interfacial layer the profile is dominated by molecular viscosity and has a linear profile. Away from the surface the profile is dominated by turbulence and has a logarithmic profile. The resistance to gas transfer in each layer is depicted as two resistors connected in series.

Bulk transfer coefficients

The momentum flux at the surface is commonly parameterized using a bulk transfer coefficient (Equation 1.5):

$$\tau = C_d u_{10}^2 \rho \qquad (1.5)$$

Where u_{10} is the 10 m wind speed and C_d is a bulk transfer coefficient known as the drag coefficient. The drag coefficient over the ocean represents the frictional effect of waves on the transfer of momentum between the atmosphere and surface-ocean. The drag coefficient over the ocean has a wind speed dependence due to the increasing roughness of seas with increasing wind speed (Smith, 1988; Kondo, 1975; Hicks, 1972; Liu *et al.*, 1979, Pond *et al.*, 1973, Donelan *et al.*, 2004).

Bulk transfer coefficients can also be written for sensible and latent heat (due to water vapor flux), and trace gases, as follows:

$$H = C_H u_{10}(\Delta T) = k_H(\Delta T) \tag{1.6}$$

$$E = C_E u_{10}(\Delta q) = k_E(\Delta q) \tag{1.7}$$

$$F = C_{gas} u_{10}(\Delta C) = k_{gas}(\Delta C) \tag{1.8}$$

Where *H*, *E*, and *F* are fluxes of heat, water vapor, and a soluble trace gas, and the *Δ quantities* represent the differential in temperature, water vapor, and trace gas concentration between a reference height (10 m) and the surface. The quantity *k* is known as the transfer velocity and is defined as the product of the transfer coefficient and 10 m wind speed. These fluxes are dependent on: (1) The physical transport through the surface and interfacial layers, represented by the bulk transfer coefficient and wind speed and (2) the air/sea thermodynamic differential. The thermodynamic differential in this case is defined as the temperature and gas concentration differential at 10 m and the sea surface.

The transfer of gases and heat differ slightly from that of momentum in the interfacial layer. In the surface layer gases, heat and momentum are all transferred by turbulent mixing at the same rate. In the interfacial layer, gases and heat must diffuse to reach the interface, while momentum can be transferred through viscous stress and pressure gradients. As a result: (1) The drag coefficient probably represents an upper-limit to the transfer coefficients of other scalars and (2) the transfer coefficients of heat and gases are dependent on diffusion and thus should vary with the diffusion coefficient of a gas.

The concept of resistance to gas transfer and the role of gas solubility

The concept of "resistance to gas transfer" uses the analogy of electrical resistance to represent the influence of turbulent and diffusive transport properties of the surface layer. Resistance is defined as the inverse of the transfer velocity, and the turbulent and diffusive processes limiting mass transfer are treated as resistors connected in series, as follows:

$$k^{-1} = r_{total} = r_{turb} + r_{diff} \tag{1.9}$$

(Figure 1.1), where k is the transfer velocity, r_{turb} is the turbulent resistance and r_{diff} is the diffusive resistance. Because turbulence transports both momentum and mass, the turbulent resistance term is sometimes represented by the drag coefficient (Equation 1.10).

$$C_d u_{10} = k_{mom} = (r_{turb})^{-1} \tag{1.10}$$

The transfer velocity for a gas is then given by Equation 1.11.

$$k^{-1} = \frac{1}{C_d u} + r_{diff} \qquad (1.11)$$

On the atmospheric side of the interface, diffusive resistance is significantly smaller than turbulent resistance. On the water side of the interface, the reverse is true. The solubility of a gas determines the relative magnitude of the air-side and liquid side resistance to transfer.

Liss (1974) used a simple two-layer model to illustrate the effect of solubility on gas transfer. The two-layer model consists of well-mixed bulk air and water layers away from the interface, with gas concentrations C_a and C_w (Figure 1.2). Just above and below the air/sea interface there are air-side and water-side diffusive sublayers. At the interface itself, the air side and water side gas concentrations are assumed to be in Henry's Law equilibrium.
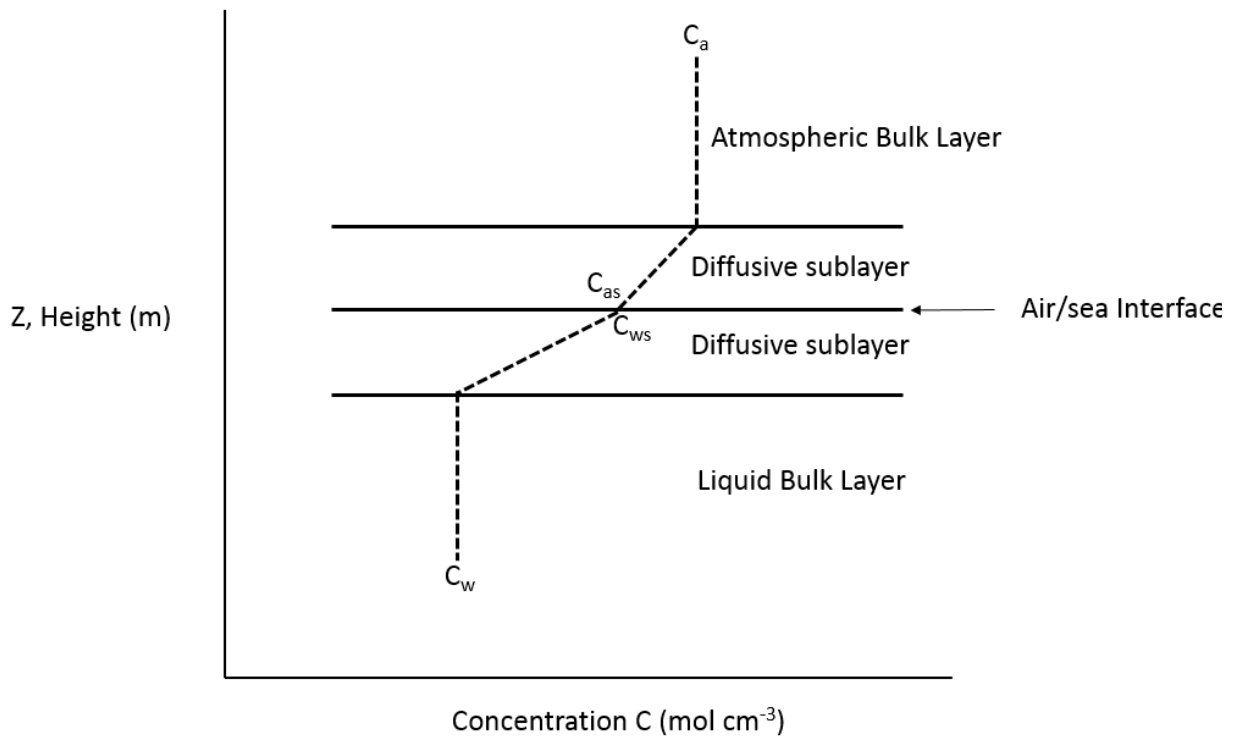
Figure 1.2 Schematic of bulk and diffusive layers in the atmospheric and liquid side if the interface. The dashed line represents a concentration profile through the layers.

If there are no additional sources or losses of the gas within these layers, then the air/sea gas flux is constant across all the layers and the following expression holds:

$$F = k_a(C_a - C_{as}) = k_w(C_{ws} - C_w) \tag{1.12}$$

$$C_{as} = \frac{C_{ws}}{H} \tag{1.13}$$

where k_a and k_w are the air-side and liquid-side transfer velocities respectively, and H is the dimensionless Henry's law constant for gas solubility expressed here as the ratio of liquid-

side to air-side concentrations. Eliminating C_{as} and C_{ws} between Equations 1.12 and 1.13 yields,

$$F = K_a(C_a - \frac{C_w}{H}) \qquad (1.14)$$

$$\frac{1}{K_a} = \left(\frac{1}{k_a} + \frac{1}{k_w H}\right) = R_{total} = (r_a + r_w) \qquad (1.15)$$

where K_a is the total transfer velocity expressed in gas side units. Equation 1.15 implies that the total resistance to gas transfer is composed of water-side and air-side terms and the strength of the liquid side resistance decreases with increasing solubility. The effect of solubility on the relative importance of air-side and liquid-side resistance is shown in Table 1.1. for gases spanning a wide range of solubilities. Air-side and water-side gas transfer velocities were calculated using the gas transfer model from Fairall *et al.* (2000). The gas, liquid and total resistance were calculated by inserting transfer velocities and the Henry's law constant into Equation 1.15. The results are summarized in Table 1.1.

Table 1.1 Table showing the effect of solubility on the resistance to gas transfer on the liquid and gas side of the interface. All Henry's law constants are given at 298.15 °K (Sander 1999).

Compound	H	R_{total} (s m^{-1})	r_a (s m^{-1})	r_w (s m^{-1})	R_g/R_{total} (%)
O_2	0.03	2.1×10^5	83	2.1×10^5	0.3 %
Dimethylsulfide	13.7	1.2×10^3	95	1.1×10^3	8 %
Methanol	5.4×10^3	93	89	3.7	96 %
SO_2	2.5×10^8	91	91	8.2×10^{-5}	100 %

Use of SO₂ as a tracer for air-side gas transfer

In this study sulfur dioxide was utilized to study air-side gas transfer velocities. This is done by computing transfer coefficients from observations of air/sea fluxes and air/sea concentration differences, as follows:

$$K_a = \frac{F}{(C_a - \frac{C_w}{H})} \tag{1.16}$$

Sulfur dioxide has several physical/chemical properties that make it useful as a tracer for the processes controlling air side resistance to air/sea gas transfer. The first of these is very high effective solubility. Sulfur dioxide is highly soluble because of rapid dissociation into bisulfite and sulfite ion (HSO_3^-; SO_3^{2-}). These equilibria are described below, with equilibrium constants given for seawater at 298 K (Millero *et al.*, 1989).

$$SO_2(g) \leftrightarrow SO_2 \cdot H_2O \quad H_{SO2} = \frac{[SO_2 \cdot H_2O]}{P_{SO2}} = 1.24 \; M atm^{-1} \tag{1.16}$$

$$SO_2 \cdot H_2O \leftrightarrow HSO_3^- + H^+ \quad K_1 = \frac{[HSO_3^-][H^+]}{[SO_2 \cdot H_2O]} = 2.6 \times 10^{-2} \; M \tag{1.18}$$

$$HSO_3^- \leftrightarrow SO_3^{2-} + H^+ \quad K_2 = \frac{[SO_3^{2-}][H^+]}{HSO_3^-} = 7.4 \times 10^{-7} \; M \tag{1.19}$$
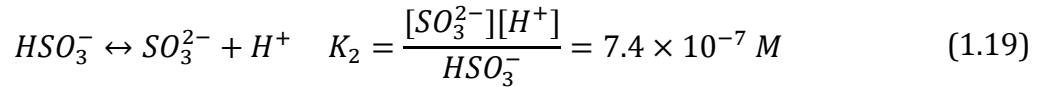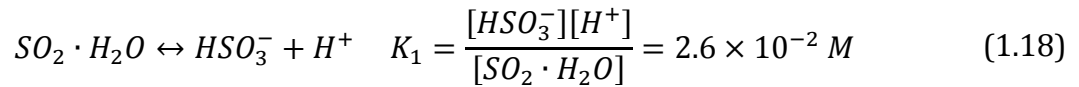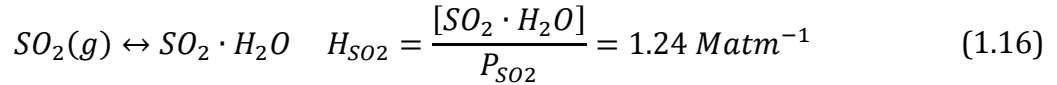
Combining these equilibria and assuming a pH of 8.1 yields an effective SO₂ solubility, as follows:

$$H_{eff} = H_{SO2} \left[1 + \frac{K_1}{[H^+]} + \frac{K_1 K_2}{[H^+]^2} \right] \cdot RT \sim 2.5 \times 10^8 \tag{1.20}$$

12

where H_{SO2} is the Henry's law solubility, K_1 and K_2 are equilibrium constants, R is the gas

constant and T is temperature. This effective solubility of SO_2 is so large that the resistance

to air/sea gas exchange is entirely on the air side of the interface and $k_a=K_a$ (Table 1.1).

In order for the effective solubility to influence gas transfer, the kinetics of ionization must

occur on a time scale significantly shorter than the characteristic time for transport across

the water side diffusive layer (Hoover and Berkshire, 1969). The characteristic time for

equilibration of SO_2 with its ionic forms is roughly 4.5×10^{-4} s (Schwartz & Frieberg, 1981),

while the time scale for diffusive transport on the water side is on the order of seconds.

Another important property of S(IV) is that it undergoes rapid oxidation in seawater. As a

result, it is expected that the levels of S(IV) in the surface ocean are extremely low. Clark &

Radojevic (1984) measured the oxidation rate of S(IV) in seawater, and obtained the

following rate expression:

$$\frac{d[S(IV)]}{dt} = (k_{ox})[S(IV)]^2 \tag{1.21}$$

Where k_{ox} is the S(IV) oxidation rate constant and [S(IV)] is the molar concentration of

S(IV) in seawater. We can estimate the levels of S(IV) in seawater using a simple steady

state box model. Two sources of S(IV) were considered, 1) sulfur dioxide deposition to the

sea surface from the atmosphere, (F_{SO2}) and 2) oxidation of hydrogen sulfide released from

marine sediments, (P_{H2S}). The loss term is the oxidation rate given in Equation 1.21. The

model equation is:

$$P_{H2S} + F_{SO2} = (k_{ox})[S(IV)]^2 \tag{1.22}$$

An upper limit for F_{SO2} was estimated using an atmospheric mixing ratio of 1 nmol mol^{-1} and an air-side transfer velocity of 0.02 m s^{-1}. Input from sulfate reduction in marine sediments was estimated assuming 10 mmol cm^{-2} year^{-1}, an upper bound on the range of global sulfate reduction rates (Bowles *et al.*, 2017).

Assuming a water depth of 10 m, a steady state S(IV) concentration was calculated to be ~0.05 μM. At equilibrium, this corresponds to an air-side mixing ratio of 5x10^{-3} pmol mol^{-1}. This is much lower than typical atmospheric SO$_2$ levels in the marine surface layer (De Bruyn *et al.* 2006; Bandy *et al.* 1992). As a result, the air sea concentration difference for SO$_2$ is entirely controlled by the air side concentration and when calculating k_a from SO$_2$ fluxes, Equation 1.23 holds.

$$k_a = \frac{F}{C_a} \tag{1.23}$$

By contrast, transfer velocities calculated from water vapor and heat flux data are dependent on measurements on both sides of the air/sea interface to estimate the air/sea thermodynamic differential.

Mass accommodation kinetics

An additional source of resistance is possible at the sea surface due to mass accommodation kinetics. This physical process describes the likelihood an SO$_2$ molecule that impacts the surface is transferred to the liquid phase. Worsnop *et al.* (1989) studied the uptake kinetics on water droplet surfaces. The result of this experiment indicate the mass accommodation coefficient of SO$_2$ is sufficiently large that the characteristic time to achieve equilibrium across the air/water interface is much smaller than the characteristic

time to diffusion to the water surface. This means any added resistance from mass accommodation kinetics is expected to be negligible compared to the total resistance to gas transfer in the marine boundary layer.

Bulk parameterizations

Numerous different expressions have been developed for the parameterization of bulk transfer coefficients for soluble gas deposition (Table 1.2; Johnson *et al.* 2010). Early parameterizations were empirical fits to flux measurements collected in a variety of ways (Liss, 1973; Hicks, 1972). More recent parameterizations include theoretical elements but still contain empirical constants to tune the models to agree with experimental results (Duce *et al.* 1991; Fairall *et al.* 2000).

Table 1.2 Commonly used equations for bulk parameterization of soluble trace gas transfer velocity (k).

Reference	k (m s^{-1})
Duce *et al.* (1991)	$\dfrac{u_*}{5Sc^{0.64} + C_d^{-0.5}}$
Fairall *et al.* (2000)	$\dfrac{u_*}{13.3Sc^{0.5} + C_d^{-0.5} - 5 + 1.25\log(Sc)}$
Mackay and Yeun (1983)	$10^{-3} + \dfrac{u_*}{21.65\,Sc^{\frac{2}{3}}}$
Shahin *et al.* (2002)	$10^{-2}D^{0.5}(0.98U_{10} + 1.26)$
Liss (1973)	$0.005 + 0.21U_{10}$

Diffusive resistance in bulk parameterizations is set proportional to the diffusion coefficient (D). Often the diffusion coefficient is expressed through the dimensionless

Schmidt number of a gas, defined as the kinematic viscosity divided by the diffusion coefficient, $Sc=v/D$. The strength of the diffusive resistance in bulk parameterizations depends on the theoretical framework the model is based on. The simple two-layer model assumes the interfacial layer is laminar with thickness related to the horizontal wind speed. This approach yields, $r_{diff} \propto D^1$ which follows from Fick's first law of diffusion (Liss and Salter, 1974). The interfacial layer is more accurately characterized as a laminar layer that episodically exchanges material with the overlying turbulent atmosphere (Higbie, 1935; Liu and Businger, 1975; Buckley and Vernon, 2016). Such models are referred to as surface renewal models and $r_{diff} \propto D^n$. There is little agreement among these models as to the value of n which typically varies from 0.5 – 0.66.

1.3. Previous soluble trace gas deposition measurements

There have been only three previous field studies of air-side controlled air/sea gas exchange of gases other than water vapor. Faloona *et al.* (2010) used eddy-covariance flux measurements of SO_2 from an aircraft in the marine boundary layer above the tropical Pacific Ocean. Transfer velocities were obtained from measurements at altitudes between 30 – 50 m and covered a wind speed range of 4.5 – 10 ms^{-1}. The transfer velocities measured in Faloona et al., (2010) were 30 % lower than predicted by the model of Fairall *et al.* (2000). The authors suggested that diffusive resistance in the Fairall *et al.* (2000) model was underestimated. Agreement with the model was obtained by increasing the thickness of the near surface diffusive layer in the model roughly 2-fold. Parameterization of the diffusive layer in air/sea gas transfer models is discussed in more detail in Chapter 6.

Marandino *et al.* (2005) made shipboard measurements of fluxes and air/sea concentrations of acetone in the Pacific. Acetone fluxes measured in this study were always negative (into the ocean). The unidirectional fluxes in this study were inconsistent with measured air/sea concentration differentials for a significant portion of the cruise. A linear relationship between fluxes, wind speed and atmospheric acetone concentration was apparent in the data. This result suggest that fluxes were independent of bulk seawater concentrations. The authors suggest that strong near-surface concentration gradients of acetone due to microbial activity may be responsible for the inconsistent results. The author notes that any conclusions about transfer coefficients or global acetone budgets drawn from this study are highly questionable considering the inconsistent results.

Yang *et al.* (2013) carried out a shipboard study of air/sea exchange of methanol in the Atlantic Ocean. They made eddy covariance flux measurements of methanol, heat and momentum and near surface seawater concentration measurements. Methanol transfer velocities from this experiment were larger than momentum transfer velocities at high wind speeds, which is physically implausible due to the additional resistance due to interfacial diffusion. The authors showed that better agreement between methanol and momentum transfer coefficients was obtained by assuming that seawater concentrations of methanol were negligible, implying that there must be strong near-surface gradients in methanol. This result was similar to the conclusion reached by Marandino *et al.* (2005).

The momentum and methanol transfer velocities derived from this study were used to calculate diffusive resistance to methanol transfer following equations 1.9-1.10. This

analysis suggested that the diffusive resistance is smaller than the parameterization in Fairall *et al.* (2000) but larger than that of Duce *et al.* (1991).

These three studies comprise the total body of literature focusing on in situ soluble trace gas flux measurements over the ocean which means there is an extremely limited amount of useful information for investigating air-side controlled trace gas fluxes. These studies were the first of their kind and provided insight into aspects of soluble trace gas fluxes were previously there was none. However, the results of these studies were highly questionable, raising more questions than providing answers.

1.4. Goals of this thesis

The flux measurements of SO_2, momentum and latent and sensible heat made in this study will increase our understanding of the physical processes in the surface and interfacial layers driving soluble gas flux. The transfer velocities from latent and sensible heat can be compared to the transfer velocities of trace gases. This comparison is rarely possible and should demonstrate that trace gases are controlled by the same physical processes that drive air/sea energy fluxes. The comparison between transfer velocities of multiple gases collected simultaneously should demonstrate the role of diffusive resistance in the interfacial layer. Bulk parameterizations can also be tested using this data. Specifically, the data can be used to evaluate the diffusive resistance term in bulk parameterizations.

2. Methodology

2.1. Overview of methodology

Introduction

Two pier-based flux studies were conducted in San Diego, CA and in Duck, NC. This Chapter describes the methods used in this study to measure coastal air/sea fluxes of momentum, water vapor, sensible heat and sulfur dioxide, as well as the bulk meteorological conditions and thermodynamic gradients driving the fluxes. The general configuration of the field setup, the sensors, data acquisition, and data analysis procedures are discussed. The chemical ionization mass spectrometric methods and instrumentation used for sulfur dioxide detection are discussed in particular detail, because these were novel aspects of this study that have not previously been used in ground-based flux studies. Details of the experimental set-up specific to each field deployment are given in chapters 3-4.

General experimental set-up

The coastal flux studies involved installing an eddy flux system at the end of a pier (Figure 2.1). The sensors and air inlets were mounted facing towards the ocean. Instrumentation for sulfur dioxide detection, data acquisition, clean air generator, and pumps were located in a shed at the end of the pier. Meteorological sensors were mounted to a boom that extended out over the water surface to avoid flow distortion from the pier. The sensing regions of the eddy covariance flux package and the air intake for chemical measurements were located roughly 10 m above the sea surface at the two sites.

In the Duck campaign, a downward-looking infrared sensor for sea surface temperature was

mounted below the eddy flux package, roughly 7 m above the water surface.
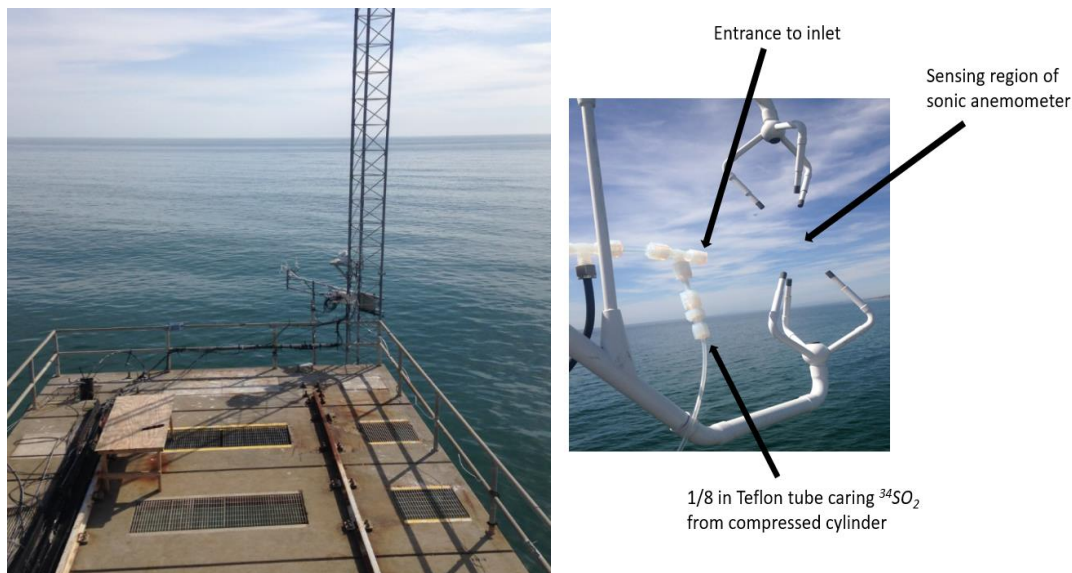
Figure 2.1. Left-Photo of the end of the Pier in Duck, NC where an aluminum arm extends 3 m out over the water surface. The sonic anemometer and IRGA attached to the end of the arm. Right-Location of inlet relative to sensing region of the Sonic Anemometer. The 1/8th in tubing carries the $^{34}SO_2$ standard from the compressed tank located in the shed.

Meteorological and oceanographic sensors

This section describes the various sensors used to make meteorological measurements

during the field campaigns in San Diego and North Carolina (Table 2.1). Wind

measurements in this study were made using a Campbell CSAT 3 sonic anemometer. This

instrument can make measurements of wind speed in 3 dimensions and air temperature at

50 Hz. Water vapor and air density measurements were made with an open-path infrared

gas analyzer (IRGA) at 5 Hz (LICOR model LI-7500). The instrument was calibrated using a

dew point generator (LICOR model LI-610). Low frequency measurements of air

temperature and relative humidity were measured with a capacitive/resistive probe

20

(Viasala Model HMP45) during the field campaign in North Carolina. Sea surface

temperatures were measured in North Carolina with a downward-looking infrared

radiometer (Apogee model SI-111) mounted ~ 2 m below the flux package. Sea surface

temperature measurements were measured in San Diego using a temperature probe chain

maintained by the Coastal Observing Research and Development Center

(http://cordc.ucsd.edu).

The IRGA and sonic anemometer were mounted to the end of the boom/arm. The sonic

anemometer was oriented facing out to sea and the IRGA was oriented just behind and to

the side of the sonic anemometer by roughly 20 cm to avoid flow distortion in the

oncoming winds but minimize distance from the sensing region of the sonic anemometer.

In Duck the infrared radiometer was attached to a 2 m aluminum arm that extended down

toward the sea surface. The temperature/RH sensor was housed in a radiation shield and

attached to the meteorological tower at the same height as the sonic and IRGA.

Table 2.1 Instrumentation used in this study for eddy covariance flux measurements and bulk gradients of momentum, water vapor, and sensible heat. LOD indicates limit of detection.

Parameter	Instrument	Model	Frequency Hz^{-1}	LOD
Water vapor	Infrared Gas Analyzer	LICOR 7500	5	300 (mmol m^{-3})
Wind speed, air temp.	Sonic Anemometer	Campbell CSAT3	30	15 (mm s^{-1}), -50 (°C)
Sea surface temp.	Infrared Radiometer	Apogee SI-111	1	-55 (°C)
Air Temp. and humidity	Temp./Humidity Probe	Viasala HMP45	0.1	-39.2 (°C), 0.8 (%RH)
SO$_2$	CIMS	Custom	10	4 (pmol mol^{-1})

2.2. SO$_2$ Detection

This section describes the instrumentation, calibration and flow set-up used to measure SO$_2$ mixing ratios during the coastal field campaigns.

Description of the chemical ionization mass spectrometer

Atmospheric sulfur dioxide mixing ratios were measured using a custom chemical ionization mass spectrometer (CIMS) developed and built in our laboratory (Figure 2.2). The CIMS instrument consists of an ionization region, an ion focusing region and two high vacuum regions. The ionization region consists of a ¼ inch glass lined steel tube which contains a ^{63}Ni foil. A pinhole (~250 μm) separates the ionization region from the ion focusing region containing an ion funnel.

The ion funnel is designed to increase ion transmission efficiency from the ambient pressure ionization region to the vacuum region of the instrument (Kelly *et al.*, 2011). The ion funnel is 127 mm long and consists of 100 concentric rings decreasing in diameter from 25.4 mm to 1.5 mm. A DC gradient of 3 Vcm^{-1} was applied to transmit ions axially and two phases of RF (2MHz, 150V p-p) were applied so that adjacent rings in the funnel were 180° out of phase. The result of this configuration is an effective potential in the funnel that increases radially outward from the center axis of the funnel. Ions can be radially focused at relatively high pressures (~1 Torr) by decreasing the diameter of the rings down the funnel.

The first high vacuum region contains three ion focusing lenses just prior to the entrance to an Extrel 19 mm diameter quadrupole. The second vacuum region contains a dynode and counting ion multiplier maintained at 4 and -2 kV respectively. Vacuum is maintained in the first and second vacuum regions by Varian 1001 and 700 turbo molecular pumps backed by an Edwards 28 vacuum pump.

DC voltages for the lenses and ion funnel were provided by a Gamma custom multichannel DC supply source. The quadrupole was driven by a Gamma QPS500 DC/RF power supply and the dynode and CEM were powered by a Gamma high voltage power supply (model number D-RR5-0.5R/SDPM/M772).

Collision Region
Ion funnel
0.7Torr

Entrance to quad
3×10^{-4}Torr

Detection Region
dynode and multiplier
4×10^{-6}Torr

Turbo Pumps

Ionization Region
430Torr

Rough Pump
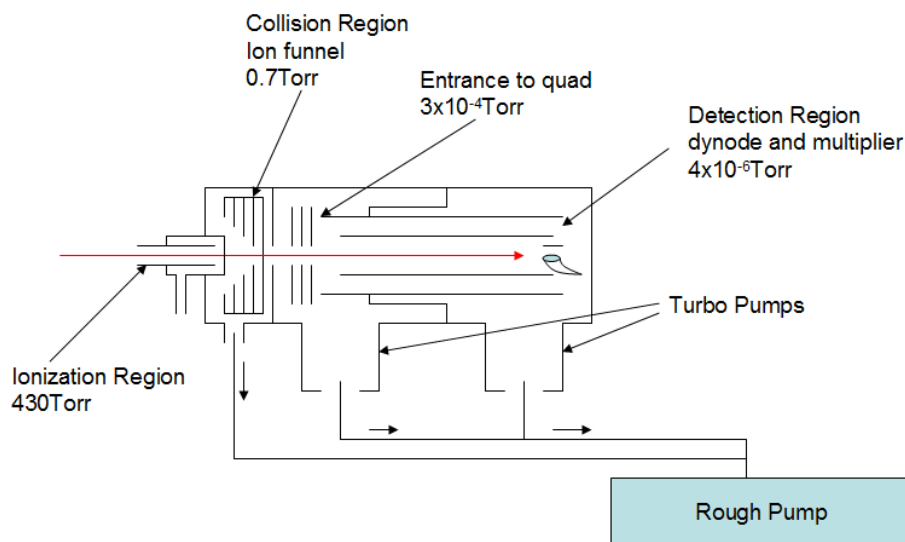
Figure 2.2 Simple schematic of the Meso-CIMS instrument. The red arrow represents an ion beam and the black arrows represent air flow through the instrument.

Ion chemistry

Ionization was initiated at ~ 430 Torr in the ionization region with a ^{63}Ni foil. Sulfur

dioxide was detected in negative ion mode as SO$_5^-$ (Equations 2.1-2.4). The reaction

scheme is given below (Thornton *et al.*, 2002).

$$O_2^- + O_3 \rightarrow O_3^- + O_2 \tag{2.1}$$

$$O_3^- + CO_2 \rightarrow CO_3^- + O_2 \tag{2.2}$$

$$CO_3^- + SO_2 \rightarrow SO_3^- + CO_2 \tag{2.3}$$

$$SO_3^- + O_2 + N_2 \rightarrow SO_5^- + N_2 \tag{2.4}$$

Ozone was added to the air stream just prior to the ionization region by flowing 200 cc/min

of dry air past a UV lamp (Pen Ray). The addition of ozone minimizes the competing

reaction O$_2^-$ + SO$_2 \rightarrow$ SO$_4^-$, and increases the sensitivity of the method (Mohler *et al.,* 1992).

There was potential interference at m/z 112 from the water vapor cluster CO$_4$(H$_2$O)$_2^-$ but it

was eliminated by dropping the pressure in the ionization region from 760 to 430 Torr.

CIMS calibration

Ambient sulfur dioxide mixing ratios were calculated using an internal isotopic standard.

In this method, a flow of gas containing a known concentration of ^{34}SO$_2$ was added to the

flow of ambient air in the main inlet. The ^{34}SO$_2$ was introduced at the beginning of the inlet

to account for any losses of ambient SO$_2$ in the Nafion driers or to the walls if the Teflon

tubing (Figure 2.4). Sulfur dioxide mixing ratios were calculated by referencing the signal

from ambient SO$_2$ at m/z 112 (^{32}SO$_5^-$) to that from the isotopic SO$_2$ at m/z 114 (^{34}SO$_5^-$). The

isotopic standard was delivered from an aluminum compressed cylinder (Scott Marin model 30A) containing a known concentration $^{34}SO_2$, through a calibrated mass flow controller. The ambient SO_2 mixing ratio was calculated according to Equation 2.5.

$$X_{SO2} = \frac{S_{112}}{S_{114}} * \frac{F_{std}}{F_{total}} X_{tank} \qquad\qquad (2.5)$$

Where S_{112} and S_{114} are the signal from ambient and isotopic SO_2 respectively and F_{std} and F_{total} are the flow rates of the isotopic standard and the inlet flow respectively and C_{tank} is the concentration of $^{34}SO_2$ in the compressed cylinder.

Three cylinders was prepared in our lab by bleeding $\sim$ 5 mbar of $^{34}SO_2$ into an evacuated cylinder and then pressurizing with pure N_2. The $^{34}SO_2$ was supplied from a compressed lecture cylinder containing $\sim$97% pure $^{34}SO_2$. These cylinders were calibrated in the lab by referencing the signals at m/z 114 from the compressed cylinder to the signal at m/z 112 from a gravimetrically calibrated permeation device (Vici Metronics model #7446-09-5, Figure 2.3). The permeation device contains pure $^{32}SO_2$ that is released via permeation through a Teflon membrane. The device was kept at 30° C in a temperature controlled chamber with a stream of dry air continuously flowing past the device. The permeation rate is calculated by weighing the tube on $\sim$bi-weekly basis. This technique verified the permeation rate is constant and $\sim$ 50 ng min^{-1}. The flow setup for a calibration consisted of a main flow in a Teflon inlet with a tee for addition of SO_2 from the permeation device and the compressed cylinder. A sub-sample of 1000 cc/min from the main inlet was sampled through the CIMS instrument. A typical tank calibration was carried out in SIM mode monitoring m/z 112 and 114 as follows;

1. Background levels of $^{34}SO_2$ and $^{32}SO_2$ were determined by sampling the house air.

2. The ratio of $^{34}SO_2/^{32}SO_2$ in the cylinder was determined by adding gas from the compressed cylinder to the main flow.

3. The ratio of $^{34}SO_2/^{32}SO_2$ in the permeation device was determined by adding the air stream flowing over the permeation device into the main inlet flow.

4. Flow from the tank and permeation device were added to the inlet flow together. The tank flow was changed in step increments and the mixing ratio of the tank (X_{tank}) was calculated for each tank flow rate according to Equation 2.6.

$$X_{Tank} = \frac{\overline{S_{114}}}{\overline{S_{112}}} * \frac{PfR}{F} \tag{2.6}$$

Where S_{114} and S_{112} are the time averaged signals at m/z 114 and 112 respectively after correction for background interference and cross contamination from $^{32}SO_2$ in the tank and $^{34}SO_2$ in the permeation tube. F is the flow rate of the tank through the mass flow controller, f is the fraction of the permeation tube sampled after the dumps and dilutions, and R is the fraction of $^{32}SO_2/^{34}SO_2$ in the permeation tube.
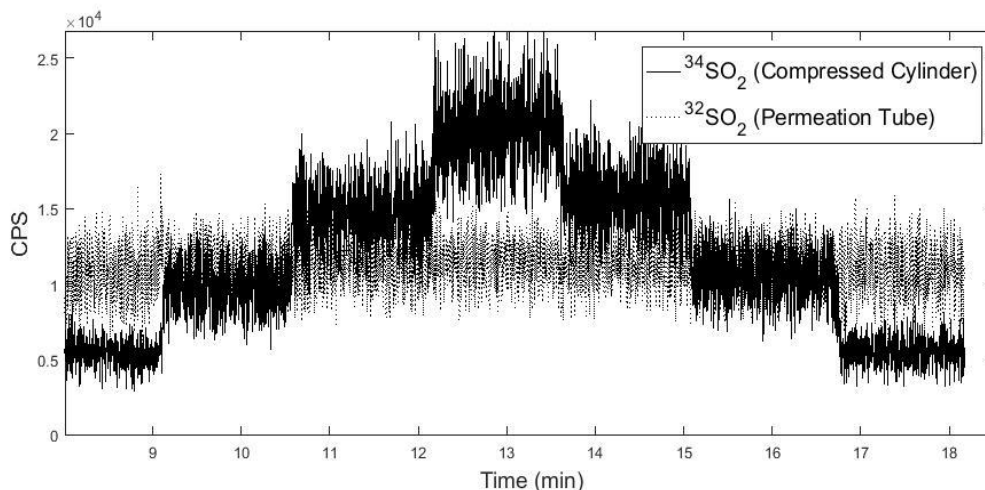
Figure 2.3 Example of a tank calibration. The dotted line is the signal at m/z 112 from $^{32}SO_5^-$ coming from the permeation device. The solid line is the signal at m/z 114 from $^{34}SO_5^-$ coming from the tank. The tank flow was changed in a step wise fashion and the concentration was calculated for each tank flow rate.

It was necessary to sample only a fraction of the permeation tube when conducting a calibration in order to obtain levels of $^{32}SO_2$ in the main flow comparable to the levels of $^{34}SO_2$ from the tank. The fraction of the permeation tube sampled, f, was controlled using a multistage dilution system. This system consisted of four mass flow controllers (Tyaln), the first of which provided the initial flow through the Teflon chamber containing the permeation device. The second third and fourth MFC's in the system provide a dump, dilution and final dump respectively. By calibrating the MFC's relative to each-other a fraction of $^{32}SO_2$ from the initial flow could be sampled. The calibration and associated calculations of the multistage dilution system is described in detail in Gallagher *et al.* (1997).

Flow set-up

This section discusses the tubing and flow set-up used to make trace gas measurements with the CIMS instrument. A ¼ in Teflon tube carried gas from near the sensing region of the sonic anemometer to the CIMS instrument in the shed. The gas inlet was mounted $\sim$ 2-4 cm behind the transducers of the sonic anemometer to avoid flow distortion but to minimize separation from the sonic anemometer sensing region (Figure 2.1). The airflow was dried with two counter-flow Nafion driers connected in series at the front of the inlet (Perma Pure Inc. Model PD-625-24PP). A sub-sample of $\sim$1000 cc/min was drawn off the main inlet flow, through the ionization region of the CIMS. Ozone was added to the air stream just prior to the ionization region by flowing dry air past a UV lamp (Pen Ray). A 1/8 Teflon tube carried $^{34}SO_2$ isotopic standard from a compressed cylinder located in the shed to the entrance of the inlet on the end of the boom (Figure 2.4). Ambient air was pumped down the main inlet and through the CIMS with a carbon vane pump (Gast model 1023) and flow rates were maintained using thermal conductivity mass flow controllers interfaced to the PC through a custom 16-bit digital mass flow controller module. Pure air for the Nafion counter-flow driers and ozone generator were supplied with a pure air generator and compressor (Aadco model 737-11), located in the shed. A simple schematic of the flow set-up is shown in Figure 2.4. The various flow rates used in the Scripps and Duck field campaigns are shown in Table 2.2.
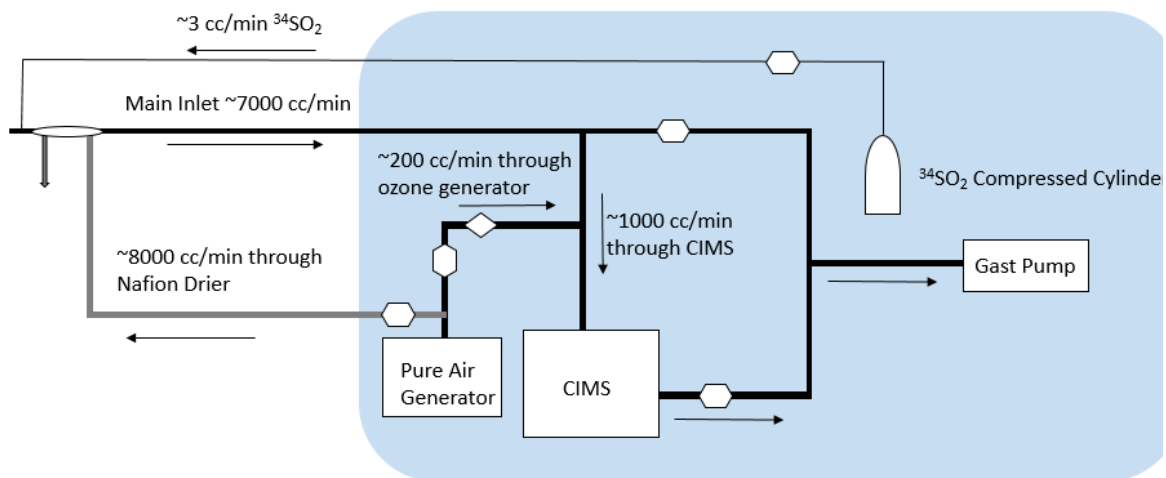
Figure 2.4 Schematic of the flow setup used during the field campaigns in San Diego and Duck.

Table 2.2 Flow rates used during the Duck and Scripps field campaign.

Flow	Flow (cc min^{-1} STP)	
	Scripps	Duck
Inlet	8500	6500-7300
Source	1000	950
Ozone	200	200
Tank	1-10	1-10
Driers	7000	7000
Total Flow	9750	7700-8500

Inlet characterization

The total flow down the inlet is calculated according to Equation 2.7;

$$F_{total} = F_{inlet} + F_{source} + F_{CIMS} - F_{ozone}$$
(2.7)

Where F_{inlet} is the flow rate of the main inlet, F_{source} is the flow through the source region of instrument, F_{CIMS} is the flow rate through the vacuum region of the instrument and F_{ozone} is the flow rate past the ozone generator.

The flow through the CIMS is a function of the pressure in the source region and the diameter of the pinhole. The flow through the CIMS was measured in the lab to be ~ 450 cc/min. Inlet flow rates varied over the course of the Duck experiment due to occasional clogging in the inlet.

The inlets used at the Scripps and Duck Pier was 13 m and 21 m respectively, with an I.D. of $\sim$2-4 mm. Transit times down the inlets were calculated according to Equation 2.8,

$$T = L * \left(\frac{F_{total}}{A}\right)^{-1}$$
(2.8)

where L is the length of the inlet and A is the cross-sectional area of the inlet tubing. These transit times were verified for each flux interval by examining the covariance between vertical wind speed and SO_2 concentration. Fluxes of SO_2 were calculated using a range of delay times. The delay producing the largest flux was taken to be the correct delay. The calculated and verified transit time roughly agreed with each other (Table 2.3).

Table 2.3 Length and transit times for inlets used at Scripps and Duck Piers.

Inlet	Length (m)	Transit Time Calculated (seconds)	Transit Time Verified (seconds)
Scripps	13	1	0.9-1.3
Duck	21	1-2	1.3-1.8

High frequency fluctuations in SO_2 are damped during passage through the air inlet tubing. The attenuation characteristics of the inlets used at Duck and Scripps were examined in the laboratory. A scenario was created where a flow of air containing SO_2 from a permeation device was sampled through the inlet. The flow of SO_2 was instantaneously interrupted by quickly removing the tubing from the inlet. This caused a delayed exponential decrease in SO_2 signal at the mass spectrometer. A decay constant (k) was calculated by fitting a linear regression to the logarithm of the signal in the decay region of the time series (Equation 2.9, Figure 2.5),

$$\log(sig) = -(k)t + C \tag{2.9}$$

where k is decay constant, t is time and C is a constant. The cut-off frequency was calculated according to Equation 2.10.

$$F_c = \frac{k}{2\pi} \tag{2.10}$$

This test was done multiple times, the average cut-off frequency for the Scripps and Duck inlets were 1.4 ± 0.1 Hz and 1.6 ± 0.1 Hz respectively.
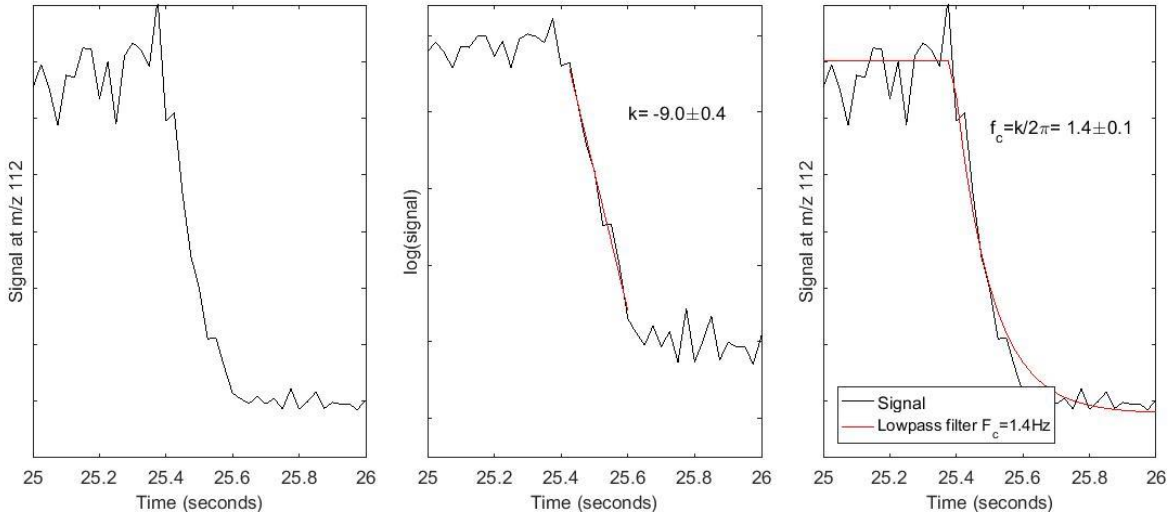
Figure 2.5 Scripps inlet high frequency attenuation characteristics. Signal at m/z 112 vs. time. Left – Response of signal to removal of SO_2. Middle – Log plot of signal (Black line) and linear regression to signal decay (red line). Right – same as left with filtered step change on top of signal (red).
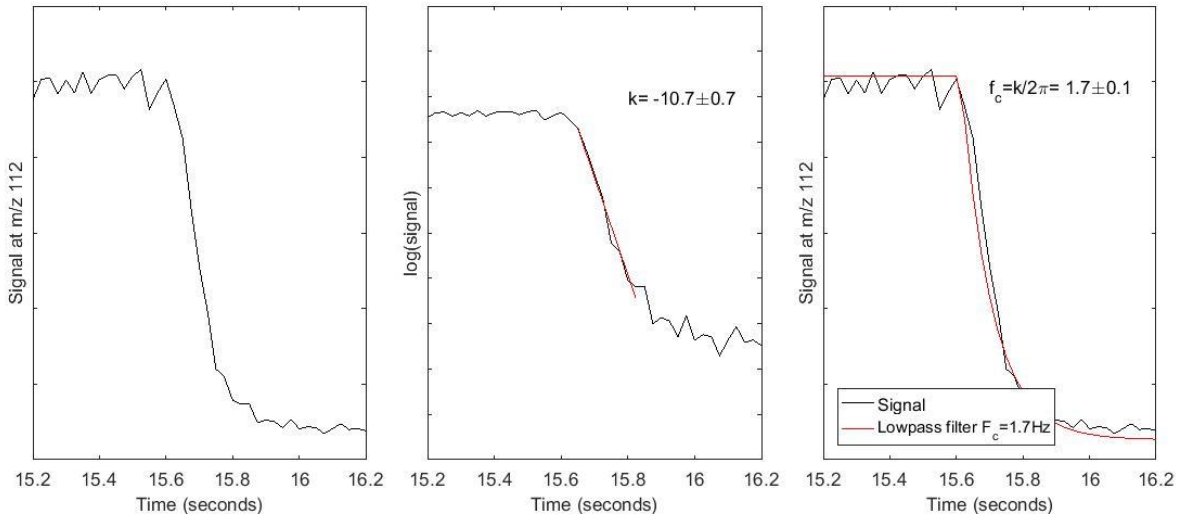
Figure 2.6 Duck inlet high frequency attenuation characteristics. Signal at m/z 112 vs. time. Left – Response of signal to removal of SO_2. Middle – Log plot of signal (Black line) and linear regression to signal decay (red line). Right – same as left with filtered step change on top of signal (red).

A first-order Butterworth filter was designed in Matlab using the calculated cut-off frequencies. A high frequency correction factor or gain, G, was computed for each flux interval by applying the filter to the time series data and taking the ratio of the filtered and unfiltered fluxes as follows:

$$G = \frac{F_{unfiltered}}{F_{filtered}} \tag{2.11}$$

This approach was applied to the sonic anemometer temperature time series. The gains were regressed against wind speed (Figure 2.7). The regressions of G vs U_{10} were not statistically different between the Scripps and Duck inlets (Figure 2.7, Table 2.4). The Scripps inlet is shorter than the duck inlet by 8 m which theoretically means the loss of high frequency fluctuations is likely occurring in the instrument and not limited by the length of the inlet. This relationship was used to correct the individual flux measurements for high frequency loss.
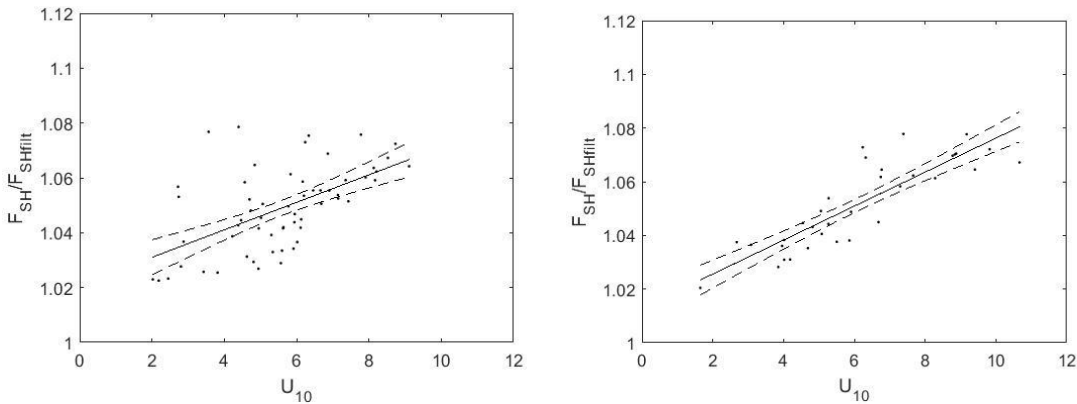
Figure 2.7 High frequency gain calculated from sensible heat data collected at Scripps (Left) and Duck (Right) Pier regressed against wind speed.

Table 2.4. Slope and intercept of the regressions to F_{SH}/F_{SHfilt} vs. U_{10} from the inlets at Scripps and Duck Pier.

	Scripps Inlet Gain	Duck Inlet Gain
Slope	5.01 ± 0.92 (x 10^{-3})	5.58 ± 0.66 (x10^{-3})
Intercept	1.01 ± 0.0	1.01 ± 0.0

2.3. Data acquisition and processing

Data acquisition

This section discusses the data collection from the various meteorological sensors and CIMS instrument as well as the processing techniques used. The analog data coming from the meteorological sensors was filtered with a Butterworth filter and logged at 50 Hz using a National Instruments SCXI 1001 data logger. Signals from the CIMS were amplified with an amplifier/discriminator and digitized with a National Instruments USB 6343 unit. The digital CIMS data were logged locally on the PC interfaced to the CIMS. The digital data from the CIMS were converted to analog in real time and logged at 50 Hz with the meteorological data. Data streams from the meteorological sensors and CIMS were adjusted to account for processing delays and transit times down the inlet. Delays from the meteorological sensors were relatively small (~200 ms) and provided in the instrument manuals.

Data processing

The analog data from the various meteorological sensors were converted to geophysical units following the equations detailed in the user manuals. Temperature measurements from the sonic anemometer were corrected to account for water vapor according to Equation 2.12,

$$T = \frac{T_{raw}}{1 + 0.32\frac{P_v}{P}}$$ (2.12)

where T_{raw} is the raw sonic temperature, P_v is the partial pressure of water vapor in pascals and P is total air pressure. The dry air density, ρ_{dry}, was calculated according to the ideal gas law (Equation 2.13) and is defined as moles of dry air per cubic meter.

$$\rho_{dry} = \frac{P_{dry}}{T * R}$$ (2.13)

Where P_{dry} is the dry air pressure defined as the difference between the total air pressure (P) and the partial pressure of water vapor (P_v) and R is the ideal gas constant. Water vapor concentrations were converted to a dry air mixing ratio, defined as mole of water vapor per mole of dry air, according to Equation 2.14,

$$X_{H2O} = \frac{C_{H2O}}{\rho_{dry}}$$ (2.14)

where C_{H2O} is the water vapor concentration. Sulfur dioxide concentrations were calculated using Equation 2.15,

$$C_{SO2} = X_{SO2} * \overline{n_d}$$ (2.15)

where X_{SO2} is the sulfur dioxide mixing ratio calculated according to equation 2.5 and n_d is the number density of air in moles per cubic meter, calculated using the ideal gas law.

The time series data were divided into $\sim$ 15 min flux intervals (Figure 2.8). Average bulk meteorological conditions and fluxes of momentum, water vapor and SO_2 were calculated for each flux interval. Fluxes were calculated according to equations 2.16 to 2.19,

$$F_{SO2} = \overline{w'C'}_{SO2} \tag{2.16}$$

$$F_{H2O} = \overline{w'X'}_{H2O}\bar{\rho}_{dry} \tag{2.17}$$

$$F_{mom} = \overline{w'u'}\bar{\rho} \tag{2.18}$$

$$F_{SH} = \overline{w'T'}\,\bar{\rho}c_p \tag{2.19}$$

Where c_p is the heat capacity of air, ρ is air density in kg m^{-3}, the ' denotes fluctuations from the average signal over the flux interval and the other variables are defined previously. Transfer velocities were calculated for each flux interval by dividing fluxes by average thermodynamic gradients driving the flux; In the case of momentum 10 m wind speed is the driving force (Equations 2.20 to 2.23).

$$k_{SO2} = \frac{F_{SO2}}{\bar{C}_{SO2}} \tag{2.20}$$

$$k_{H2O} = \frac{F_{H2O}}{(\bar{X}_{H2O} - \bar{X}_s)\bar{\rho}_{dry}} \tag{2.21}$$

$$k_{mom} = \frac{F_{mom}}{\overline{U_{10}\bar{\rho}}} \tag{2.22}$$

$$k_{SH} = \frac{F_{SH}}{(\overline{T} - \overline{T}_s)\bar{\rho}\,C_p}$$

<div align="right">(2.23)</div>

Where X_s is the theoretical mixing ratio of water vapor at the saturation vapor pressure at

the sea surface temperature. Saturation vapor pressures were calculated following

Sharqawy *et al.* (2010).
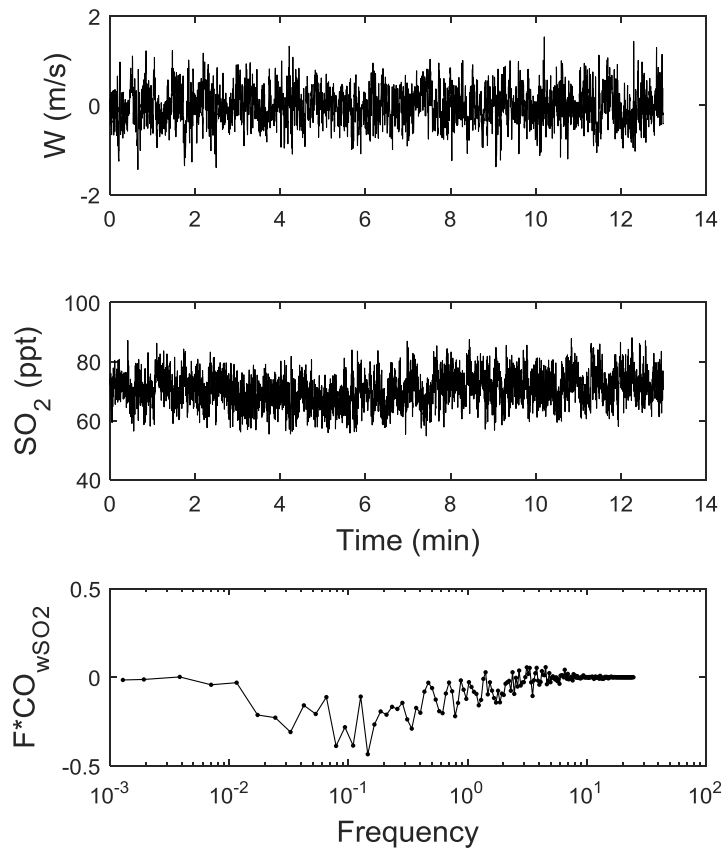
Figure 2.8 Example of a flux interval taken during the field
campaign in Duck, NC. The top panel is a time series of vertical
wind speed and the middle panel is a time series of SO_2 mixing ratio.
The bottom panel is the frequency weighted co-spectra.   The area
above the co-spectra represents the average flux during the flux
interval.

Quality control was applied to the data to reject bad or contaminated flux intervals. The criteria to reject a flux interval were slightly different for each field deployment and are detailed below.

1. Normalized cumulative flux – A plot of flux (normalized by the total flux) vs. frequency was generated for each parameter (SO$_2$, water vapor, sensible heat, momentum) for each flux interval. Intervals exceeding or opposite in sign to the total flux at 0.004 Hz and 0.008 Hz for the Scripps and Duck deployments respectively, were identified and eliminated. Intervals were declared excessively noisy if the difference between cumulative flux at two consecutive frequencies exceeded 18% and 12% for the Scripps and Duck deployments respectively. Flux intervals with obvious deviations in co-spectral shape from those defined in Kaimal *et al.* (1972) were eliminated subjectively.

2. Thermodynamic gradients – Intervals with relatively small thermodynamic gradients across the air sea interface were identified and eliminated. The minimum thermodynamic gradient for each parameter are shown in Table 2.5.

Table 2.5 Air/sea thermodynamic differential thresholds for accepting flux intervals. Thresholds apply to both field campaigns.

Parameter	Threshold
Water Vapor	1×10^{-3} (mol/mol)
SO$_2$	10 (pmol mol^{-1})
Sensible Heat	0.7 (°C)

3. Wind sector – Wind direction was variable during the Duck campaign. Flux intervals with average winds outside a defined wind sector were eliminated. This

eliminated intervals where winds may be coming over land or from a direction with

interference from structures.

4. Atmospheric stability – Flux intervals with an atmospheric stability parameter,

z/L, > 0.07 were rejected to avoid stable conditions.

5. Electronic noise and contamination – Intervals with obvious electronic spikes or

sharp excursions in SO_2 likely reflecting local contamination were rejected.

Validation

Background interference at m/z 114 and 112 in the field were determined by attaching a

filter (Whatman No. 41) on the front of the inlet that had been soaked in 1% K_2CO_3 solution.

This technique ensured background interference at m/z 112 and 114 were minimal (Figure

2.9).
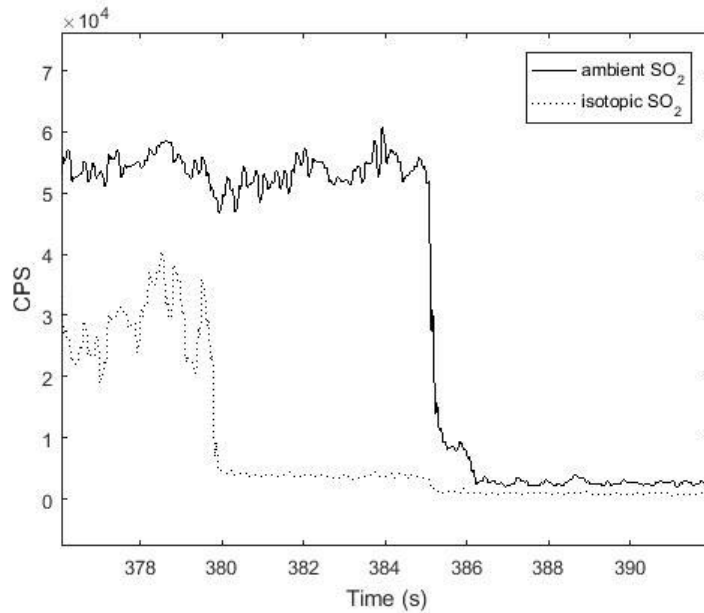
Figure 2.9 Instrument background at m/z 112 (ambient SO_2) and m/z 114 ($^{34}SO_2$) taken during the deployment in Duck, NC. A carbonate filter was used to scrub the isotope and ambient signal at 386 seconds. Note the initial drop in isotope at 380 seconds was caused by removing the tubing carrying the isotope when attaching the carbonate scrubber.

The time series from the ambient SO_2 and isotopic $^{34}SO_2$ showed clearly different behavior in the field (Figure 2.10). The signal at m/z 112 had much larger variability compared to the internal standard. The fluctuations in the ambient signal likely reflects the downward transport of $^{32}SO_2$ to the sea surface via turbulent eddies in the marine surface layer.
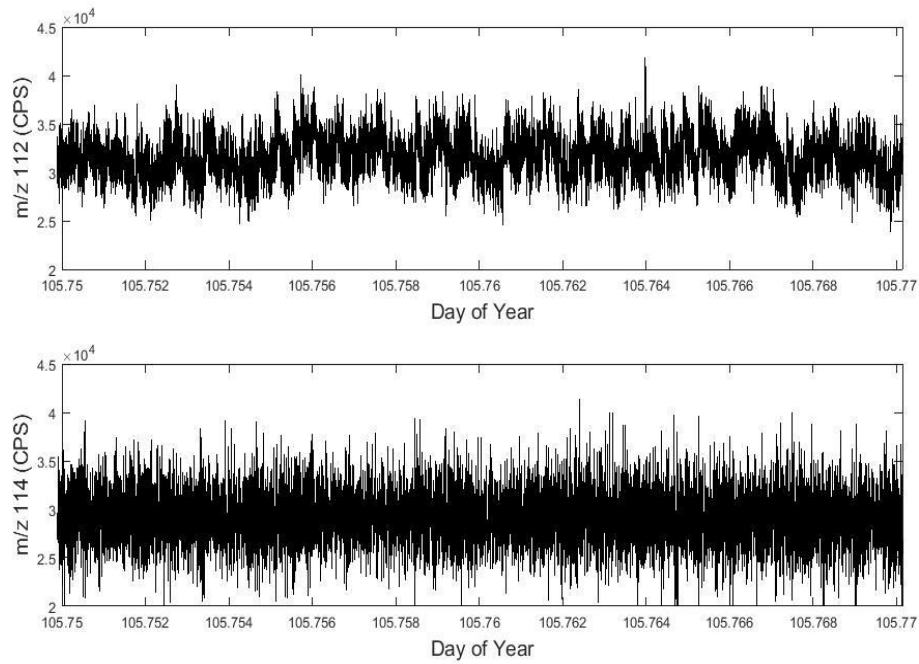
Figure 2.10 Example of raw data from the Duck Pier. Top panel is m/z 112 ($^{32}SO_5$) from ambient SO_2 and the bottom panel is m/z 114 ($^{34}SO_5^-$) from the compressed cylinder. The ambient signal has clear fluctuations that are associated with turbulent eddies in the atmosphere while the isotope signal is relatively constant.

3. Flux measurements at the Scripps pier

3.1. Overview

The Scripps deployment is the first attempt at making simultaneous ground-based flux measurements of SO_2 and sensible and latent heat in the marine boundary layer. The goals of this deployment were to (1) assess the performance of the CIMS with the ion funnel in measuring SO_2 in the marine boundary layer, (2) determine if the CIMS instrument and the experimental set-up are capable of measuring SO_2 fluxes, (3) compare transfer velocities of the scalar fluxes (SO_2, H_2O, sensible heat) to each other and to momentum transfer velocities, and (4) determine if any observable differences in the transfer velocities can be attributed to physical processes in the boundary layer.

This study was conducted at the Scripps pier located in La Jolla, California. The local meteorology is characterized by a daily westerly sea-breeze with occasional frontal systems that generally approach from the north-west. The Scripps facility is near our laboratory, has easy access and sufficient power to run electrical equipment in a shed located on the end of the pier. The pier structure extends 330 m from the coast WNW at a heading of ~290° to a water depth of 10 m. The end of the pier extends roughly 100 m past breaking waves and a ~ 6 m long aluminum boom is located on the north-west corner of the pier that can rotate out over the water surface to avoid flow distortion from the pier.

3.2. Results

Meteorological and oceanographic conditions

The field study was carried out from April 6th to April 27th and resulted in approximately 100 hours of data. The data were divided into 13 min flux intervals and average bulk meteorological and oceanographic properties were calculated for each interval. Winds were generally light during the study, with a mean wind speed of 3.8 ± 2.0 m/s and a range of 0-9.7 m s^{-1}. The average relative humidity was 80% and coastal fog in the mornings was common. Air temperatures were 16.2±1.3 °C with a range from 12.9-19.9 °C and sea water temperatures averaged 16.5±0.9 °C with a range of 13.8-18.3 °C. The SO_2 mixing ratio was highly variable over the course of the study with an average of 100 pmol mol^{-1} and ranging from 0 to 560 pmol mol^{-1}. Sharp spikes in SO_2 were usually associated with military/commercial vessels passing upwind of the pier and low SO_2 levels were associated with the occurrence of fog.

Air masses approached the study site from the northerly direction. A high-pressure region was located over the study site for the first few days of the deployment (DOY's 97-100) during which winds were light and air temperatures were warm. Air mass back trajectories from this period indicated air masses were pushed inland over California before reaching the site (Figure 3.1). Thus, SO_2 levels were relatively high during this time likely due to pollution from fuel combustion. After the high pressure moved out of the region air masses generally approached the study site by traveling over the ocean and SO_2 levels were relatively low. There was a notable increase in wind speed starting at DOY 106.

On DOY 115 a low pressure passed over the region and brought extremely high winds

(Figure 3.1).

Figure 3.1 Left column – 500 mbar height contours for North America on DOYs' 98, 106 and 116 at 1100 UTC (National Weather Service). Right column – 120-hour backward trajectories from Scripps Pier ending at 2000 UTC for DOYs' 98, 106 and 116.
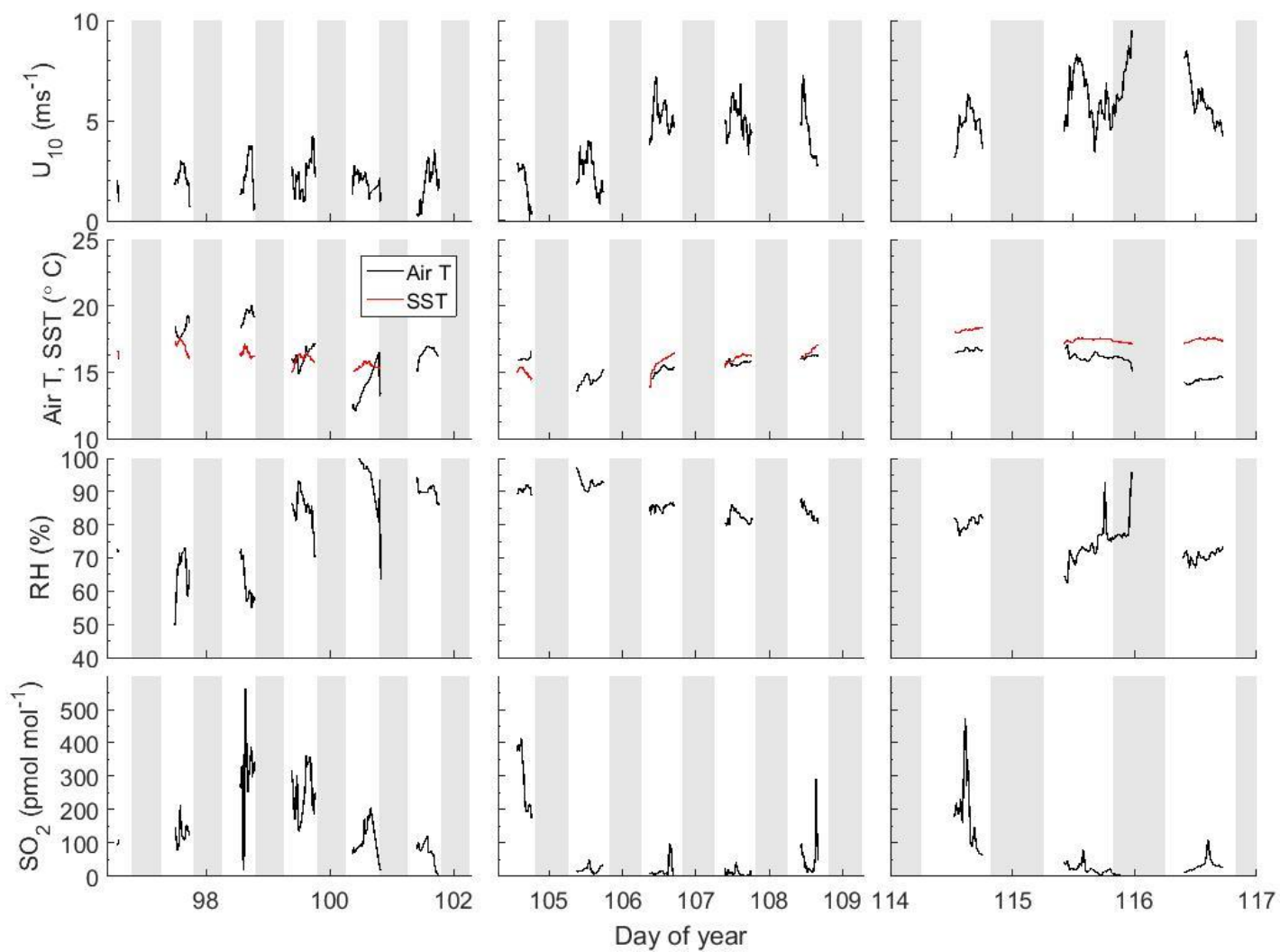
Figure 3.2 Time series of meteorological and oceanographic parameters during the Scripps deployment. The grey bands indicate night time hours.

47

CIMS instrument performance

The CIMS instrument successfully measured SO_2 in the marine boundary layer for the duration of the deployment. The average signal at m/z 112 and 114 was ~ 12,000 and ~29,000 cps respectively over the duration of the deployment (Figure 3.3). This resulted in a mean calculated SO_2 mixing ration of ~ 100 pmol mol^{-1}. Attaching the carbonate scrubber on the entrance to the inlet dropped the signal to ~ 1000 cps and further increased confidence that SO_2 was being measured. Spikes in the signal at m/z 112 were associated with passing commercial vessels which were likely emitting diesel exhaust known to be rich in sulfur.

The average sensitivity was calculated for each flux interval according to Equation 3.1,

$$S = \frac{\overline{cps}_{114}}{X_{tank}} * \frac{F_{total}}{F_{tank}} \qquad (3.1)$$

Where cps_{114} is the average counts at m/z 114 during the flux interval, X_{tank} is the tank mixing ratio, F_{total} is the total inlet flow and F_{tank} is the tank flow. The CIMS had an average sensitivity in the field of ~120 cps/(pmol mol^{-1}). The sensitivity of the instrument varied over the course of the deployment from 65 cps/(pmol mol^{-1})to 250 cps/(pmol mol^{-1}) (Figure 3.3). It is unclear what caused the variability in the CIMS sensitivity over the course of the experiment. Sensitivity was notably high when SO_2 mixing ratios were below ~50 pmol mol^{-1} but generally constant when mixing ratio was larger than 50 pmol mol^{-1} (Figure 3.4). Sensitivity was also inversely correlated with water vapor mixing ratio. This is probably due to loss of $^{34}SO_2$ in the inlet to the walls of the tubing from condensation.
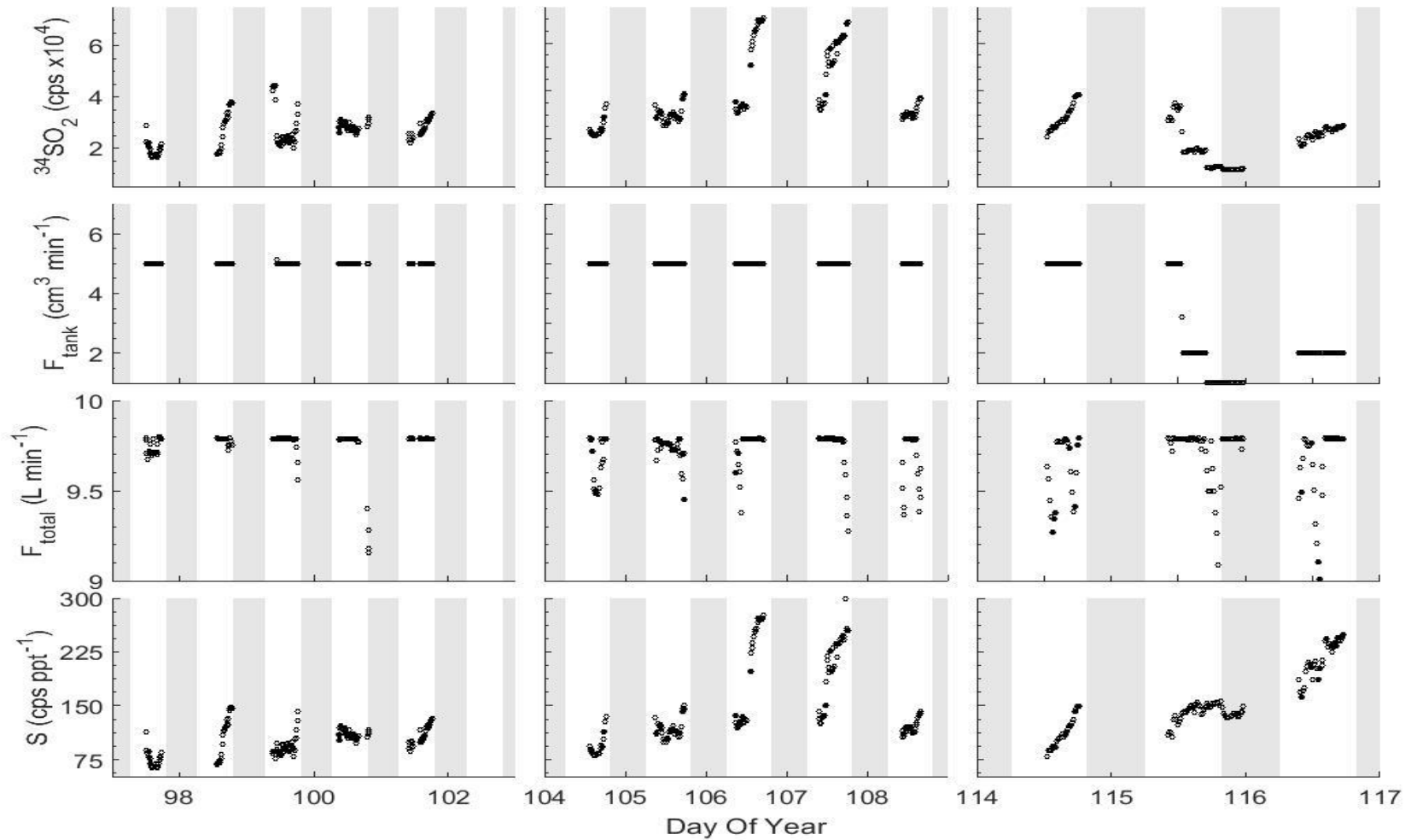
Figure 3.3 Time series of the CIMS instrument performance during the Scripps campaign. The top row shown average counts at m/z 114 from the isotopic standard ($^{34}SO_2$). Rows two and three shows the tank flow and total inlet flow respectively. The fourth row shows the sensitivity of the CIMS instrument (cps pmol^{-1} mol).
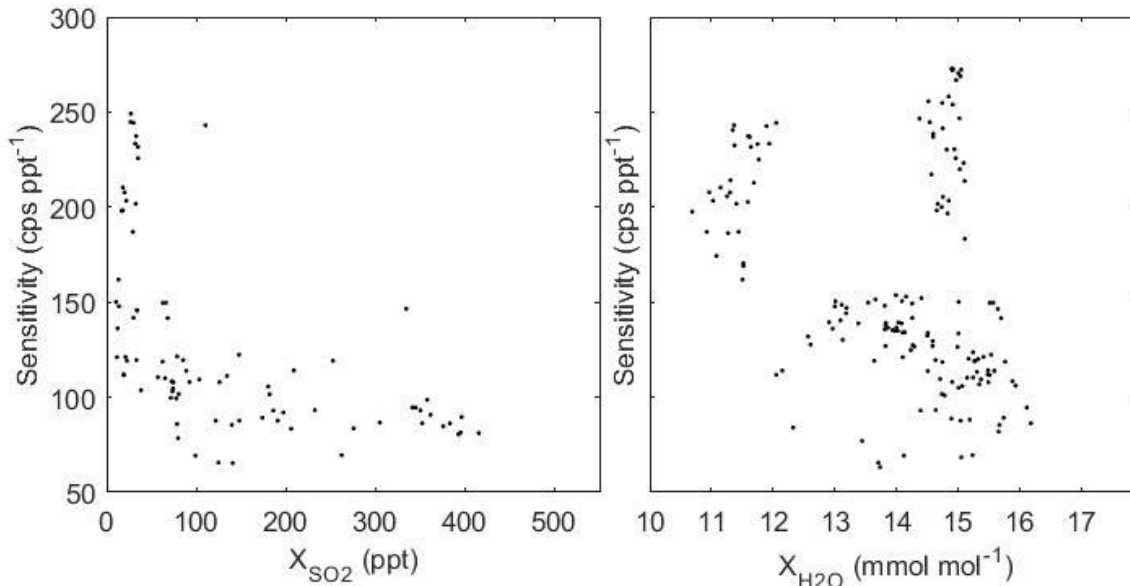
Figure 3.4 CIMS sensitivity vs. SO$_2$ mixing ratio (left) and CIMS sensitivity vs H$_2$O mixing ratio (right) during the Scripps deployment. The data shown passed quality control for the respective parameter.

Air/sea thermodynamic differentials and fluxes

The average air/sea temperature differential was 0.56 ± 1.55 °C with a range from -3.5 °C to 2.7 °C with positive values representing a warmer ocean than atmosphere by convention. Occasionally air/sea temperature differentials had diurnal variability which reflected the daily air temperatures. Starting around DOY 114 sea water temperatures warmed and were significantly warmer than air temperatures for the remaining three days of the study. Sensible heat fluxes generally reflected the air/sea temperature differential in magnitude and direction over the course of the study indicating that fluxes of sensible heat were successfully measured. There were a few instances when sensible heat flux was opposite in direction to the thermodynamic differential which may suggest a slight bias in either air or seawater temperature measurement. These cases were usually associated

with very small temperature differences and none of those intervals passed the quality control criteria. Large sensible heat fluxes were observed on the last two days of the study when passage of a low-pressure system brought high wind speeds and colder air temperatures (Figure 3.5).

The thermodynamic gradient for water vapor was positive (from the ocean to the atmosphere) for duration of the study and the observed fluxes were all upward (Figure 3.6). The warm sea water temperatures combined with the high winds and cold temperatures on the last two days of the study resulted in large H_2O fluxes.

All the observed SO_2 fluxes were from the atmosphere to the ocean surface and ranged from 0 to 65 pmol m^{-2} s^{-1} with the largest fluxes observed at the beginning and end of the deployment associated with high SO_2 levels and high wind speeds respectively (Figure 3.7).
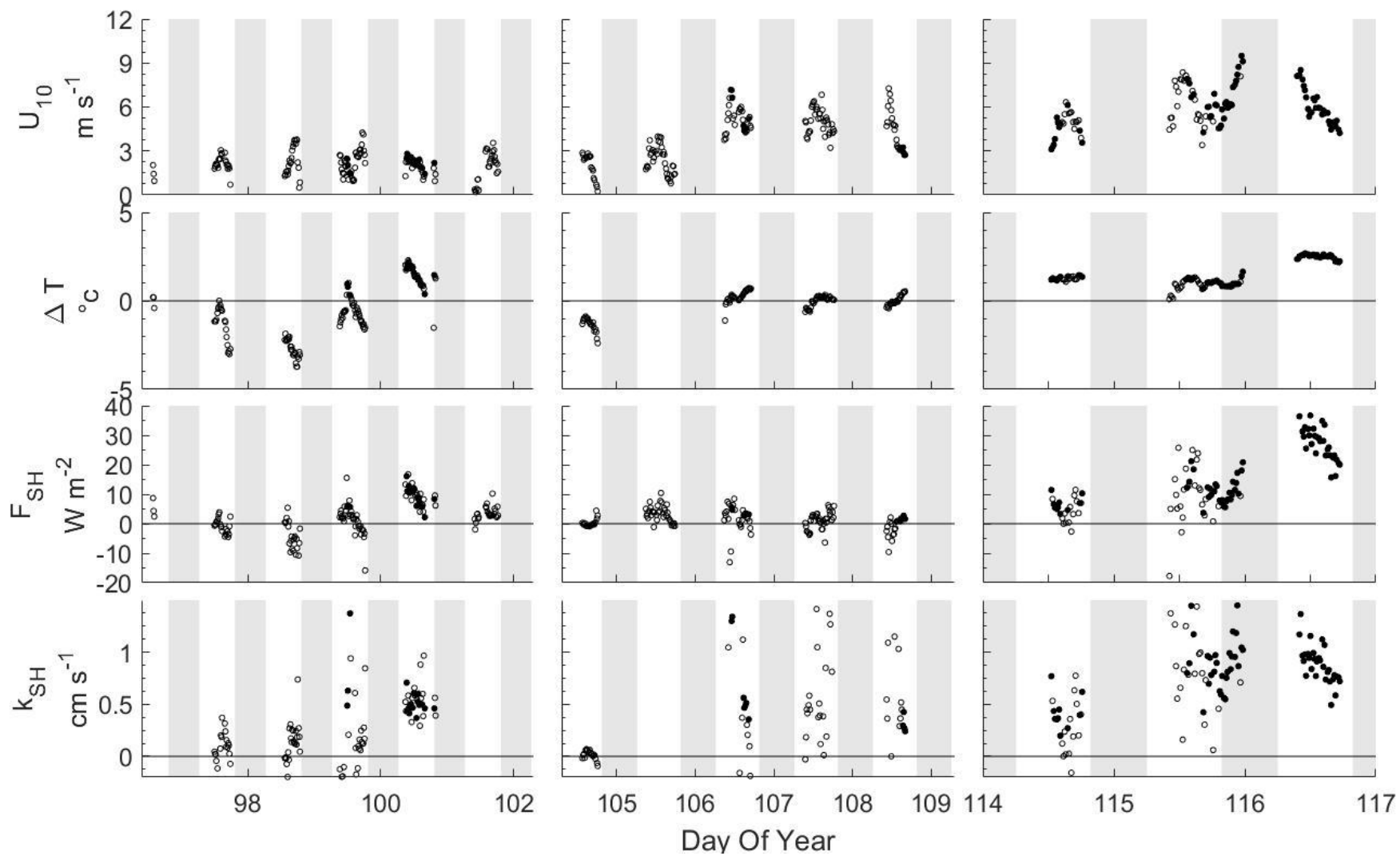
Figure 3.5 Time series of parameters related to sensible heat flux collected at Scripps Pier from April 6th – 27th. Solid data points passed quality control criteria.
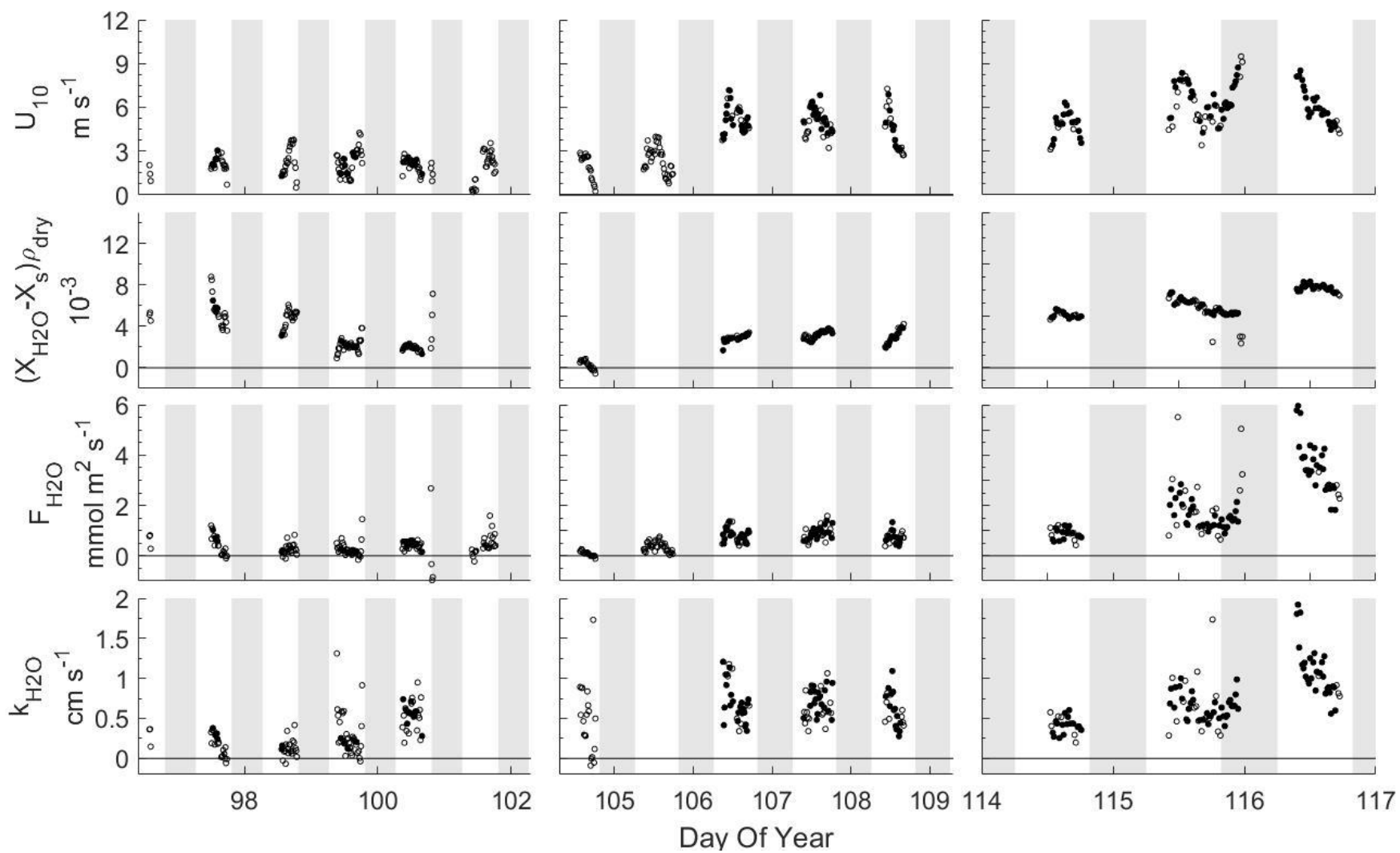
Figure 3.6 Time series of parameters related to water vapor flux collected at Scripps Pier from April 6th – 27th. Solid data points passed quality control criteria. White bands indicate daylight hours.
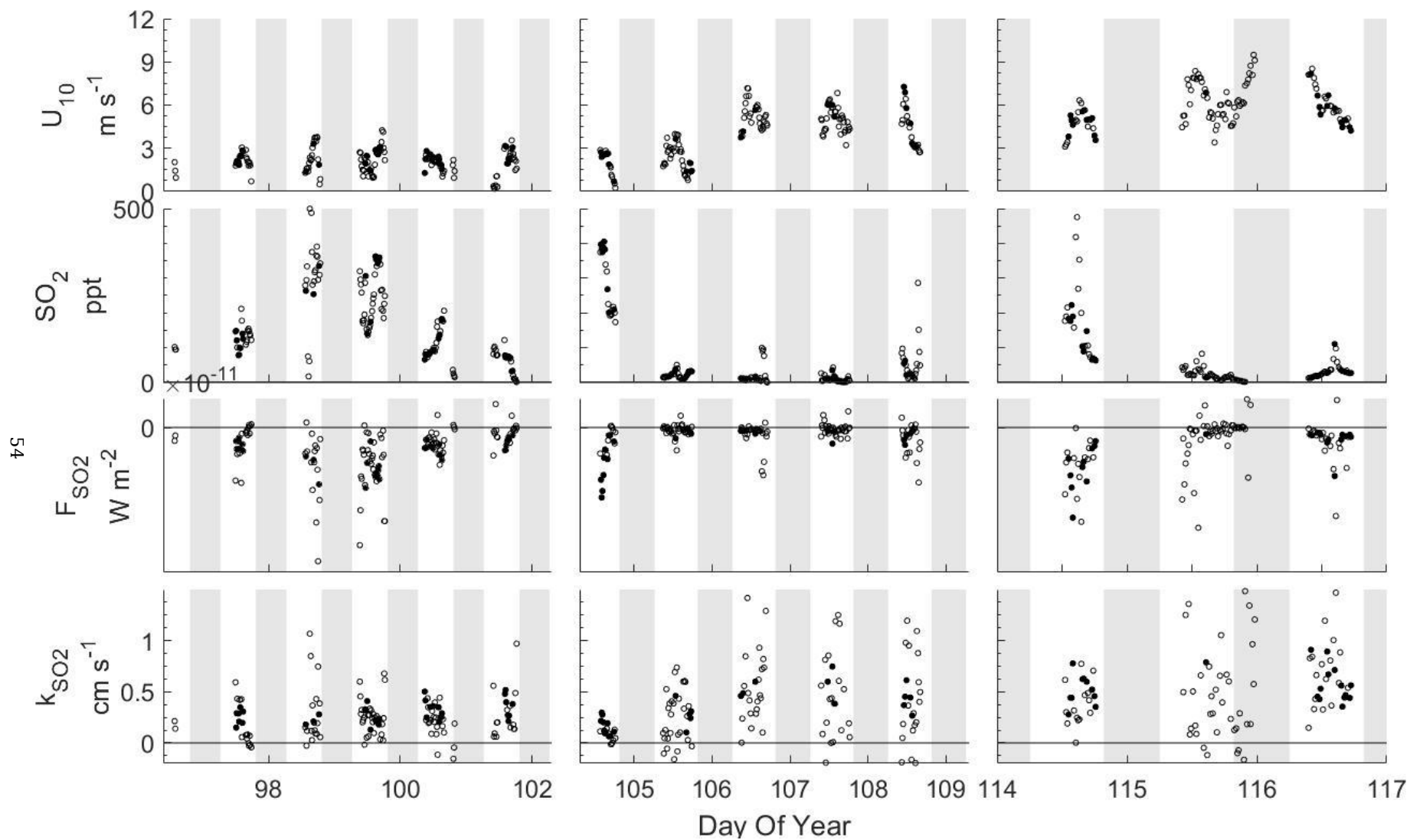
Figure 3.7 Time series of parameters related to SO₂ fluxes at collected at Scripps Pier from April 6th – 27th. Solid data points passed quality control criteria.   White bands indicate daylight hours.

Co-spectra

The co-variance of the fluctuations of vertical wind and atmospheric concentration of the various parameters are shown in the form of co-spectra (Figures 3.8-3.10). Co-spectra are useful for validating flux measurements and assessing the the quality of the dataset. All SO_2 co-spectra were negative indicating fluxes were exclusively from the atmosphere to the ocean (Figure 3.8). This is consistent with the theory that sea water concentrations of SO_2 are negligible. All water vapor and sensible heat co-spectra were positive indicating fluxes were exclusively from the ocean to the atmosphere (Figures 3.9 and 3.10). The directionality of the water vapor and sensible heat fluxes agree with the measured thermodynamic potentials (Figures 3.5-3.7). Theoretical co-spectra defined in Kaimal *et al.*, (1972) were within one standard deviation of the frequency weighted normalized co-spectra measured at Scripps Pier for all parameters. The co-spectra measured during DOY's 114-117 were significantly larger than those measured during the rest of the campaign because of the strong winds and large air/sea thermodynamic differentials observed during that period (Figures 3.5-3.7).
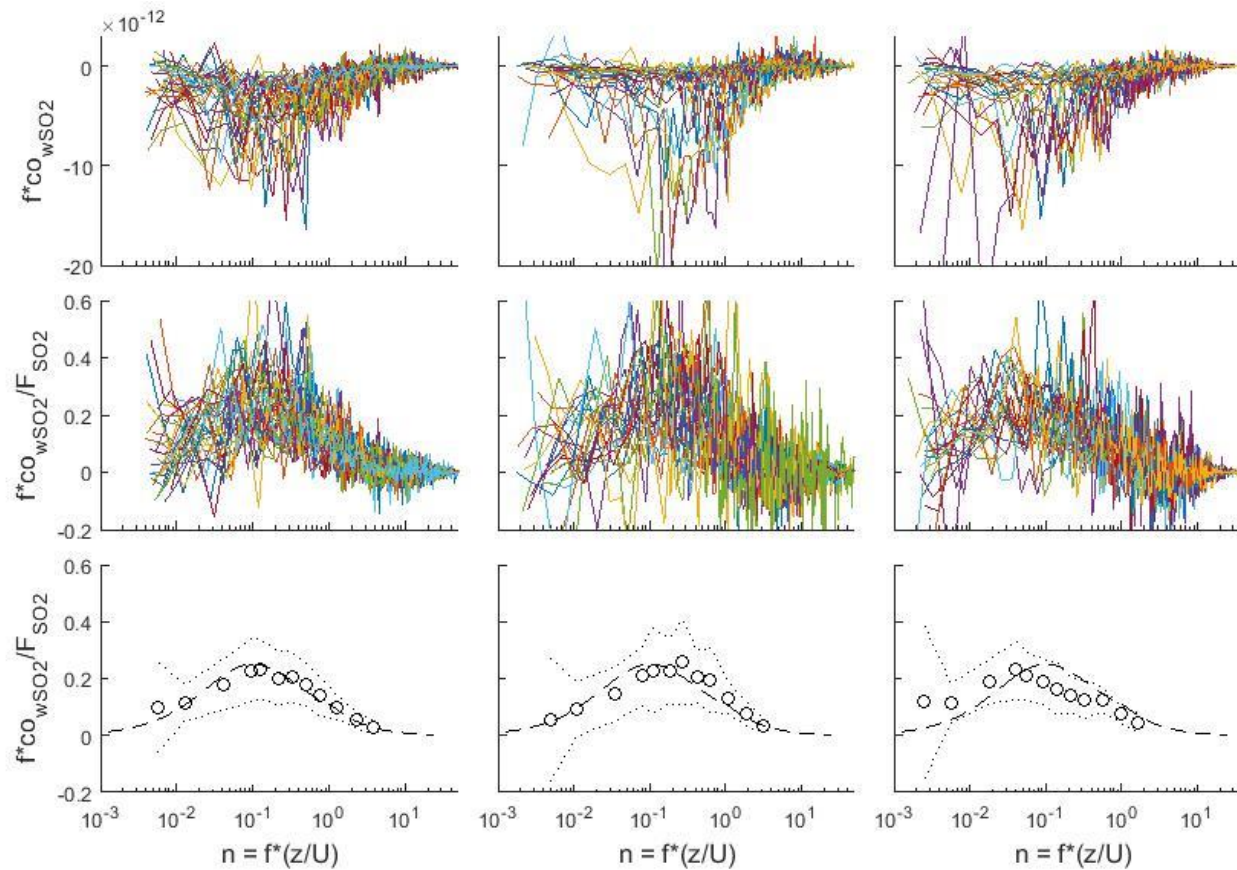
Figure 3.8 Frequency weighted co-spectra of vertical wind and SO_2 concentration for flux intervals collected at Scripps Pier divided into three-time periods. The respective time-periods for columns 1-3 are DOY's 96-102, 104-109 and 114-117. Top: individual co-spectra for 13-minute flux intervals; Middle: Same as top except co-spectra have been normalized to the average flux during the interval. Bottom: Bin-averages of the flux normalized co-spectra (circles), ± 1 standard deviation (dotted line), and theoretical co-spectral shape from Kaimal *et al*. (1972), (Dashed line).
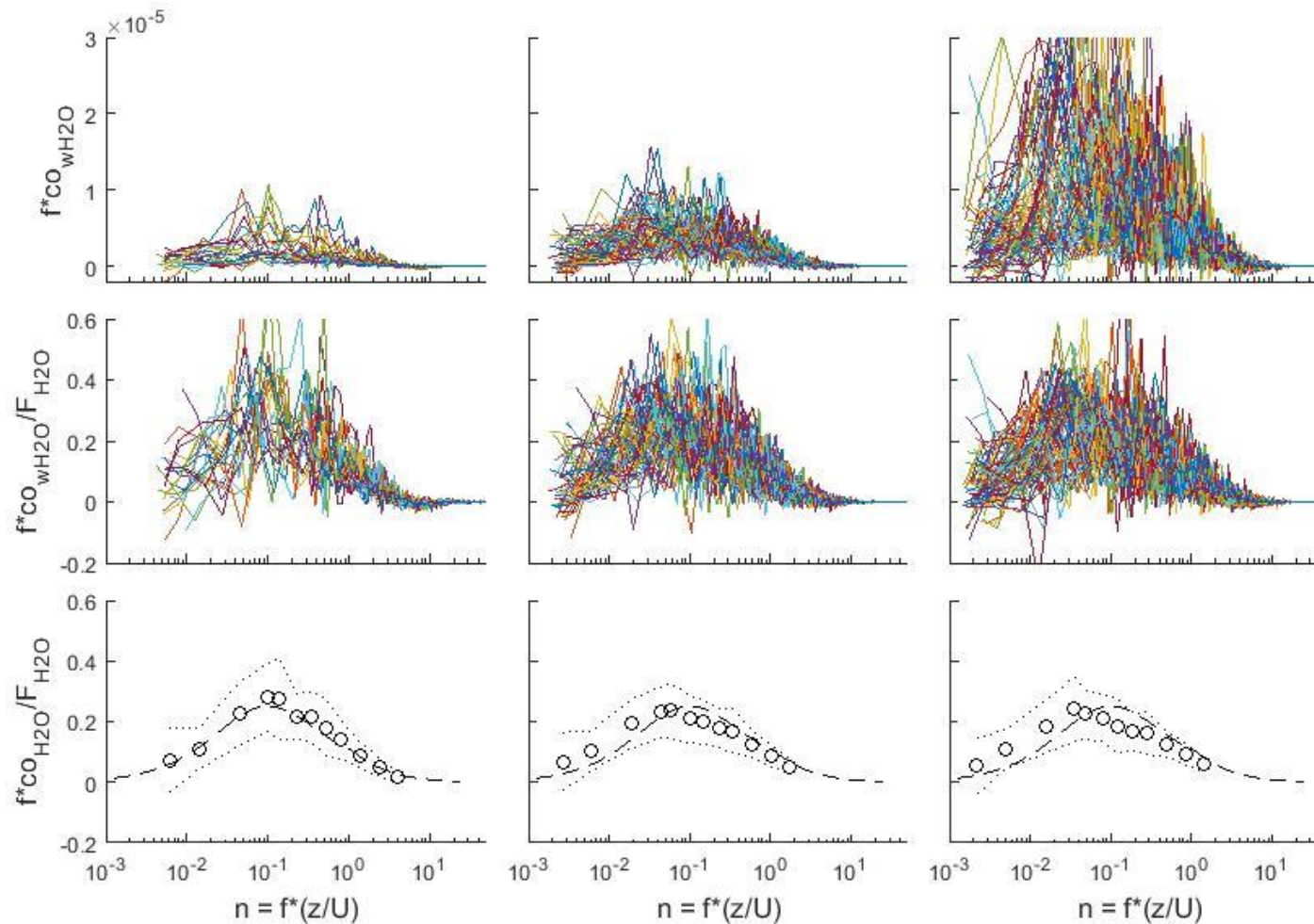
Figure 3.9 Frequency weighted co-spectra of vertical wind and water vapor concentration for flux intervals collected at Scripps Pier divided into three time-periods. The respective time-periods for columns 1-3 are DOY's 96-102, 104-109 and 114-117. Top: individual co-spectra for 13-minute flux intervals; Middle: Same as top except co-spectra have been normalized to the average flux during the interval. Bottom: Bin-averages of the flux normalized co-spectra (circles), ± 1 standard deviation (dotted line), and theoretical co-spectral shape from Kaimal *et al.* (1972), (Dashed line).
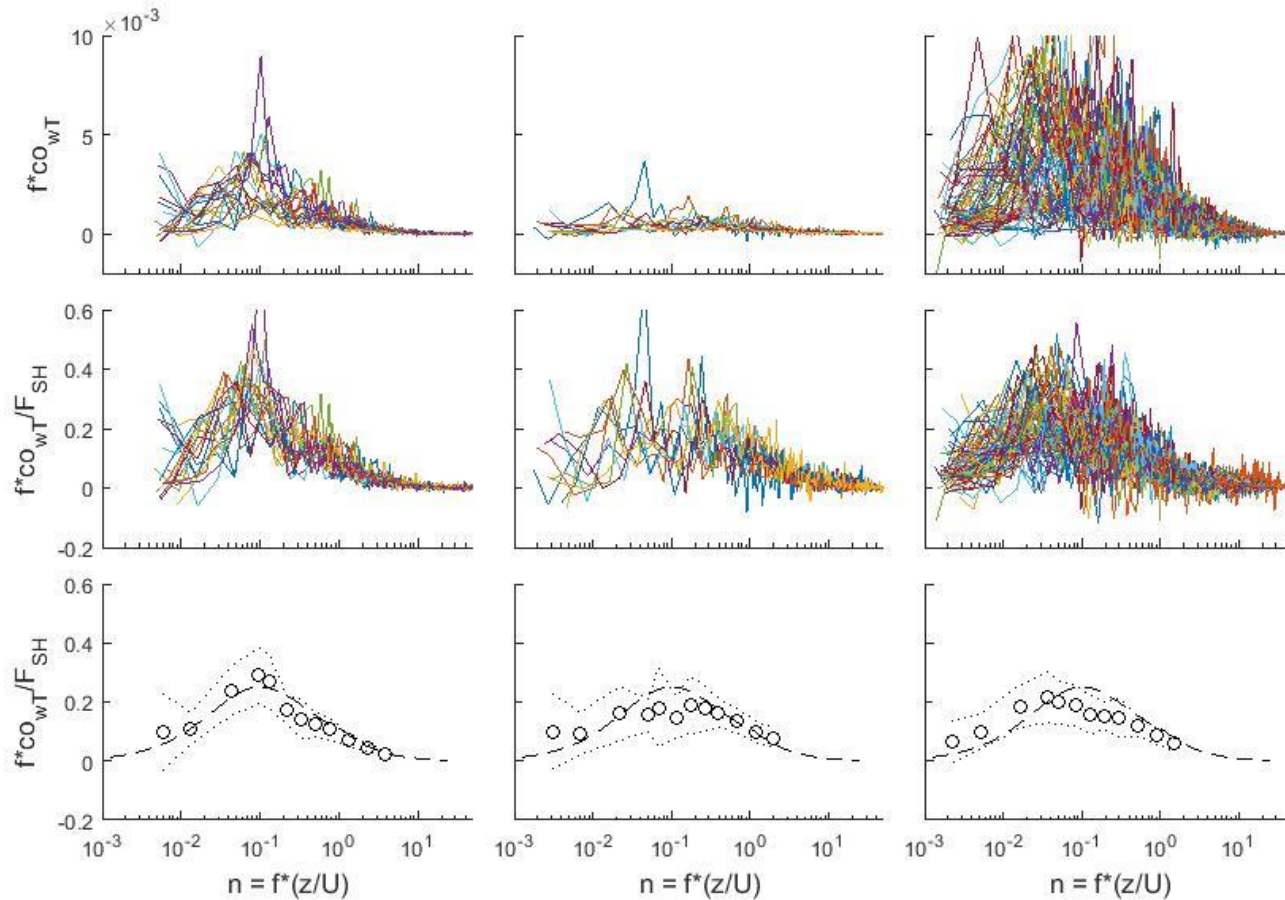
Figure 3.10 Frequency weighted co-spectra of vertical wind and temperature for flux intervals collected at Scripps Pier divided into three-time periods. The respective time-periods for columns 1-3 are DOY's 96-102, 104-109 and 114-117. Top: individual co-spectra for 13-minute flux intervals; Middle: Same as top except co-spectra have been normalized to the average flux during the interval. Bottom: Bin-averages of the flux normalized co-spectra (circles), ± 1 standard deviation (dotted line), and theoretical co-spectral shape from Kaimal *et al*. (1972), (Dashed line).

Transfer velocities

Transfer velocities for water vapor, sensible heat, SO_2 and momentum were calculated for each flux interval using equations 2.20-2.23. The transfer velocities for all parameters were positively correlated with wind speed, as expected given the increase in atmospheric turbulence associated with increased winds. A one-way least squares linear regression was used to obtain the transfer coefficient for each parameter and the uncertainty at the 95% confidence interval (*k/U*; Table 3.1). The transfer coefficient of momentum was the largest followed by water vapor, sensible heat and SO_2. Based on this analysis, the transfer coefficient of SO_2 was smaller than water vapor, sensible heat and momentum by 13, 8 and 35 % respectively. The transfer coefficients of sensible heat and water vapor within 5 % of each other.

An analysis of variance was computed to test if the slopes of the linear regressions were significantly different from each other at the 95 % confidence interval (Table 3.2). Based on the *F*-values from this test the slope of the regression to the momentum data were significantly different from the slopes of all the other regressions ($F > F_{crit}$, α=0.05). The slopes of the regressions of the water vapor, SO_2 and sensible heat data were not different from each other at the 95 % confidence level ($F < F_{crit}$ α=0.05).
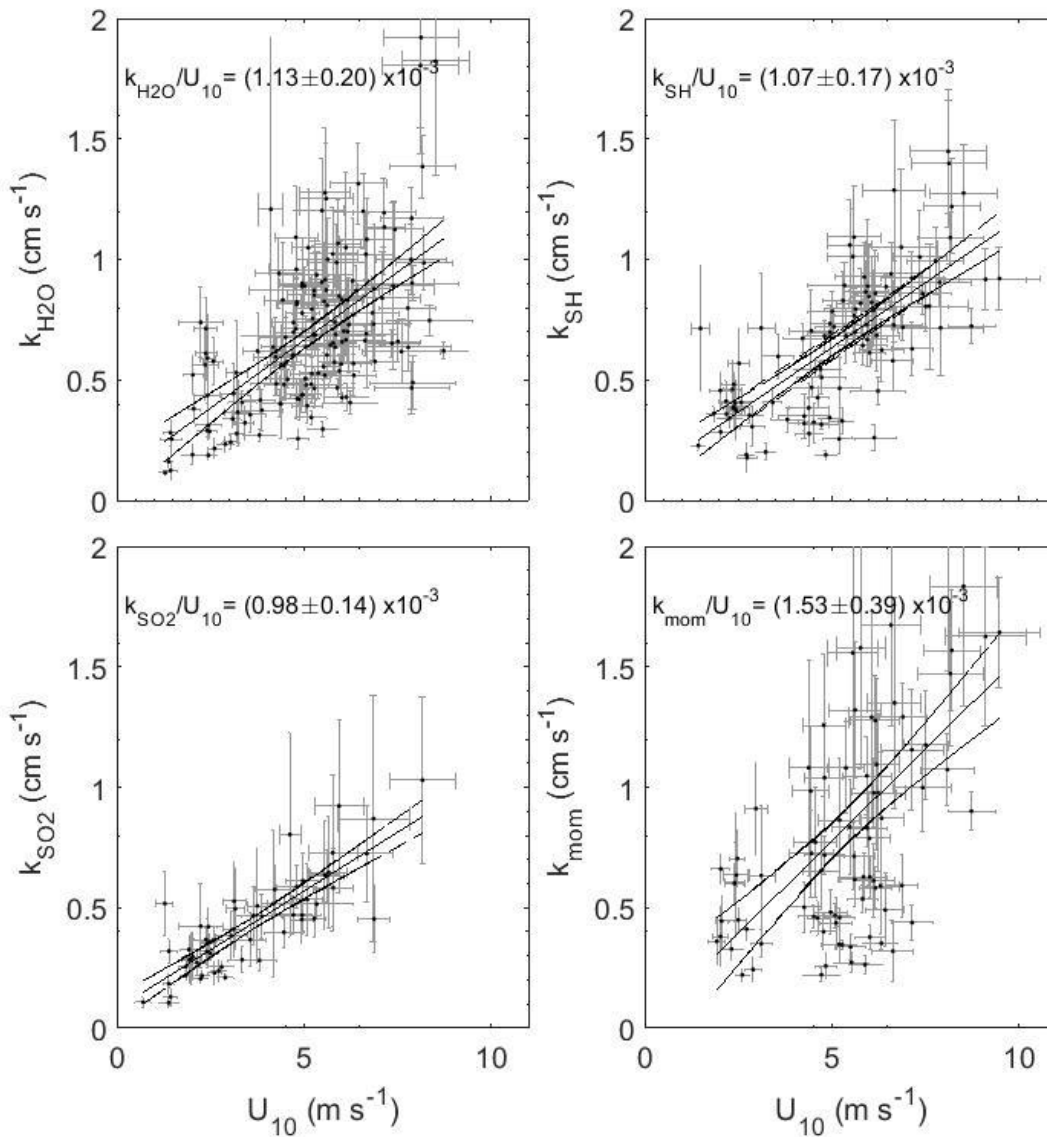
Figure 3.11 Transfer velocities collected at Scripps Pier for water vapor, sensible heat, SO_2 and momentum plotted against 10 m wind speed. The solid line is one-way least squares fit to the data and the curved lines represent the 95% confidence interval.

Table 3.1   Transfer coefficients (k/U_{10}) and 95% confidence interval obtained from field measurements at Scripps Pier.

Parameter	Transfer coefficients (k/U_{10}) x10^3
Water vapor (k_{H2O}/U_{10})	1.13±0.20
Sensible heat (k_{SH}/U_{10})	1.07±0.17
Sulfur dioxide (k_{SO2}/U_{10})	0.98±0.14
Momentum (k_{mom}/U_{10})	1.53±0.39

Table 3.2 Results of the analysis of variance test comparing the slopes of the linear regressions of the k vs U_{10} scatter plots.

	F	$F_{critical}$ ($\alpha=.05$)	p-value
SO_2 vs. H_2O	0.57	1.46	0.4512
SO_2 vs. Heat	0.37	1.49	0.5446
Heat vs. H_2O	0.11	1.34	0.7353
Momentum vs. SO_2	2.43	1.51	0.1216
Momentum vs Heat	2.23	1.41	0.1375
Momentum vs H_2O	1.57	1.39	0.2117

The comparison of wind-speed dependences suggests that sulfur dioxide has a lower transfer coefficient than either water vapor or sensible heat. That comparison utilized all the data that passed quality control collected during the Scripps deployment. It should be noted that data sets for the different constituents were not identical because of the elimination of intervals by the quality control criteria.

An alternative and more rigorous way to compare the transfer velocities of water vapor, SO_2 and sensible heat is to examine only flux intervals where multiple constituents passed quality control simultaneously. For these intervals, the physical conditions were identical for each parameter (atmospheric turbulence, sea state, etc.). Transfer velocities measured simultaneously were plotted against each other and two-way linear regressions were applied to the data. The results of this analysis showed k_{SO2} is smaller than both k_{H2O} and k_{SH} (Table 3.3; Figure 3.12).
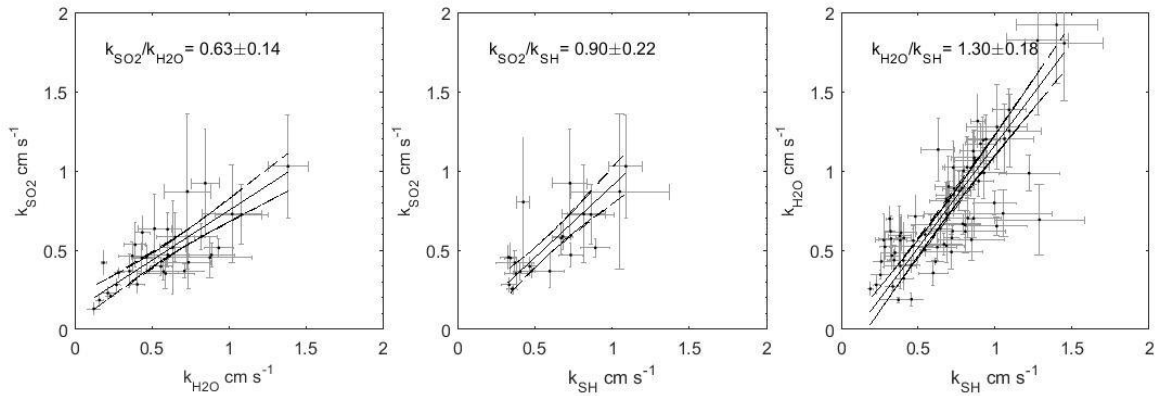
Figure 3.12 Transfer velocities plotted against each-other for intervals collected simultaneously at Scripps Pier.   The solid line is a two-way Deming regression and curved lines represent the 95 % confidence bounds of the regression. The error on the slope and intercept of the regressions is the 95 % confidence interval.

Table 3.3   Slope and 95 % confidence interval of regressions to k vs k in Figure 3.12.

k vs. k	Slope of fit to scatter plots	Number of data points
k_{SO2} vs. k_{H2O}	0.63 ± 0.14	33
k_{SO2} vs. k_{SH}	0.90 ± 0.22	21
k_{H2O} vs. k_{SH}	1.30 ± 0.18	77

The transfer coefficient for SO_2 is expected to be smaller than that of water vapor or sensible heat because the molecular diffusion coefficient of SO_2 in air is smaller than that of the other two. However, the ratio k_{SO2}/k_{H2O} from these results is surprisingly small given that diffusive resistance is only a small part of the overall air-side resistance to gas transfer.

Few intervals passed quality control simultaneously for sensible heat and SO_2. The error associated with k_{SO2}/k_{SH} was large and the ratio was not different from one as a result.

Water vapor and sensible heat diffuse at roughly the same rate in air and therefore should have similar transfer coefficients when measured under simultaneous conditions. The

ratio of k_{H2O}/k_{SH} was larger than one which may suggest a measurement bias in the sea surface/air temperature or water vapor mixing ratio.

As discussed in the introduction, previous studies have utilized the transfer of momentum as a proxy for the air-side resistance due to turbulence alone, sometimes referred to as the aerodynamic resistance. To compare the scalar transfer to momentum transfer, the transfer velocities to for flux intervals passing quality control simultaneously for the scalar quantities and momentum were plotted against each-other and linear two-way Deming regressions were fit to the data (Figure 3.13). The resulting regression slopes were all significantly less than one in each case (0.51±0.24, 0.68±0.16, 0.52±0.08). The regression to the k_{SH} vs. k_{mom} scatter plot significantly improved the R^2 value compared to the k_{SH} vs. U_{10} plot. There was no improvement for water vapor and SO_2. The regression slopes for the various scalars against momentum are not statistically different from each other at the 95 % confidence level.
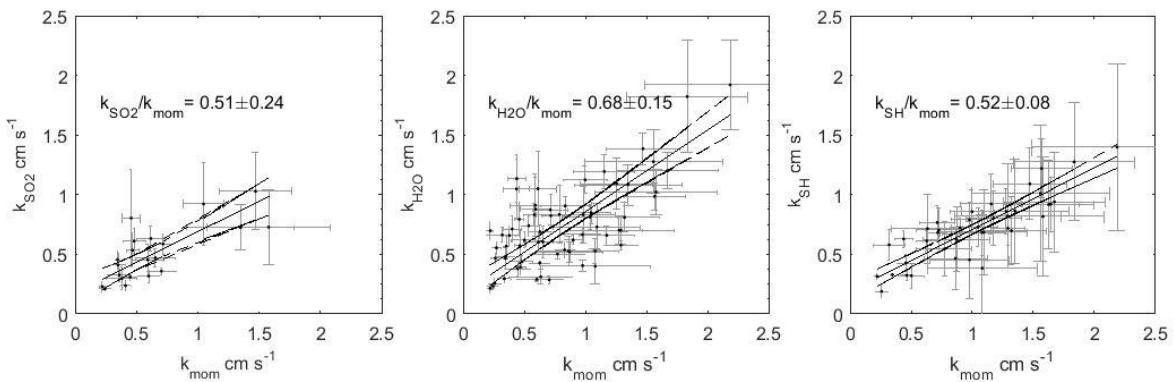
Figure 3.13 Transfer velocities for the scalar parameters plotted against the aerodynamic limit (k_{mom}) for intervals collected simultaneously at Scripps Pier. Solid line is a two-way Deming regression, the error on the slope and intercept are 95 % confidence intervals. The curved lines are 95 % confidence bounds on the regression.

Table 3.4 Slope and 95 % confidence interval for regressions to k vs k in Figure 3.13.

k vs. k	Slope of fit to scatter plots	Number of data points
k_{SO2} vs. k_{mom}	0.51±0.24	21
k_{H2O} vs. k_{mom}	0.68±0.15	66
k_{SH} vs. k_{mom}	0.52±0.08	41

3.3. Discussion

The Scripps data show the transfer velocities for all parameters scale with wind speed. This wind speed dependence likely results from two effects. First, increasing wind speed results in increasing turbulent transport across the turbulent part of the surface layer. Second, turbulence near the surface may reduce the depth of the interfacial viscous layer above the sea surface where diffusive behavior may limit transport of the scalars (sensible heat, water vapor, and sulfur dioxide).

The data also indicate that scalar transfer velocities (SO_2, water vapor, sensible heat) are smaller than the momentum transfer velocity when both are observed under simultaneous or similar conditions. This difference is significant for all three scalars at the 95 % confidence interval (Figure 3.13). One might expect this general relationship because momentum can be transferred by multiple processes that are not applicable to the transfer of scalars. For example, form drag involves momentum transfer as a result of pressure forces against waves, which does not result in enhanced transfer of scalars (Kondo, 1975; Liu *et al.*, 1979).

The Scripps data gives an average ratio of k_{scalar}/k_{mom}=0.57±0.29. By comparison, the COARE algorithm, which is tuned to open-ocean momentum and latent heat flux data, predicts a ratio the k_{H2O}/k_{mom} =0.85.

Sulfur dioxide transfer velocities are lower than those of water vapor and sensible heat in this data set. This result was significant at the 95 % CI when SO_2 transfer velocities were regressed against water vapor transfer velocities (Figure 3.12). However, this result was not significant when SO_2 transfer velocities were regressed against sensible heat transfer velocities. There was too much scatter and limited data to see a statistically significant difference between the SO_2 and sensible heat transfer velocities. Lower transfer velocities for SO_2 are expected, because the molecular diffusivity of SO_2 in air is roughly half than that of water vapor and sensible heat, so transport across the viscous interfacial layer should be slower. However, the magnitude of the difference in gas transfer velocities between SO_2 and water vapor is far larger than one would expect from molecular diffusivity. For example, the observed ratio of k_{SO2}/k_{H2O} =0.63 ± 0.14 is essentially equal to the ratio of the molecular diffusivities implying that transport through the marine surface layer is a purely diffusive process. This is not possible, given that the surface layer is turbulent. For example, the typical log-normal vertical profiles of scalars in the surface layer demonstrate that turbulent mixing is a significant component of the overall resistance (Von Karman., 1930).

Sulfur dioxide transfer velocities were lower than sensible heat transfer velocities. However, the results were only significant at the 75 % confidence interval. Sulfur dioxide diffuses at roughly half the rate of heat in air, so the result qualitatively agrees with the

theory of diffusive resistance in the interfacial layer. The uncertainty in the regression is due to the small sample size (21 simultaneous intervals).

3.4. **Conclusion**

The Scripps deployment was successful in terms of demonstrating the capability to measure SO_2 at ambient levels with the CIMS instrument. Eddy covariance flux measurements of SO_2, water vapor and sensible heat were successfully measured with our flux package, as evidenced by the quality of the co-spectra. The absence of upward SO_2 fluxes confirmed the hypothesis that SO_2 concentrations in sea water are negligible.

The data provide evidence that sulfur dioxide transfer velocities are smaller than those of water vapor or sensible heat. This result is qualitatively consistent with gas transfer theory suggesting slower diffusing gases have higher resistance in the interfacial sublayer. However, the data set available for direct comparison was limited in terms of the quantity of data and the wind speed range. The results suggest that this is a useful approach for studying air-side resistance, but that the results would be improved if it was implemented in an environment with a wider range of wind speeds and larger air/water temperature differences.

It is notable that SO_2 exhibited the least scatter and smallest error of the three constituents in terms of its relationship to wind speed (Table 3.1, Figure 3.11). The thermodynamic gradient for SO_2 is purely dependent on atmospheric concentrations and calculations of k_{SO2} are not subject to measurements uncertainty associated with sea surface temperature

measurements. This may have led to a more precise measurement of k_{SO2} relative to k_{H2O}

and $k_{SH,}$ both of which are dependent on sea surface temperature measurements

4. Flux measurements at the Duck pier

4.1. Overview

The second field campaign was carried out at the U.S. Army Corps of Engineers Field Research Facility in Duck, NC. Duck is located in the Outer Banks barrier islands off the coast of North Carolina. The major goal of the second field campaign was to expand our data-set across a broader range of wind speeds. An analysis of wind speed and direction at the study site for the years 2012-2014 show that winter and early spring are generally characterized by strong winds from a northerly direction which are ideal for flux measurements. This field research facility maintains a research pier with a meteorological tower suitable for attaching our eddy flux package and a shed at the end of the pier to house our CIMS instrument and associated electronics.

A second goal of this experiment was to improve the precision and accuracy of the sea surface temperature measurement. The infrared radiometer used in this study can measure skin temperature of the ocean to within 0.2 °C of uncertainty. This technique will improve our ability to accurately measure the air/sea thermodynamic differentials driving sensible heat and water vapor fluxes. Resulting estimates of water vapor and sensible heat transfer coefficients should also improve.

4.2. Results

Meteorological and oceanographic conditions

Weather conditions at the sampling location were characterized by the periodic passage of cold fronts from the northwest. Frontal passages occurred on average every four days (~8 events in total), due to cyclonic flow around a recurring low-pressure system off the North Atlantic coast. Virtually all valid flux data collected during this study were obtained during and just after frontal passages, primarily because of the quality control requirement that winds lie in the sector from 125-305° to ensure offshore flow and minimize flow distortion by the pier. All the frontal passages were accompanied by a sharp drop in air temperature, increase in wind speed, and a gradual shift in wind direction from the south or southeast to the north (Figure 4.1 & 4.2). The cold air temperatures associated with frontal passages resulted in a small temperature differential between the sea surface and air.

Relative humidity and SO_2 mixing ratio were variable during these events and dependent on the air-mass trajectory. During the frontal events on DOY's 95 and 105 relative humidity decreased markedly because of strong air-mass subsidence into the boundary layer. This contrasts with the high humidity observed on DOY 99 when air-masses had no subsidence and were in contact with the sea surface prior to arriving at the study site. Air masses originating over the north-east US, such as on DOY 105, were associated with high levels of SO_2 due to pollution from fossil fuel combustion. During frontal passages SO_2 levels averaged 145 pmol mol^{-1}, considerably higher than the average levels (83 pmol mol^{-1}) observed between events.

NOAA HYSPLIT MODEL
Backward trajectories ending at 2100 UTC 07 Apr 15
GDAS Meteorological Data

Figure 4.1 Back trajectories (48 hr) starting at Duck Pier for the frontal passage that occurred on April 4th ending April 7th. The air masses reaching the pier shift from a southerly to a northerly origin, (top panel) and experience subsidence as they approach the study site (bottom panel).

Figure 4.2 Time series plot showing bulk meteorological and SO_2 data collected at Duck Pier from March 18 - 24, 2015 (DOY 75-111). The grey bands indicate frontal passages and black data points had an average wind direction between 125-305°. Data are sparse at the beginning of the study due a few electronics failures.

CIMS instrument performance

The average signal from ambient and isotopic SO_2 was 2.6×10^4 and 2.7×10^4 cps respectively for intervals passing quality control. This resulted in an average SO_2 mixing ratio of 97 ± 92 pmol mol^{-1} and an average sensitivity of 165 ± 57 cps pmol^{-1} mol. There was an inverse relationship between water vapor mixing ratio and instrument sensitivity. There was also an inverse relationship between SO_2 mixing ratio and instrument sensitivity (Figure 4.4). This behavior was also observed during the Scripps campaign and the cause is not understood.

The mass flow controller controlling the inlet flow did not maintain a steady flow as the study progressed (Figure 4.3). It is possible the driers were slowly becoming clogged due to sea spray and/or particulates from tree pollen (large amounts of tree pollen were observed deposited on the entrance of the inlet). The variance of the inlet flow during the study was only 2 % of the mean flow and not anticipated to have a large effect on the inlet attenuation characteristics. Inlet delays were calculated on an interval by interval basis to account for the changing transit times over the course of the study.

73
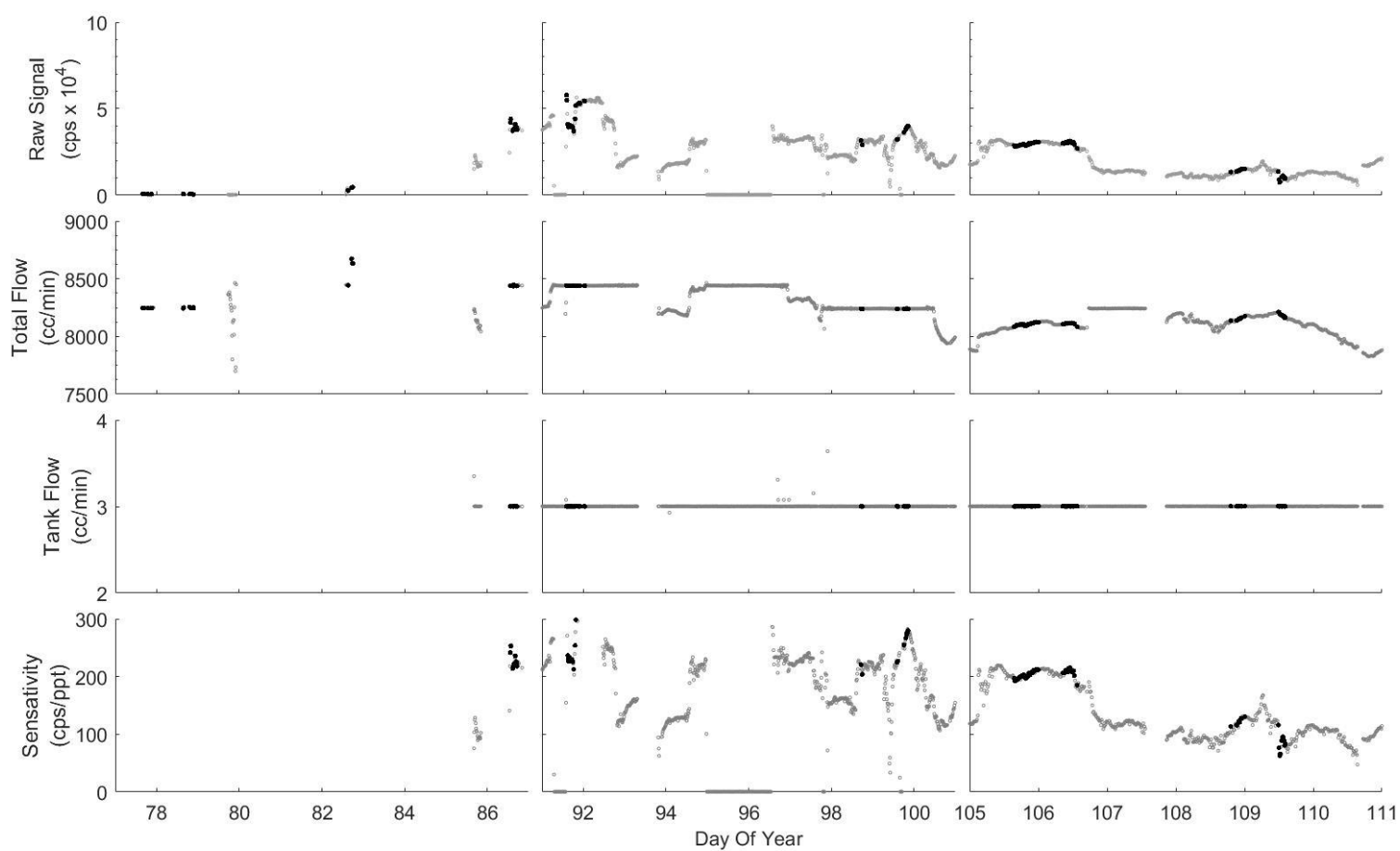
Figure 4.3 Time series of the CIMS instrument performance during the Duck campaign. The top row shows average counts at m/z 114 from the isotopic standard ($^{34}SO_2$). Rows two and three shows the tank flow and total inlet flow respectively. The fourth row shows the sensitivity of the CIMS instrument (cps/pmol mol^{-1}). Black data points passed quality control criteria for SO_2 fluxes.
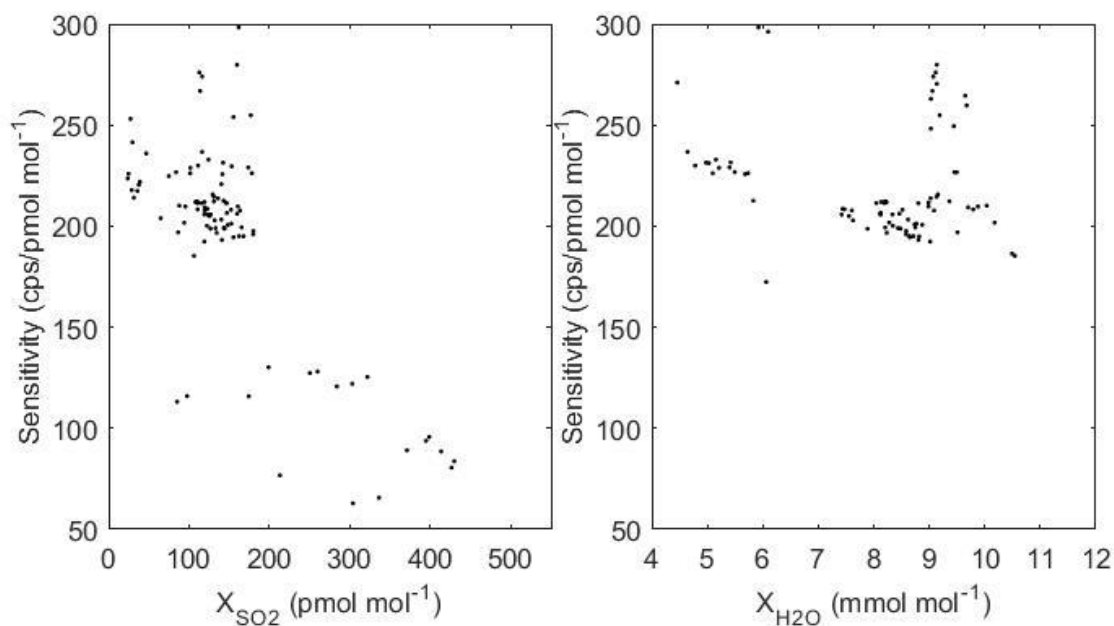
Figure 4.4 Sensitivity vs. SO$_2$ mixing ratio (left) and sensitivity vs H$_2$O mixing ratio (right) during the Duck deployment. The data shown passed quality control for the respective parameter.

Air-sea thermodynamic differentials and fluxes

The average SO$_2$ mixing ratio during the study was $1.01\times10^2 \pm 1.15\times10^2$ pmol mol^{-1}. All SO$_2$ fluxes passing quality control were downward into the ocean even when SO$_2$ concentrations were small as on DOY's 87 and 97. For the first eight days of the study flux measurements were made but the isotopic standards were not used. During this time SO$_2$ mixing ratio calculations were not possible, however transfer velocity calculations were still possible using the raw signal at m/z 112 from ambient SO$_2$ (Figure 4.5).

The average temperature differential between the bulk atmosphere at 10 m and the sea surface was -4.7 $\pm$ 4.3 °C. During frontal passages from the north the air/sea temperature differentials were very small because of the cold air associated with these fronts. The

majority of intervals that passed quality control criteria for sensible heat fluxes were during frontal passages from the north because of the requirement that wind directions lie between 125-305°. The mean temperature differential for intervals passing quality control was 1.3 ± 0.6 °C and the average heat flux was 11.7 ± 7.1 W m^{-2}. All heat fluxes were upward for intervals passing quality control. The small temperature differentials meant good quality heat flux data were limited during the campaign. Only 68 of the ~ 2000 flux intervals passed quality control (Figure 4.6).

The average difference between water vapor mixing ratio at 10 m and the mixing ratio at the saturation vapor pressure at the sea surface temperature was -0.6 ± 4.7 mmol mol^{-1} with a range from -14.5 to 28.2 mmol mol^{-1}. Water vapor fluxes went into and out of the ocean over the course of the study but nearly all intervals that passed quality control had upward fluxes (Figure 4.7).
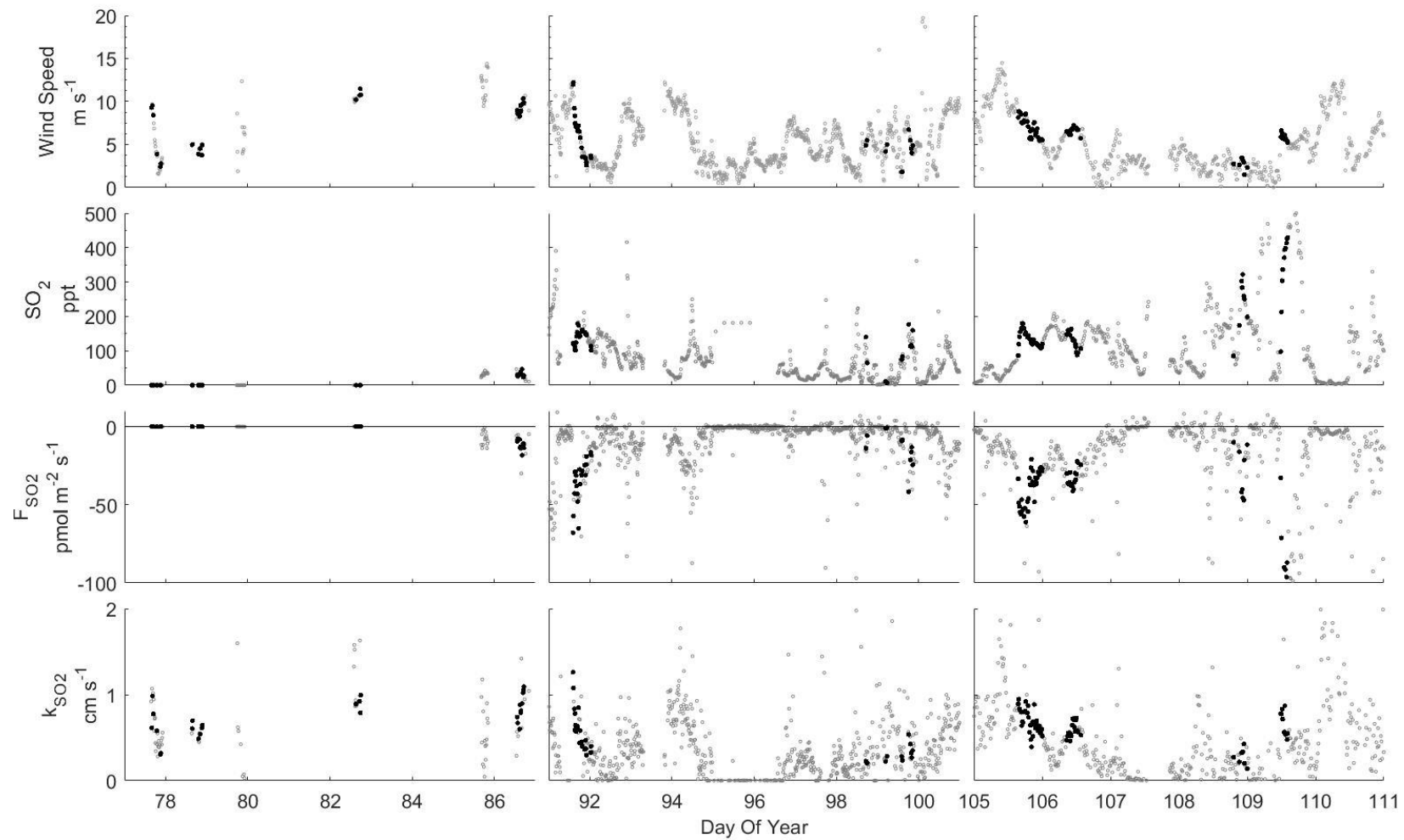
Figure 4.5 Time series of parameters related to SO$_2$ fluxes collected at Duck Pier from March 18– April 21. Black points indicate the interval passed quality control.
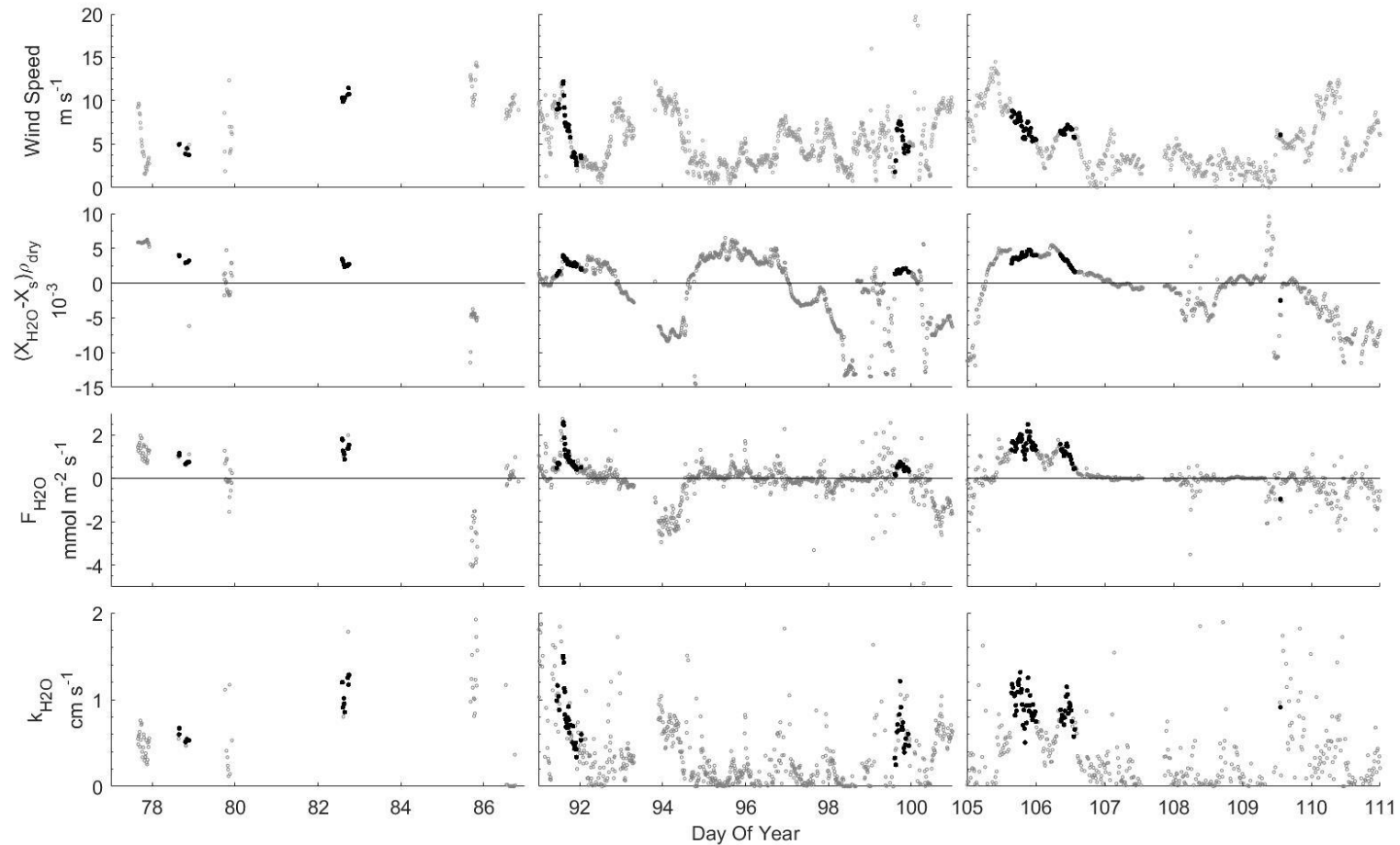
Figure 4.5 Time series of parameters related to H₂O fluxes collected at Duck Pier from March 18– April 21. Black points indicate the interval passed quality control.
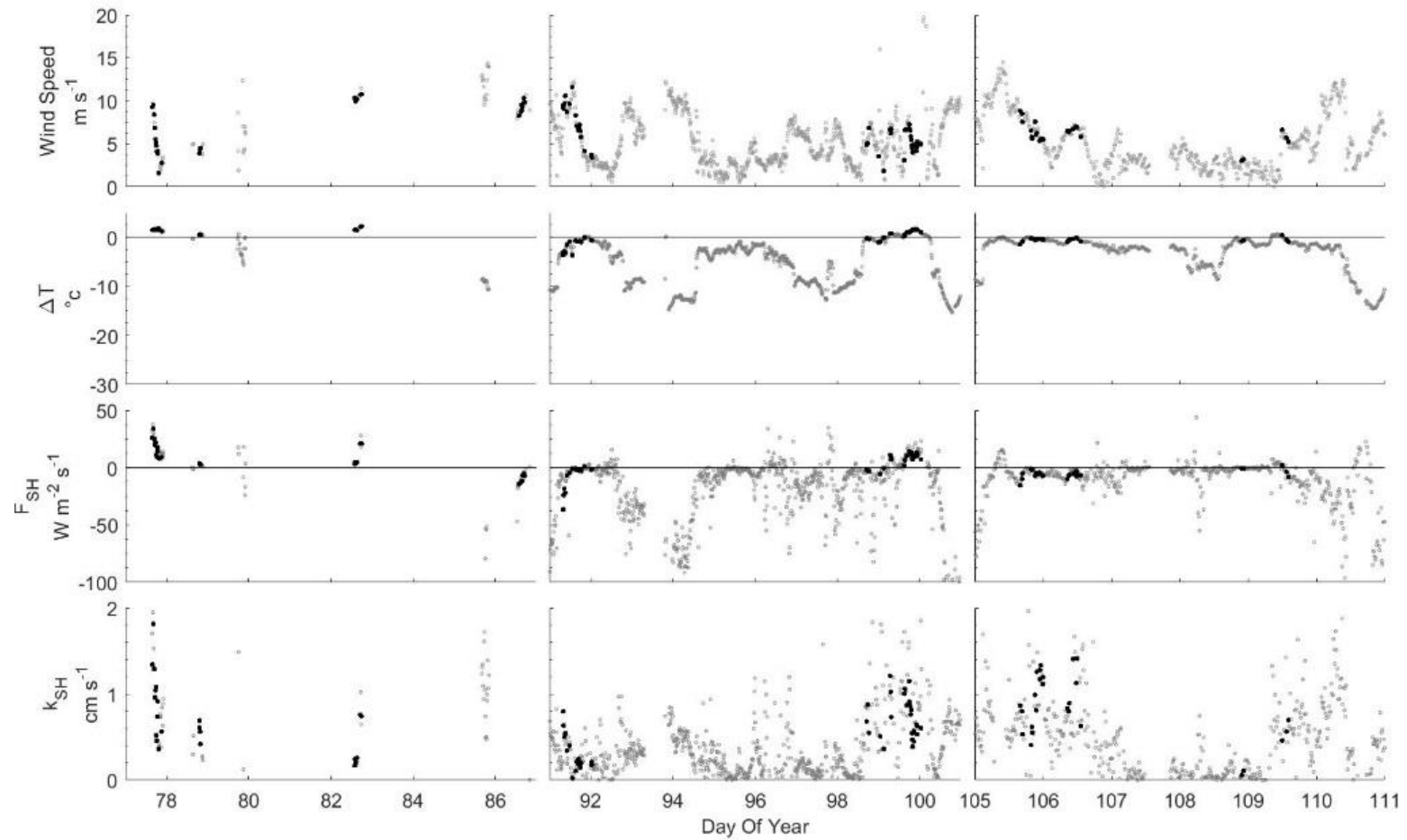
Figure 4.5 Time series of parameters related to sensible heat fluxes collected at Duck Pier from March 18– April 21. Black points indicate the interval passed quality control.

78

Co-spectra

In this section the co-spectra from the scalar parameters are examined to assess the quality of our flux measurements. All SO_2 co-spectra passing quality control were negative indicating fluxes were always from the atmosphere to the ocean (Figure 4.8). All water vapor co-spectra were positive indicating fluxes were always from the ocean to the atmosphere (Figure 4.9). Sensible heat co-spectra were bi-directional (Figure 4.10). Average co-spectra from this experiment have a similar shape to the theoretical co-spectra from Kaimal *et al*. (1972) to within one standard deviation for all parameters (Figure 4.8-4.10). This indicates that fluxes were successfully measured in the marine boundary layer. Sulfur dioxide co-spectra agreed well with theoretical co-spectra from Kaimal *et al.* (1972) at high frequencies (Figure 4.9). This result shows that there was negligible attenuation of fluctuations in SO_2 mixing ratio in the gas inlet.
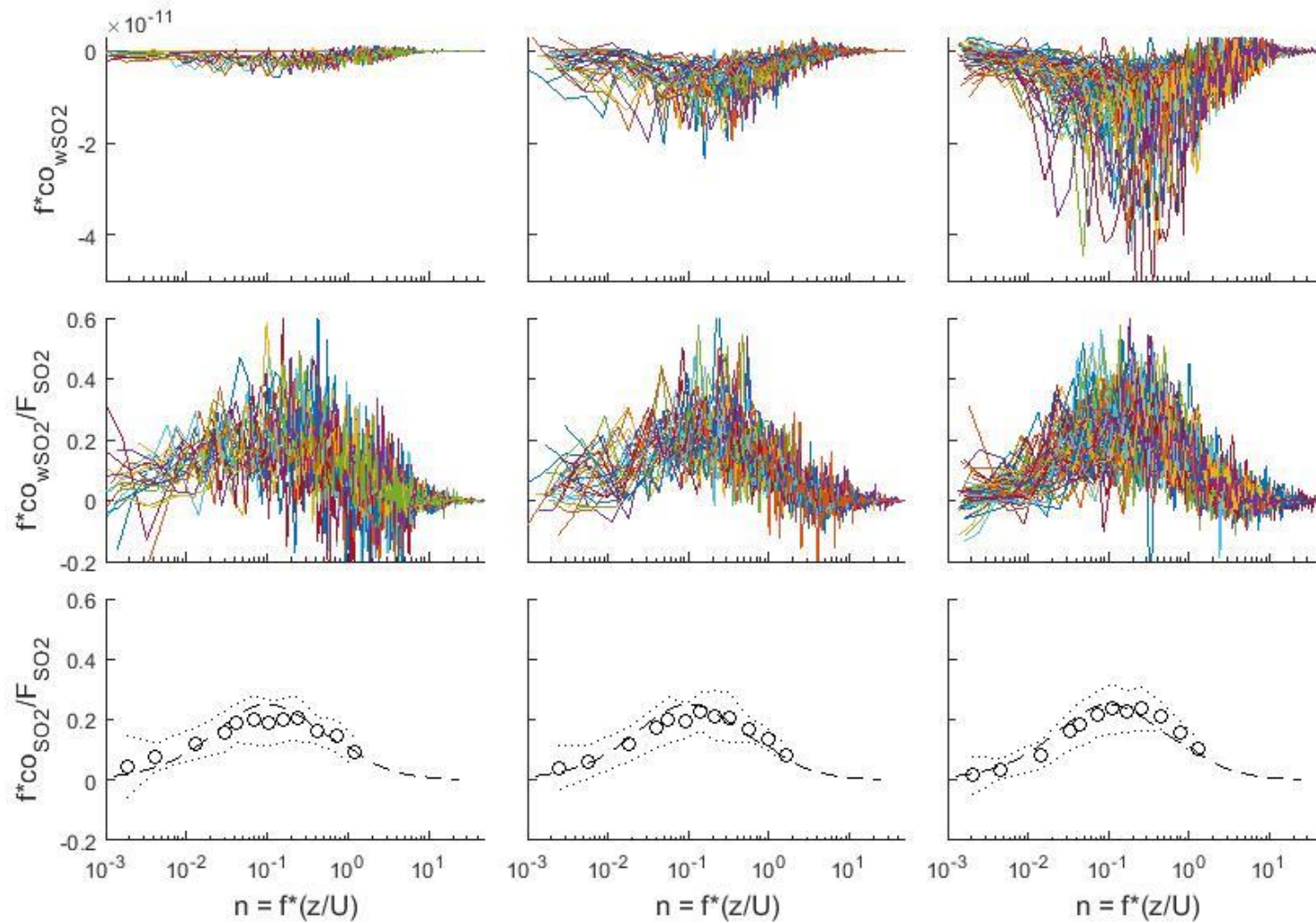
Figure 4.8 Frequency weighted co-spectra of vertical wind and sulfur dioxide for flux intervals collected at Duck Pier divided into three time-periods. The respective time-periods for columns 1-3 are DOY's 77-87, 91-101 and 105-111. Top: individual co-spectra for 13-minute flux intervals; Bottom: average co-spectrum (solid black line), ± 1 standard deviation (dotted line), and co-spectral shape from Kaimal *et al.* (1972), (Dashed line).
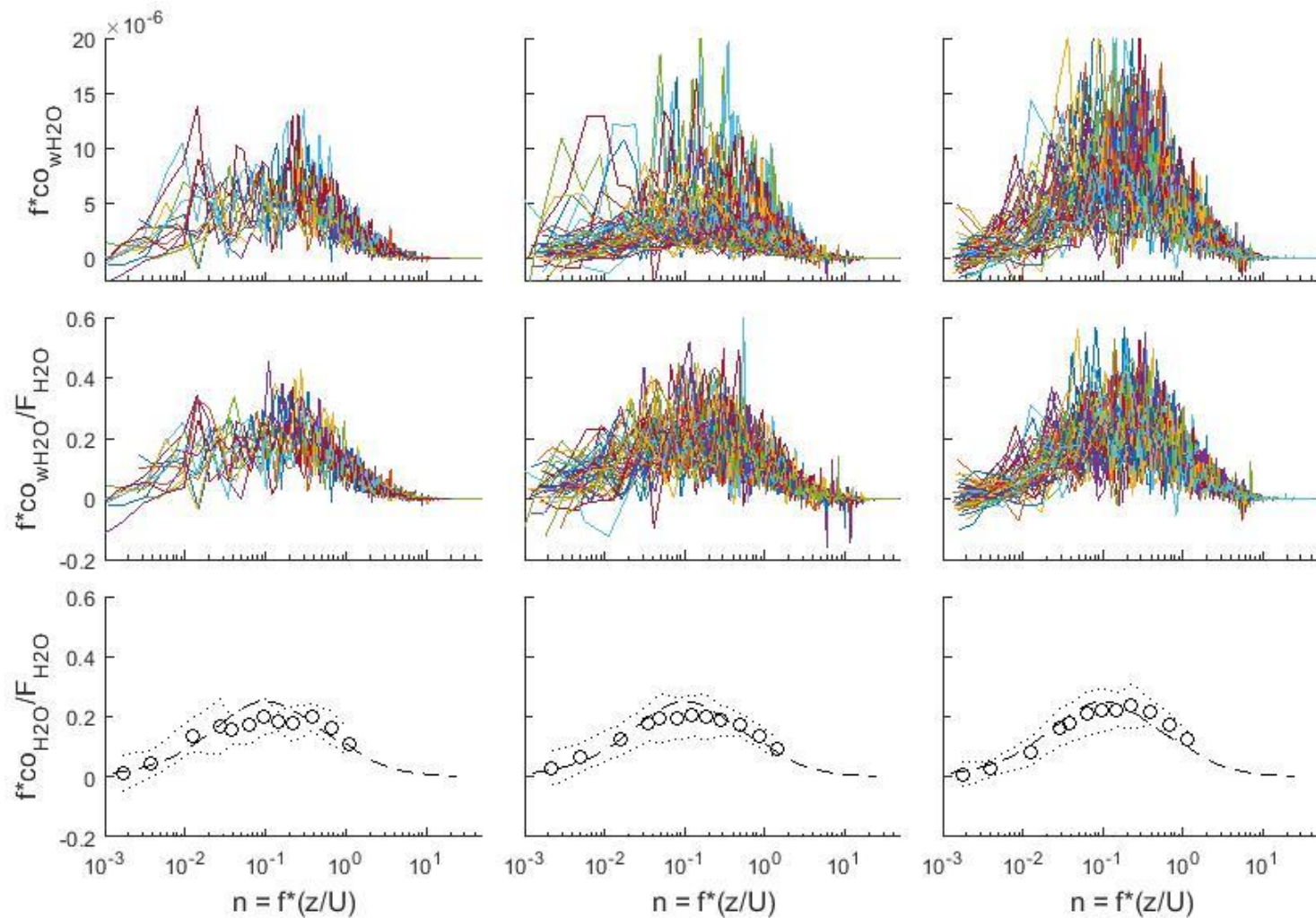
Figure 4.9 Frequency weighted co-spectra of vertical wind and water vapor for flux intervals collected at Duck Pier divided into three time-periods. The respective time-periods for columns 1-3 are DOY's 77-87, 91-101 and 105-111. Top: individual co-spectra for 13-minute flux intervals; Bottom: average co-spectrum (solid black line), ± 1 standard deviation (dotted line), and co-spectral shape from Kaimal *et al.* (1972), (Dashed line).
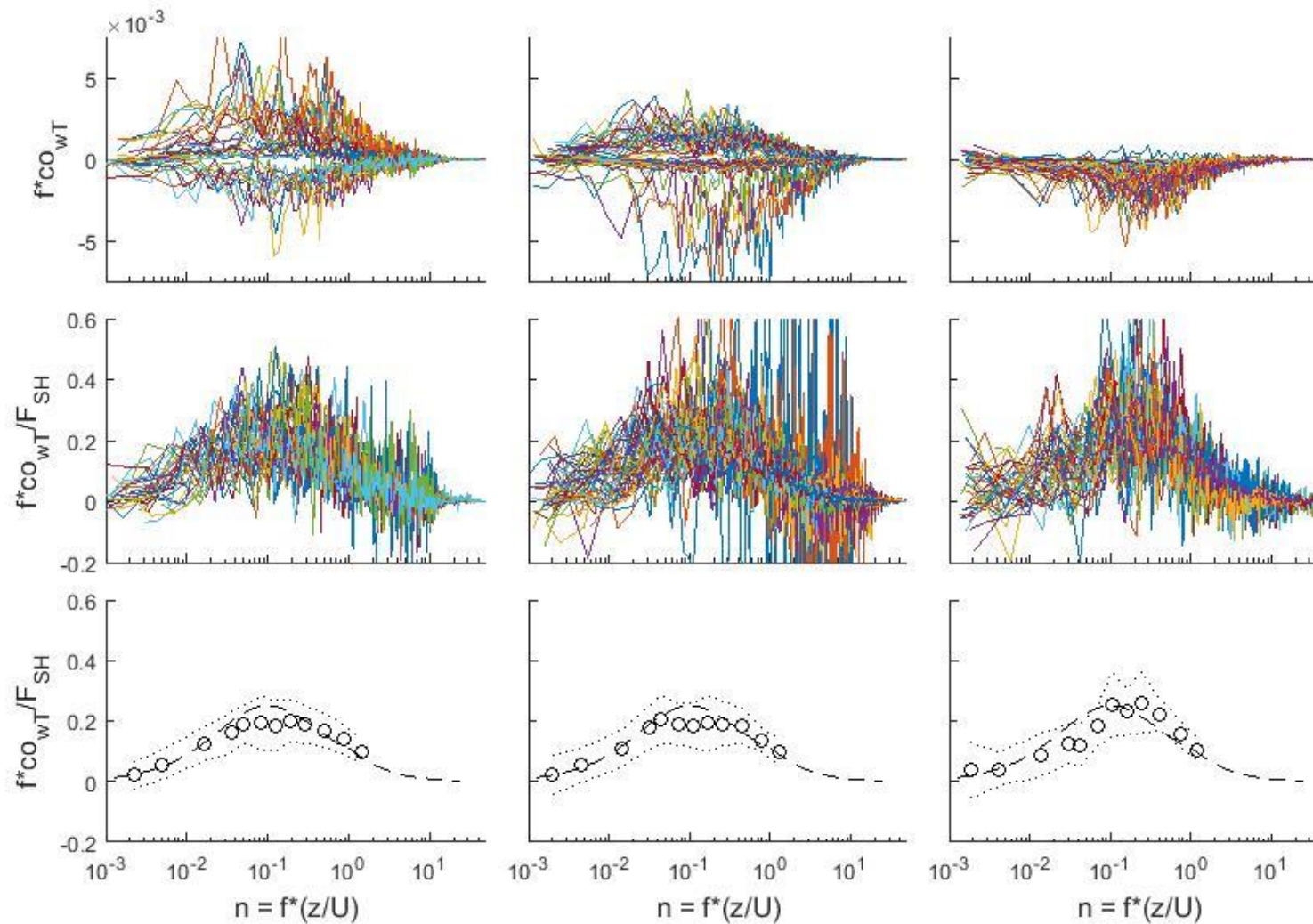
Figure 4.10 Frequency weighted co-spectra of vertical wind and sensible heat for flux intervals collected at Duck Pier divided into three time-periods. The respective time-periods for columns 1-3 are DOY's 77-87, 91-101 and 105-111. Top: individual co-spectra for 13-minute flux intervals; Bottom: average co-spectrum (solid black line), ± 1 standard deviation (dotted line), and co-spectral shape from Kaimal *et al.* (1972), (Dashed line)*.*

Transfer velocities

Transfer velocities for SO_2 water vapor, sensible heat and momentum were calculated using equations 2.20-2.23. Transfer coefficients (k/U_{10}) were calculated by fitting one-way linear regressions to the scatter plots of k vs U_{10} (Figure 4.11). This analysis showed that the momentum transfer coefficient was the largest followed by water vapor and SO_2 (Table 4.1). An analysis of variance was computed to test for statistical significant differences between the linear regressions. All the regressions were different from each other at the 95 % CI except for the sensible heat and momentum regressions (Table 4.2).

There were relatively few data points that passed quality control for sensible heat. The uncertainty in the regression to the sensible heat data were large compared to the other parameters as a result. The poor quality of sensible heat data were likely because of small air/sea temperature differentials that occurred during the passage of cold fronts from the north. Unfortunately, winds were from a suitable direction for eddy covariance flux measurements during such frontal passages from the north. The remaining results and discussion exclude sensible heat due to the low quality of the data-set.
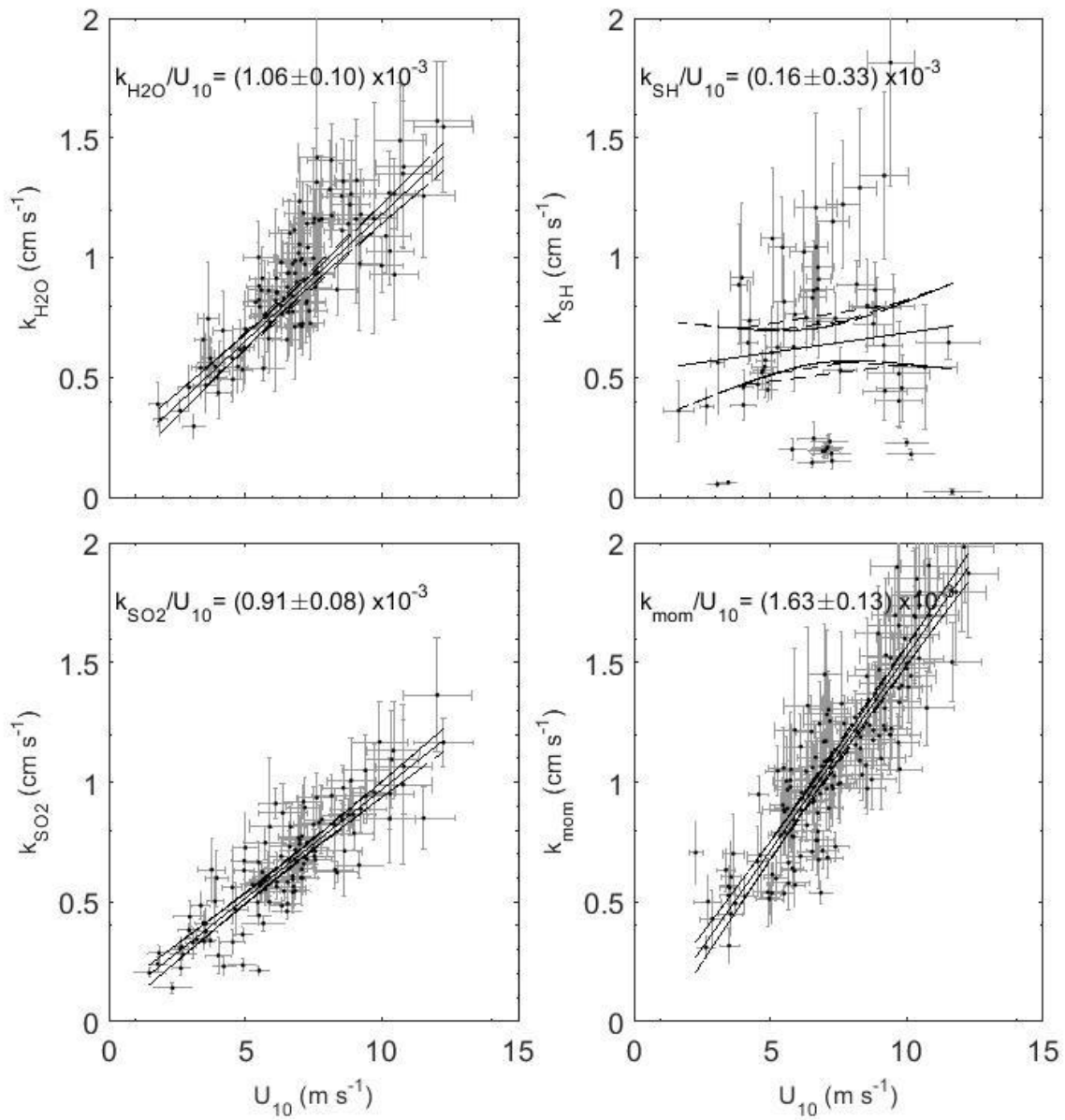
Figure 4.11 Transfer velocities for water vapor, sensible heat, SO_2 and momentum measured at Duck Pier. Each parameter is plotted against 10 m wind speed. The solid line is one-way least squares fit to the data and the curved lines represent 95% confidence bounds on the regression.

Table 4.1 Transfer coefficients (k/U_{10}) and 95% confidence interval obtained from field measurements during the Duck field campaign study.

Parameter	Transfer coefficients (k/U_{10}) x10^3
Water vapor (k_{H2O}/U_{10})	1.06±0.10
Sensible heat (k_{SH}/U_{10})	1.65±0.33
Sulfur dioxide (k_{SO2}/U_{10})	0.91±0.08
Momentum (k_{mom}/U_{10})	1.63±0.13

Table 4.2 *F* statistic and *p* value from the analysis of variance test comparing the linear regressions from Figure 4.11.

Comparison	F	F-critical	p value
SO_2 vs. H_2O	4.75	1.05	0.0303
SO_2 vs. mom	66.56	1.32	5.27e-15
H_2O vs. mom	33.53	1.33	1.22e-8

The wind speed analysis indicates that SO_2 transfer velocities are smaller than the water vapor transfer velocities. This result is broadly consistent with the results from the Scripps deployment. These results were significant at the 95 % confidence interval ($F > F_{crit}$). Water vapor and SO_2 transfer velocities were compared by identifying intervals passing quality control simultaneously for both parameters and plotting k_{SO2} vs. k_{H2O} (Figure 4.12). A two-way Deming regression to the data showed that $k_{SO2}/k_{H2O} = 0.80 \pm 0.07$ ($R^2 = 0.83$).
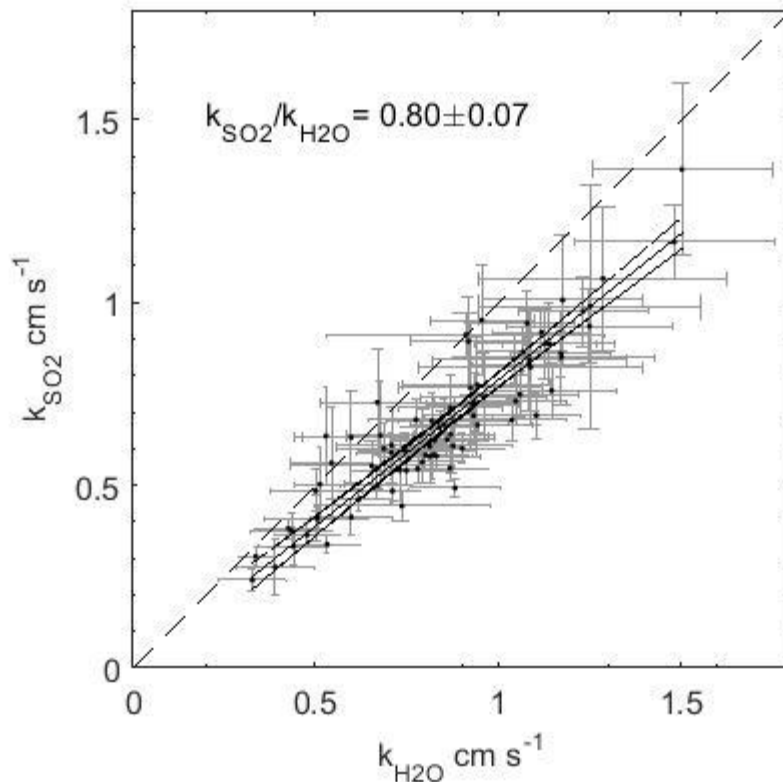
Figure 4.12 Sulfur dioxide transfer velocities plotted against water vapor transfer velocities for intervals collected simultaneously at Duck Pier. The solid line is a two-way Deming regression fit to the data and the curved lines represent the 95 % confidence bounds of the regression. The dashed line has a slope of 1. The errors on the slope and intercept of the regressions is the 95 % confidence interval.

Table 4.3 Slope and 95 % confidence interval for slope of regression to k_{SO2} vs k_{H2O}.

k vs. k	Slope of fit to scatter plots	Number of data points
k_{SO2} vs. k_{H2O}	0.80±0.07	82

The wind speed analysis showed that water vapor and SO_2 transfer velocities were significantly smaller than momentum transfer velocities. To compare the scalar transfer velocities to momentum transfer velocities intervals passing quality control simultaneously for momentum and either water vapor or SO_2 were identified. The scalar transfer

velocities and momentum transfer velocities were plotted against each other in a scatter plot. A two-way linear Deming regression was fit to the data. The results of this analysis indicate that SO_2 and water vapor transfer velocities are 54 % and 58 % of momentum transfer velocities.
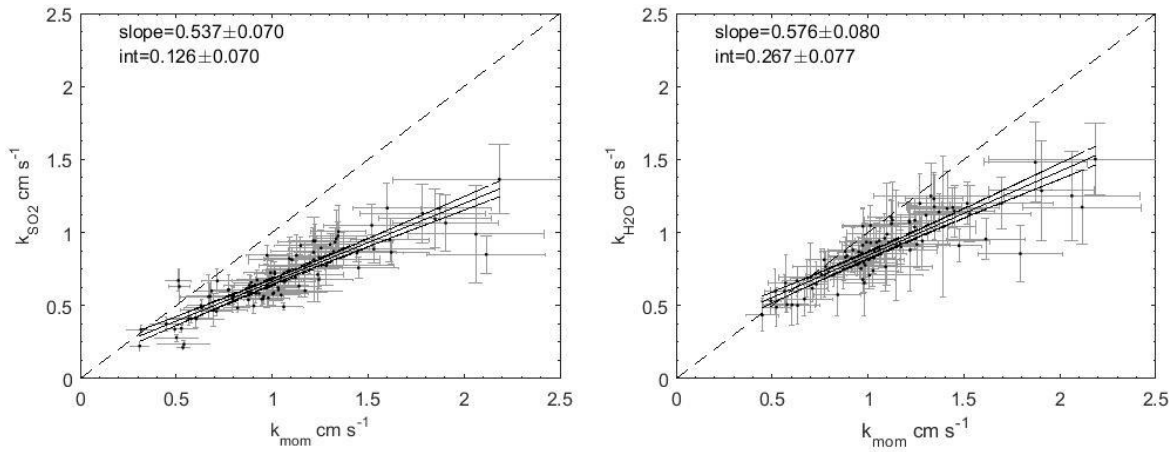
Figure 4.13 Transfer velocities for the scalar parameters plotted against the aerodynamic limit (k_{mom}) for intervals collected simultaneously at Duck Pier. The solid line is a two-way Deming regression, the error on the slope and intercept are 95 % confidence intervals. The curved lines are 95 % confidence bounds on the regression and the dashed line has a slope of 1.

4.3. Discussion

There are three important observations from the Duck study: 1) transfer velocities for all parameters increased with increasing wind speeds in a linear fashion (Figure 4.11), 2) transfer velocities for momentum were larger than those for the scalar parameters (water vapor and sulfur dioxide), (Figure 4.13), and 3) The most important observation of this study was that SO_2 transfer velocities are significantly smaller than water vapor transfer velocities (Figure 4.12). These three observations are in general agreement with the observations from the dataset collected at Scripps pier.

The data set collected at Duck Pier is better than the Scripps data set in three significant ways: 1) the data set was much larger, 2) the range of wind speeds observed at the study site was significantly broader and 3) measurements of air temperature, sea surface temperature and sensor height were more precise. These improvements lead to a lower uncertainty in the analyses performed on this data relative to the analysis on the Scripps data. The linear regression of k against U_{10} for water vapor, momentum and SO_2 were statistically different from each-other at the 95 % confidence interval. The uncertainty associated with the linear regression of k_{SO2} against k_{H2O} was small (8.5 %) relative to the same analysis of the Scripps data (22.1 %). The only way this data set was worse than the Scripps data set was the small temperature differentials between the bulk atmosphere and the sea surface which resulted in large uncertainty associated with the regression of k_{SH} against U_{10}.

4.4. Conclusion

The study was successful in regard to expanding the flux dataset across a broader range of wind speeds. The broader range of wind speeds and improved sea surface and air temperature measurement allowed for a statistically measurable difference between water vapor, SO_2 and momentum transfer velocities. Sulfur dioxide transfer velocities were ~ 20 % lower than water vapor transfer velocities.

5. Comparison of data from Scripps and Duck field campaigns

5.1. Overview

This chapter compares the data from the Scripps and Duck field campaigns with the goal of identifying common trends between the two data-sets. Consistent results between the two datasets validates the experimental design and increases confidence in the conclusions drawn about the physical processes at the air sea interface. The important questions that this comparison is intended to answer are, 1) do both data sets show evidence of turbulent transport through the marine surface layer? 2) is there an observable difference between transfer velocities of the scalar parameters and momentum? and 3) is there an observable difference between the transfer velocities of the scalar parameters (water vapor, SO_2, sensible heat)?

5.2. Using friction velocity as a basis for comparison of field studies

Gas transfer velocities from various studies are usually compared using wind speed as the independent variable. However, the relationship between wind speed and surface roughness can vary significantly between the open ocean and coastal environments and among different coastal sites because of the differences in water depth, fetch, tidal currents, surfactants, wave properties, etc. Thus, the turbulent properties of the atmospheric surface layer in coastal environments are not well described by wind speed alone. Here friction velocity (u_*) is used as the independent variable, (Equation 5.1).

$$u_* = \sqrt{\frac{F_{mom}}{\rho}}$$ (5.1)

Friction velocity computed from observations of momentum flux are used as the basis on which to compare gas transfer coefficients from Scripps and Duck to each other and to various model parameterizations intended for use over the open ocean (see Chapter 6).
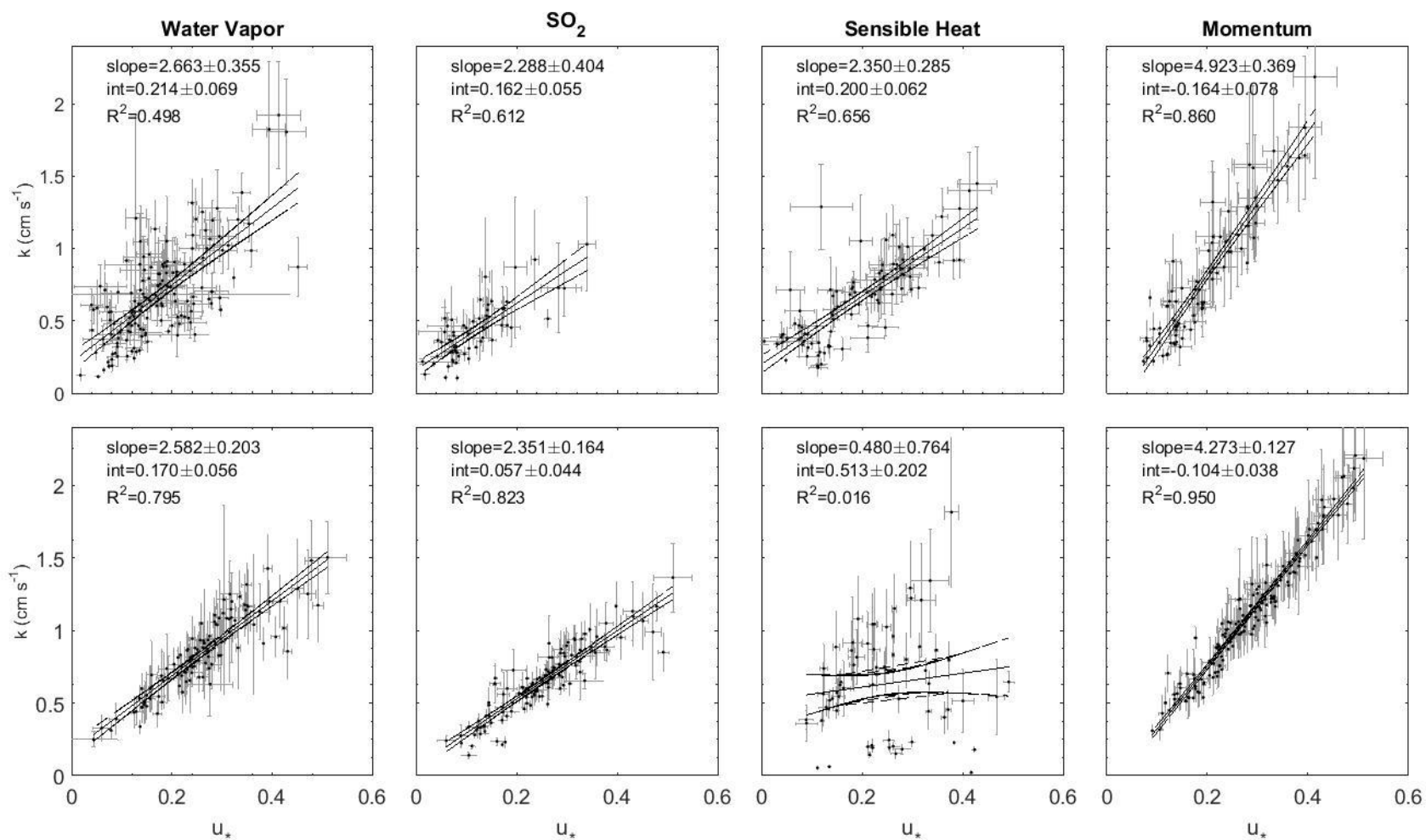
Figure 5.1 Transfer velocities vs friction velocity for water vapor, SO2, sensible heat and momentum measured at Scripps and Duck piers. Top row is the data set from Scripps Pier and the bottom row is the data set from Duck Pier. The solid line is one-way least squares fit to the data and the dotted lines represent 95% confidence interval. The error estimates are 95% confidence bounds.

5.3. Gas transfer coefficient as a function of friction velocity (k vs. u_*)

The data sets from Scripps and Duck show the scalar transfer velocities are positively correlated with u_* (Figure 5.1). The slopes of the regressions of k vs. u_* for the scalar parameters were not significantly different from each other at the 95 % confidence interval. This was true when slopes were compared within and between the data sets. In theory k_{SO2} should be less than k_{H2O} and k_{SH} due to diffusive resistance in the interfacial layer, however, the uncertainty associated with regressions of k vs u_* were too large. Friction velocities are derived from momentum fluxes and are therefore dependent on the co-spectral quality of $\overline{u'w'}$. While friction velocities are useful for the intercomparison between different datasets, wind speeds are a better metric when comparing transfer velocities collected during a single field experiment.

The large scatter in the sensible heat data from Duck precluded meaningful analysis of this data.

5.4. Momentum transfer velocities as a function of friction velocity

The slopes of the regressions of k_{mom} vs u_* were not different from each other between the Scripps and Duck data sets. The slopes of the regression of k_{mom} vs u_* were significantly larger than the slopes of regressions of the scalar parameters. This result was consistent between both data sets

5.5. k_{SO2} vs k_{H2O}

When comparing transfer velocities from simultaneous intervals sulfur dioxide transfer
velocities were less than water vapor transfer velocities for both field studies. The
Scripps data showed k_{SO2}/k_{H2O} = 0.63 ± 0.14 and the Duck data showed k_{SO2}/k_{H2O} =
0.80±0.07. These two slopes were not statistically different from each other at the 95 %
confidence level and both slopes were statistically less than one. The Scripps data had
significantly more scatter than the Duck data and thus the uncertainty in the linear
regression slope was much larger (Figure 5.2). More precise temperature measurements
and a larger data set across a broader range of wind speeds resulted in the high quality of
the Duck data relative to the Scripps data.
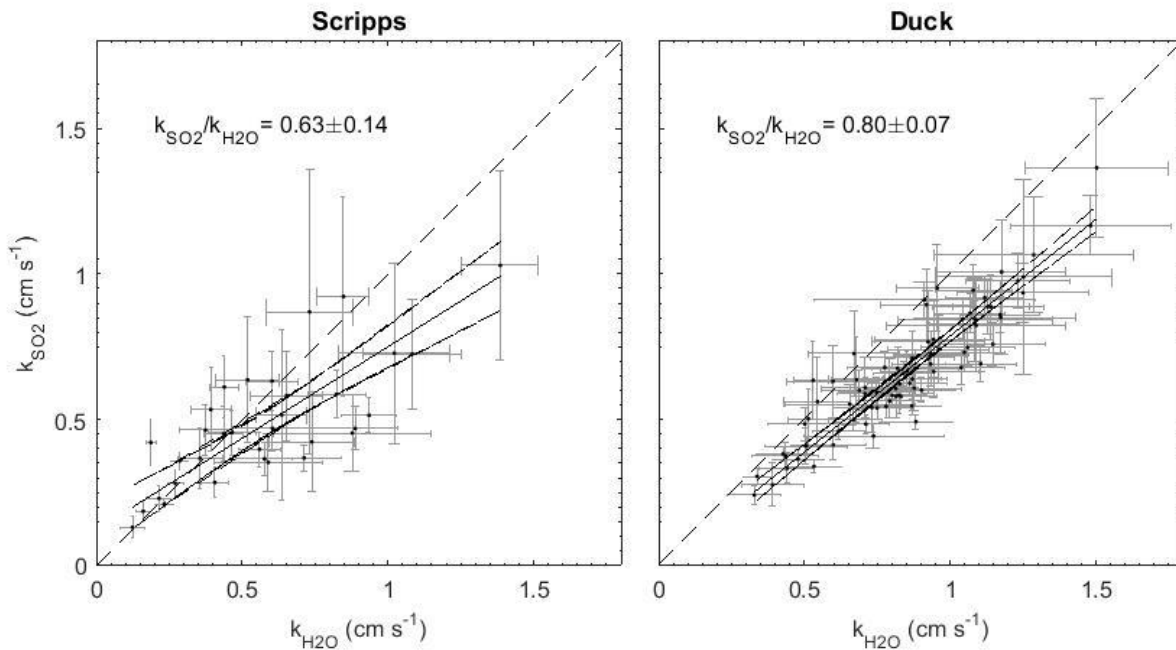
Figure 5.2. Sulfur dioxide transfer velocities plotted against water vapor transfer velocities. The left panel is from the Scripps experiment and the right panel is from the Duck experiment. The solid line is two-way Deming regression to the data and the curved lines represent 95% confidence bounds of the regression. The error estimates are 95% confidence intervals. The dashed line has a slope of one.

5.6. Conclusion

The results of the two field campaigns were consistent in two important aspects. First, the scalar transfer velocities are smaller than those of momentum. This observation ($k_{mom} > k_{scalar}$) can be explained by the fact that diffusive resistance in the interfacial layer affects heat and gases but not momentum. Second, SO_2 transfer velocities are smaller than water vapor transfer velocities for simultaneous measurements. This is also likely explained by

diffusive resistance. Sulfur dioxide diffuses at half the rate of water vapor in the interfacial layer (Reid *et al.,* 1987). The agreement of the two studies increases confidence that these results are meaningful.

The intercomparison between these two datasets also indicated that the overall quality of the Duck data set is significantly better than that of the Scripps data set. This is due to both environmental conditions and improved sensors.

6. Discussion of bulk parameterizations and comparison to experimental results

6.1. Overview

This chapter consists of: 1) a description of previously published bulk parameterizations of

the air/sea gas transfer velocity, 2) a comparison of the Scripps and Duck field results to

bulk gas transfer parameterizations, and 3) an attempt to use the field data to constrain the

magnitude of the diffusive resistance in gas transfer parameterizations.

6.2. Bulk parameterizations of transfer velocities

The bulk transfer equation relates the surface flux to the air/sea concentration differences

in the bulk fluids on either side of the interface (Equation 6.1).

$$F = k_a \left(C_a - \frac{C_w}{H} \right)$$

(6.1)

In Equation 6.1, C_a is the atmospheric partial pressure of a gas (atm), C_w is the molar

concentration in seawater, and H is Henry's law constant (M/atm). In the case of highly

soluble, air-side controlled gases, the transfer velocity is a proportionality constant that

represents the physical transport processes occurring in the turbulent and diffusive layers

in the marine surface layer of the atmosphere. There are several parameterizations that

predict bulk transfer velocities for soluble trace gases over the ocean (Table 6.2). This

section is a comparison between various parameterizations of the bulk transfer velocity

and experimental results. To make these comparisons, experimental values of u_* and C_d

from the Duck and Scripps field campaigns were used to calculate k_{SO2} and k_{H2O} using the

equations in Table 6.2. Diffusion coefficients were calculated for water vapor, SO_2 and heat

at 298 °K following Andreas (2005). Schmidt numbers were calculated by dividing the

kinematic viscosity of air at 298 °K by the diffusion coefficients (Table 6.1).

Table 6.1 Diffusion coefficients and Sc number for water vapor, SO_2 and heat calculated for 298 K° using Andreas (2005)

	SO_2	H_2O	Heat
D ($cm^2 s^{-1}$)	0.128	0.254	0.208
Sc #	1.21	0.61	0.75

Two analyses were conducted using the transfer velocities calculated from model

parameterizations: 1) transfer velocities were plotted against u_* and 2) sulfur dioxide

transfer velocities were plotted against water vapor transfer velocities. Regressions were

applied to the data in each analysis. To compare the parametrizations to the experimental

data the same analysis was conducted using the experimental measurements of transfer

velocities (Figure 6.1-6.2).

The parameterizations from Liss, (1973) and Shahin *et al*. (2002) compute gas transfer

coefficients based on wind speeds and were intended for use in the open ocean. These

parameterizations were converted to utilize friction velocity rather than wind speed, so

they can be compared to the other models and to the coastal experimental results. This

was done by converting wind speeds to friction velocities using the open ocean

parameterization of Smith (1988), (Equations 6.2-6.3).

$$u_* = \frac{U_{10}\kappa}{\log(\frac{z}{z_o})} - \psi(\frac{z}{L}) \qquad (6.2)$$

$$z_o = \frac{\alpha u_*}{g} + \frac{0.11\nu}{u_*} \qquad (6.3)$$

In equations 6.2-6.3, z is measurement height, z_o is roughness length, κ is Von Karman's constant, L is the Obukhov length, g is the acceleration of gravity, ν is kinematic viscosity and α is the Charnock constant which varies from 0.011 to 0.018. The ψ function is the empirical stability function to account for atmospheric stability.

Table 6.2 Commonly used equations for bulk parameterization of soluble trace gas transfer velocity (k).

Reference	k (m s^{-1})
Duce *et al.* (1991)	$\dfrac{u_*}{5Sc^{0.64} + C_d^{-0.5}}$
Fairall *et al.* (1999)	$\dfrac{u_*}{13.3Sc^{0.5} + C_d^{-0.5} - 5 + 1.25\log(Sc)}$
Mackay and Yeun (1983)	$10^{-3} + \dfrac{u_*}{21.65\ Sc^{\frac{2}{3}}}$
Shahin *et al.* (2002)	$10^{-2}D^{0.5}(0.98U_{10} + 1.26)$
Liss (1973)	$0.005 + 0.21U_{10}$
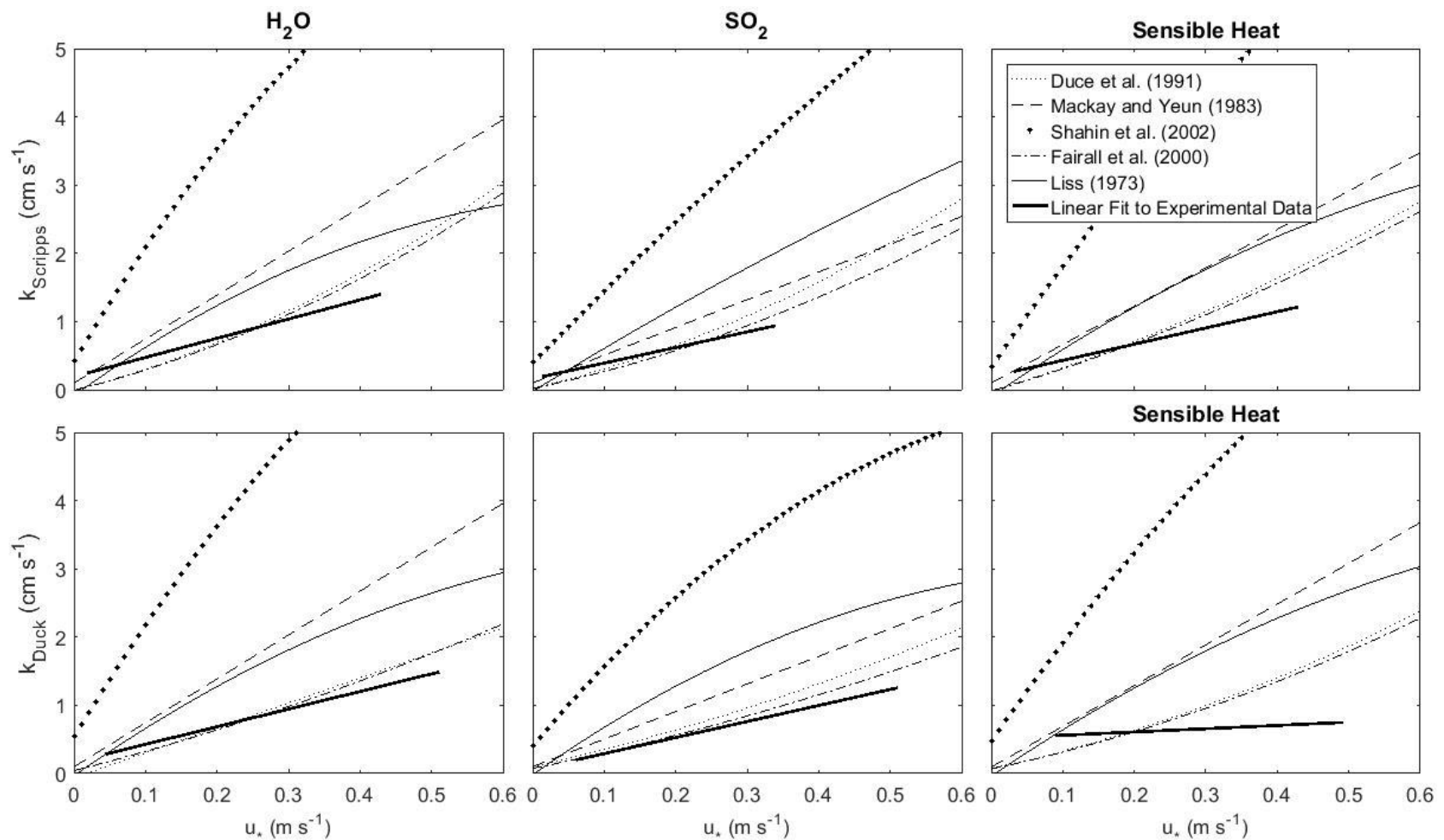
Figure 6.1 Comparison of transfer velocities from field campaigns to bulk parameterizations. Transfer velocities were calculated per the equations in Table 6.1 using experimental measurements of u_* and C_d from Scripps. (Top row) and Duck (Bottom row) pier. The linear regressions of k vs. u_* from the experimental results are shown with the solid black line.
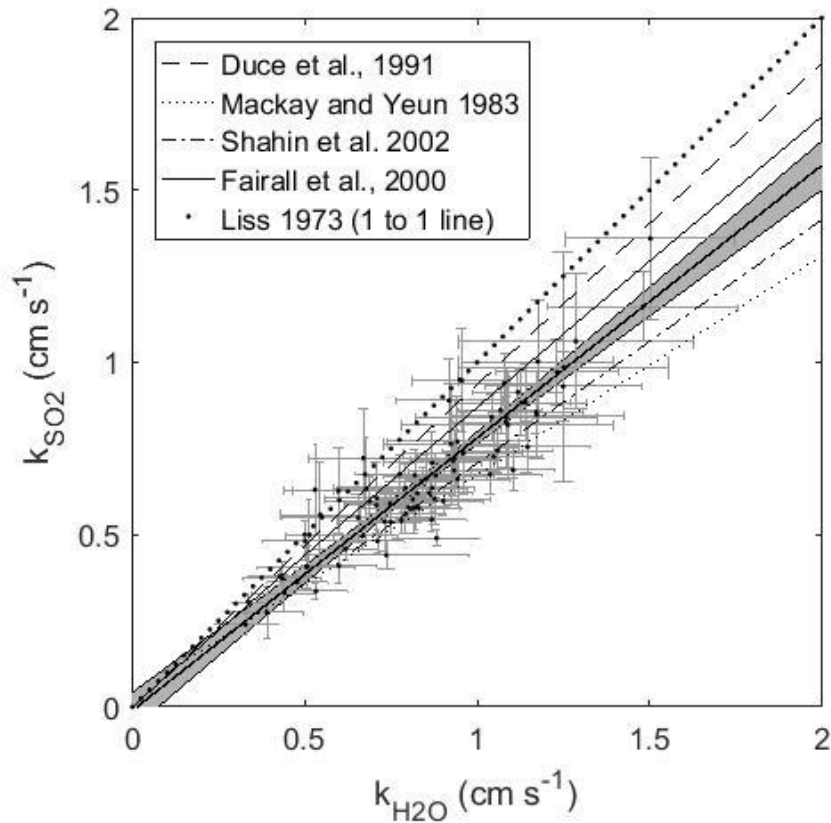
Figure 6.2 Sulfur dioxide transfer velocities plotted against water vapor transfer velocities. The scattered data is from Duck Pier and the grey band is the 95 % confidence bound of the linear regression to the scattered data. The various lines are from the models presented in Table 6.2.

Liss 1973: The Liss (1973) parameterization is based on water vapor flux measurements made in a wind/wave tank. The equation was obtained by fitting a linear regression to measured transfer velocities vs. wind speed. Hence, the parameterization is empirically-derived from laboratory experiments, rather than on a physics-based model of gas transfer. This parameterization overestimated transfer velocities by a large margin for all parameters (Figure 6.1). In general, gas transfer velocities obtained in linear wind/wave tank studies tend to be large relative to those from in situ measurements (Johnson *et al.*,

2010). This is thought to be due to the limited fetch in wind/wave tanks that prevents full

development of the wave field. The Liss (1973) parameterization does not have an explicit

diffusive term and, therefore, has no dependence on diffusion coefficient. As a result, the

ratio k_{SO2}/k_{H2O} is unity (Figure 6.1).

Mackay and Yeun (1983): The parameterization from Mackay and Yeun (1983) is also

based on flux measurements in a wind wave tank. Various gases were dissolved in water

and fluxes were calculated by measuring the change in the concentration of these species

over time.   The equation in this parameterization were obtained from a fitted linear

regression of the measured transfer velocities against $Sc^{-0.67}u_*$. This approach is intended

to account for diffusive behavior. However, the entire transfer velocity is scaled with the Sc

number, which is not consistent with the physical processes believed to control surface

fluxes. Turbulence in the atmospheric surface layer is a significant component of the

overall resistance to gas transfer and does not involve molecular diffusion.

In all the models except Liss (1973), the dependence on diffusivity is scaled with an

exponent less than unity. The theoretical basis for this is the assumption of non-steady

state diffusion from the interfacial layer, for example due to surface renewal (Higbie, 1935;

Slinn *et al.*, 1978; Liu *et al.*, 1979). The exponent of 0.67 in Mackay and Yeun (1983) is

based on measurements of evaporative rates in a closed cell and is not representative of

oceanic conditions (Tamir and Merchuk, 1978).

The parameterization from Mackay and Yeun (1983) overestimated the transfer velocities

for water vapor, SO_2 and sensible heat. As noted above, flux measurements in wind/wave

tank are thought to overestimate transfer coefficients in the oceanic environment. The

102

parameterization from Mackay and Yeun (1983) predicted the ratio k_{SO2}/k_{H2O} =0.64 which was the smallest of any other parameterization and 15 % smaller than the experimental results. The strong diffusive dependence in this model is the result of two factors. Firstly, the exponent on the Sc number is 0.67 which is on the upper end of the range of exponents on existing parameterizations. Secondly, the equation combines the turbulent and diffusive processes into one term which has the effect of over emphasizing the role of diffusive behavior on the transfer velocity.

Shahin et al. (2002): The model from Shahin *et al.* (2002) is based on in situ flux measurements collected on the rooftop of a building in an urban area. Fluxes of HNO_3, SO_2, H_2O and NH_3 were measured in this study using a water surface sampler. The equation was obtained by fitting a linear regression to transfer velocities against wind speed. The transfer velocities for the various gases were normalized by dividing k by $D^{0.5}$. It should be noted again that this approach is not likely to be correct because transfer velocities are expected to be largely dominated by turbulent processes in the bulk layer of the atmosphere which are not related to diffusion. The exponent on the diffusion coefficient is 0.5 in this case, based on various previous studies (Schwarzenbach *et al.*, 1993; Lyman *et al.*, 1990).

The parameterization from Shahin *et al.* (2002) predicted the highest transfer velocities of any parameterization and over-estimated the experimental transfer velocities for all parameters by a significant amount (Figure 6.1). This result is probably because the turbulent characteristics of the atmospheric surface layer in urban areas are significantly different from the marine surface layer. The ratio k_{SO2}/k_{H2O} in the parameterization from

Shahin *et al.* (2002) was 0.71. This result is the second lowest of the models and 10 %

lower than the experimental results.

Duce et al. (1991) and Fairall et al. (1999): The parameterizations from Duce *et al.* (1991)

and Fairall *et al.* (2000) are physically-based models. They are considered together here

because they both model the transfer velocity as the sum of independent resistance terms

representing diffusive and turbulent processes. This contrasts with the parameterizations

from Shahin *et al.* (2002) and Mackay and Yeun (1991) which group the diffusive and

turbulent processes into a single term.

The largest resistance term in these models is turbulent transport in the atmospheric

surface layer, defined as:

$$r_{turb} = k_{mom}^{-1} = \frac{C_d^{-0.5}}{u_*}$$

(6.4)

Diffusive transport in these models have the general form:

$$r_{diff} = \frac{\lambda Sc^m}{u_*}$$

(6.5)

The exponent *m* accounts for non-steady-state diffusion in the interfacial layer and λ is

related to the theoretical height of the interfacial layer. Specifically, λ is the height above

the interface that marks the transition from a linear profile to the log profile of the bulk

atmosphere (Figure 6.3). The linear profile is defined by Equation 6.6 and the log profile is

defined by Equation 6.7, where u^+ and z^+ are dimensionless wind speed and height defined

by Equations 6.8 & 6.9 (Von Karman 1930). Note that in the interfacial layer, the classic

viscosity equation can be derived by substituting z^+ and u^+ from Equations 6.8 & 6.9 into Equation 6.6.

$$u^+ = z^+ \tag{6.6}$$

$$u^+ = \frac{1}{\kappa}\log(z^+) \tag{6.7}$$

$$z^+ = z\left(\frac{u_*}{\mu}\right) \tag{6.8}$$

$$u^+ = \frac{U}{u_*} \tag{6.9}$$

The exponent m is related to the diffusive process in the interfacial layer. The interfacial layer is in contact and exchanges material with the turbulent layer above. The periodic renewal of gas from the turbulent layer prevents a steady state diffusion from being achieved (Figure 6.4). The flux through the interfacial layer under such non-steady-state conditions is described by scaling the *Sc* number with the exponent m (Higbie 1935; Slinn *et al.,* 1978, Liu *et al.,* 1979). The value of m in the models ranges from 0.5 to 0.67 depending on the theoretical framework.
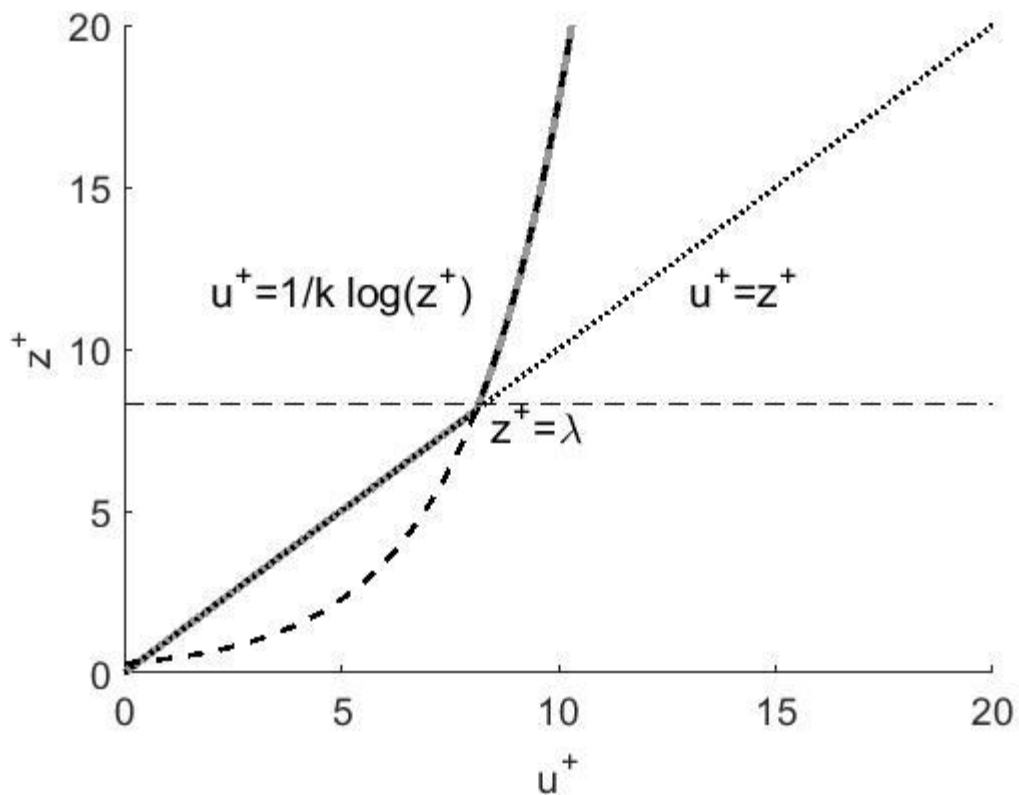
Figure 6.3 Law of the wall (Von Karman 1930). Height vs. wind speed given in dimensionless units. Dimensionless height units (y axis) are defined by Equation 6.8 and dimensionless wind speed (x axis) by Equation 6.9. The thick dotted line is defined by Equation 6.7 and represents the logarithmic profile of the bulk atmosphere. The thick dotted line is defined by Equation 6.6 and represents the linear vertical profile in the interfacial layer. The horizontal thin dotted line is defined as $u^+ = \lambda$, where λ is the height of the interfacial layer above which the profile is defined by the logarithmic profile and below which the profile is linear (grey band).
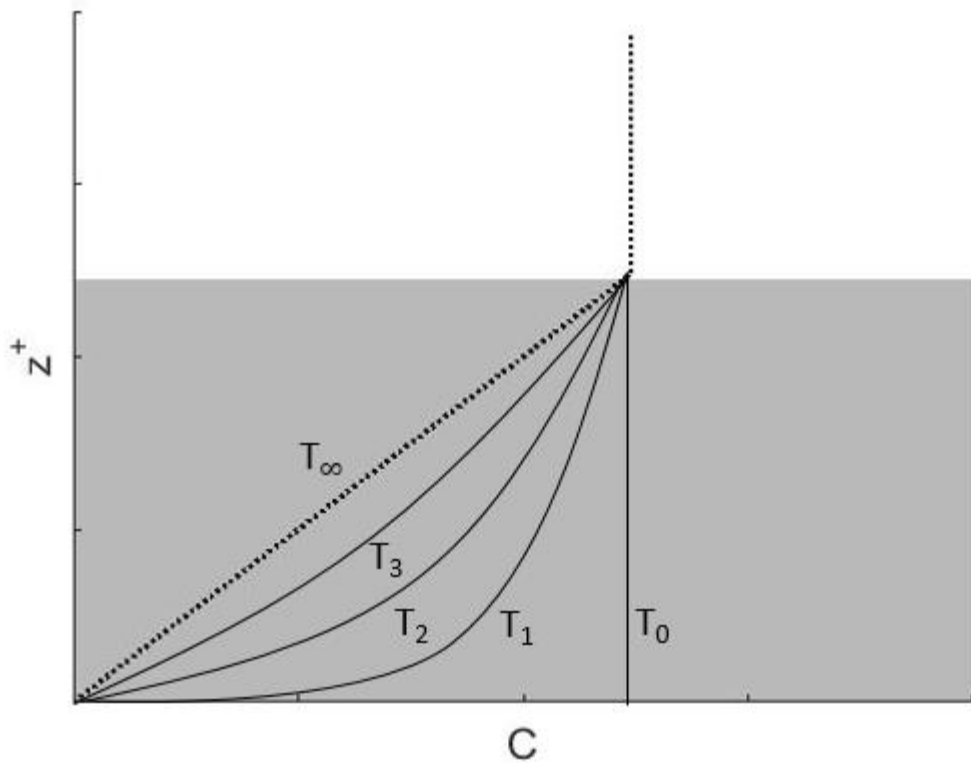
Figure 6.4 Concentration profile in the interfacial layer. The solid black lines show the evolution of the concentration profile starting from time=0 when an air parcel initially contacts the sea surface. The dashed line represents a steady state diffusive concentration profile.

There is little agreement in the literature as to the accepted values of λ and m over the sea surface. The constants $\lambda = 5$ and $m = 0.67$ in the parameterization from Duce *et al.* (1991) are based on Hicks *et al.* (1986), which cites numerous flux studies over land surfaces and in wind tunnels. These studies are summarized in Garratt and Hicks (1973).

The values for λ and m in the parameterization from Fairall *et al.* (1999) are 13.3 and 0.5 respectively, based on surface renewal theory (Liu *et al.*, 1979). Surface renewal theory models the interfacial layer as being intermittently replaced by material from the bulk. A

full discussion of surface renewal theory can be found in Liu *et al.* (1979) and Liu and Businger, (1975). The value of 13.3 is based on Kraus and Businger, (1994) and Soloviev and Schluessel, (1994). Fairall *et al.* (2000) notes that this value is not based on definitive experimental evidence and it remains a major uncertainty in gas transfer parameterizations.

Water vapor transfer velocities calculated from the Duce *et al.* (1991) and Fairall *et al.* (2000) parametrizations were very similar (Figure 6.1). Sensible heat transfer velocities were also similar between these two parameterizations. In contrast, sulfur dioxide transfer velocities calculated from the Fairall *et al.* (2000) parameterization were roughly 12 ± 2 % lower than k_{SO2} calculated from the Duce *et al.* (1991) parameterization. This result is because the Fairall *et al.* (2000) parameterization has a stronger diffusive resistance term than the Duce *et al.* (1991) parameterization. For example, the ratio of k_{SO2}/k_{H2O} from the Duce *et al* model was 0.93 while the ratio was 0.85 from the Fairall *et al.* (2000) parameterization.

The ratio of k_{SO2}/k_{H2O} predicted in the Duce *et al* (1991) and Fairall *et al* (2000) parameterizations were 18 % and 7.6 % higher than the experimental result for the ratio of k_{SO2}/k_{H2O} = 0.80 ± 0.07 from the Duck field experiment.

The Fairall *et al.* (2000) and Duce *et al.* (1991) parametrizations both indicate that transfer velocities increase non-linearly with u_* (Figure 6.1). This non-linearity was not evident in the experimental data for water vapor, SO_2 or sensible heat for either the Scripps or Duck field experiments. The non-linearity in those parameterizations leads to generally underestimating k_{H2O} for values of u_* from 0 to ~ 0.3 and over-estimated k_{H2O} for values of

u_* > 0.3 for the data from Duck Pier (Figure 6.6). The Fairall *et al.* (2000) and Duce *et al.* (1991) parameterizations tended to overestimate k_{SO2} across the entire range of u_* for the data from Duck pier (Figure 6.6). The scatter in the sensible heat data collected at Duck pier is also too large for a meaningful comparison to the parameterizations.

These trends were not clear when comparing these parametrizations to Scripps Pier k_{H2O} and k_{SO2} due to scatter in the data and the limited rang in u_* (Figure 6.5).
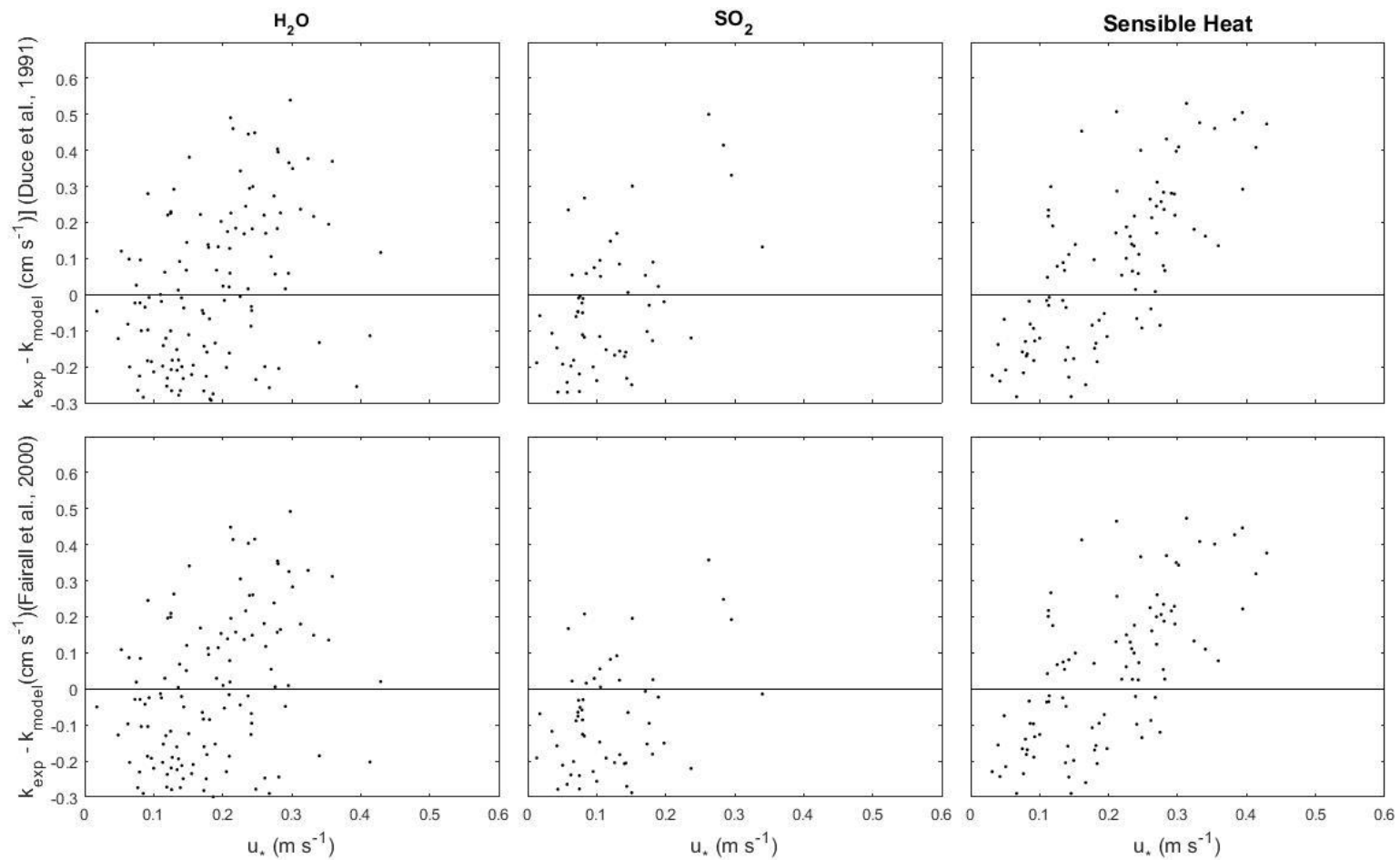
Figure 6.5 (Top row) Difference between transfer velocities from the Duce et al., (1991) parametrizations and the transfer velocities measured at Scripps Pier for water vapor, SO₂ and Sensible heat plotted against u_*. (Bottom row) Difference between transfer velocities from the Fairall et al., (2000) parametrizations and the transfer velocities measured at Scripps Pier for water vapor, SO₂ and Sensible heat plotted against u_*.
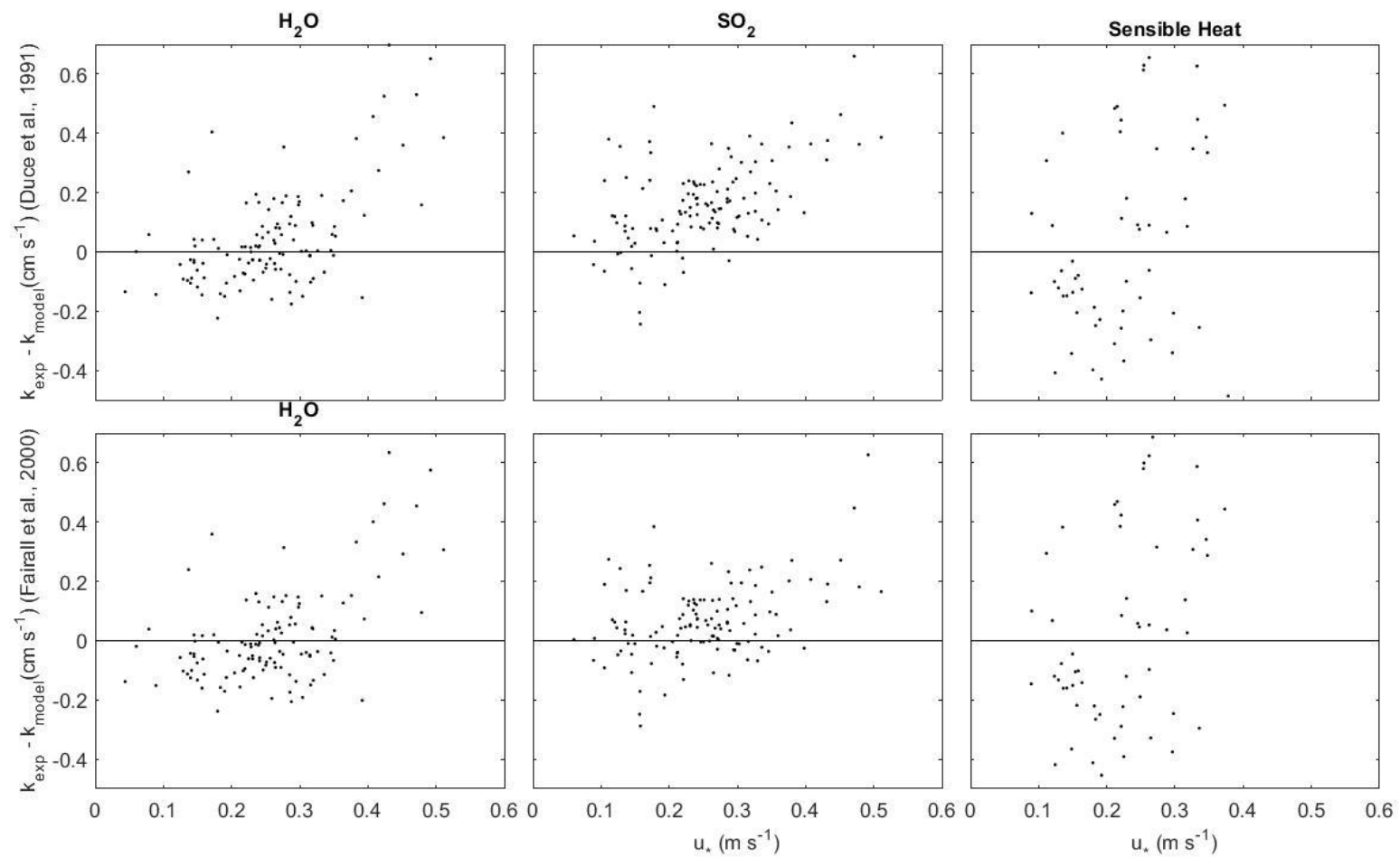
Figure 6.6 (Top row) Difference between transfer velocities from the Duce et al., (1991) parametrizations and the transfer velocities measured at Duck Pier for water vapor, SO2 and Sensible heat plotted against u_*. (Bottom row) Difference between transfer velocities from the Fairall et al., (2000) parametrizations and the transfer velocities measured at Duck Pier for water vapor, SO2 and Sensible heat plotted against u_*.

6.3. Constraining diffusive resistance

In principle, the experimental field measurements can be used to constrain the scaling of

diffusive resistance in the physically-based gas transfer parameterizations (Duce *et al.*,

1991, Fairall *et al.*, 2000). An analysis was performed to explore the extent to which the

experimental results from Duck Pier constrain the value of λ and m in the models. This was

done by systematically varying the values of λ and m in the COARE and Duce *et al.* (1991)

parameterization equations, applying the values to the experimental conditions for the

Duck and Scripps data sets, and comparing the predicted values of k_{SO2} and k_{H2O} to the

experimental values. This comparison was done using the correlation coefficient (R),

calculated as follows:

$$R = \left(1 - \frac{SS_{res}}{SS_{tot}}\right)^{0.5} \tag{6.10}$$

$$SS_{res} = \sum_{i}(k_{observed}^{i} - k_{predicted}^{i})^{2} \tag{6.11}$$

$$SS_{tot} = \sum_{i}(k_{observed}^{i} - \bar{k}_{observed})^{2} \tag{6.12}$$

where $k_{observed}$ are the transfer velocities measured at Duck Pier and $k_{predicted}$ are transfer

velocities calculated from Fairall *et al.* (2000) or Duce *et al.* (1991). The overbar denotes

the mean value and i is the number of data points. Three separate analysis were

performed, 1) A comparison between k_{H2O} observed and k_{H2O} predicted, 2) a comparison

between k_{SO2} observed and k_{SO2} predicted and 3) a comparison between $k_{observed}$ and $k_{predicted}$

including both k_{SO2} and k_{H2O} simultaneously as one dataset. These three comparisons were

performed for both the Duce *et al.* (1991) and Fairall *et al.* (2000) parameterizations (Figures 6.7 & 6.8).
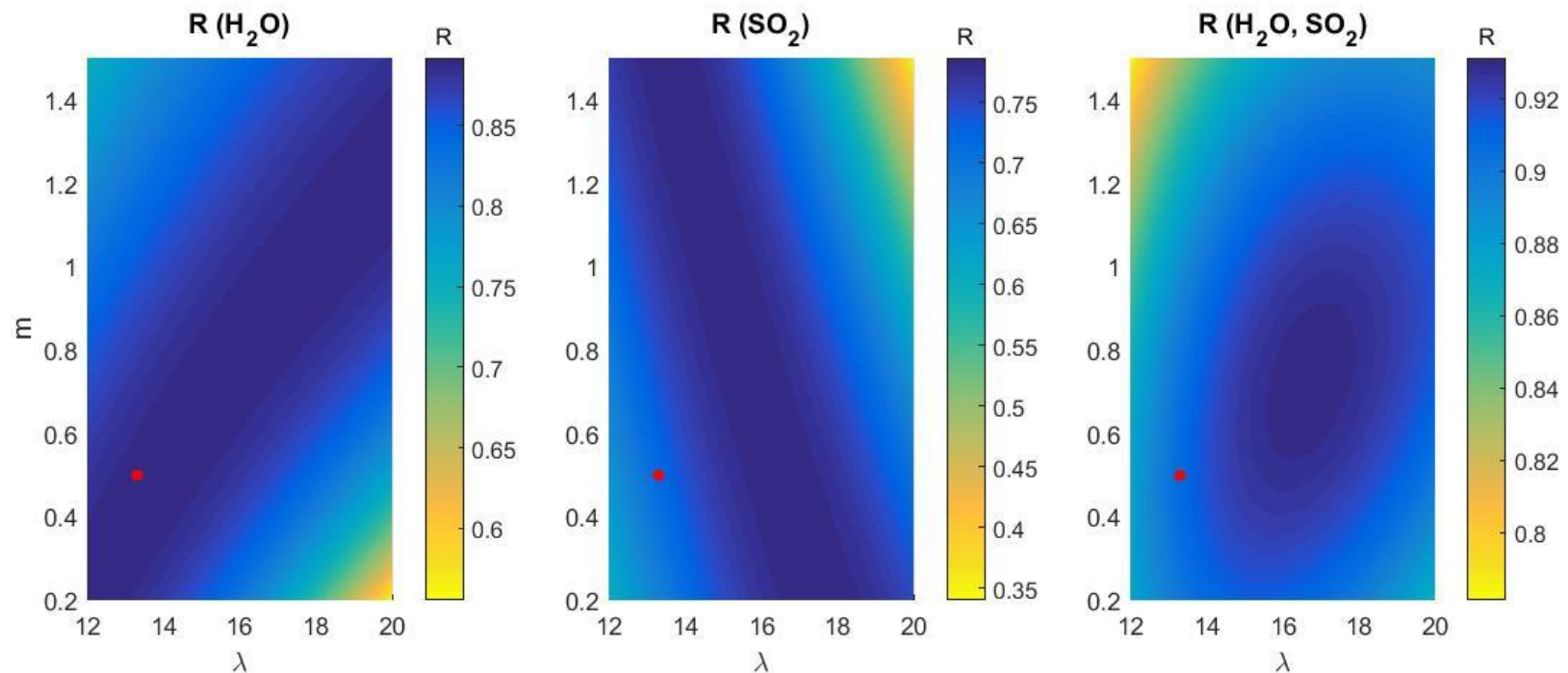
Figure 6.7 Contour plot of the coefficient of determination (R) for the comparison between experimental measurements of k from the Duck field study, and predicted values of k from the Fairall *et al*. (2000) parameterization. Left panel: coefficient of determination for parameterizations and experimental measurements of k_{H2O}, Center panel: coefficient of determination for parameterizations and experimental measurements of k_{SO2}, Right panel: coefficient of determination for parameterizations and experimental measurements of both k_{H2O} and k_{SO2}. The red dot shows the values of λ and m in the Fairall *et al*. (2000) model. Note the color scales are different for each subplot.
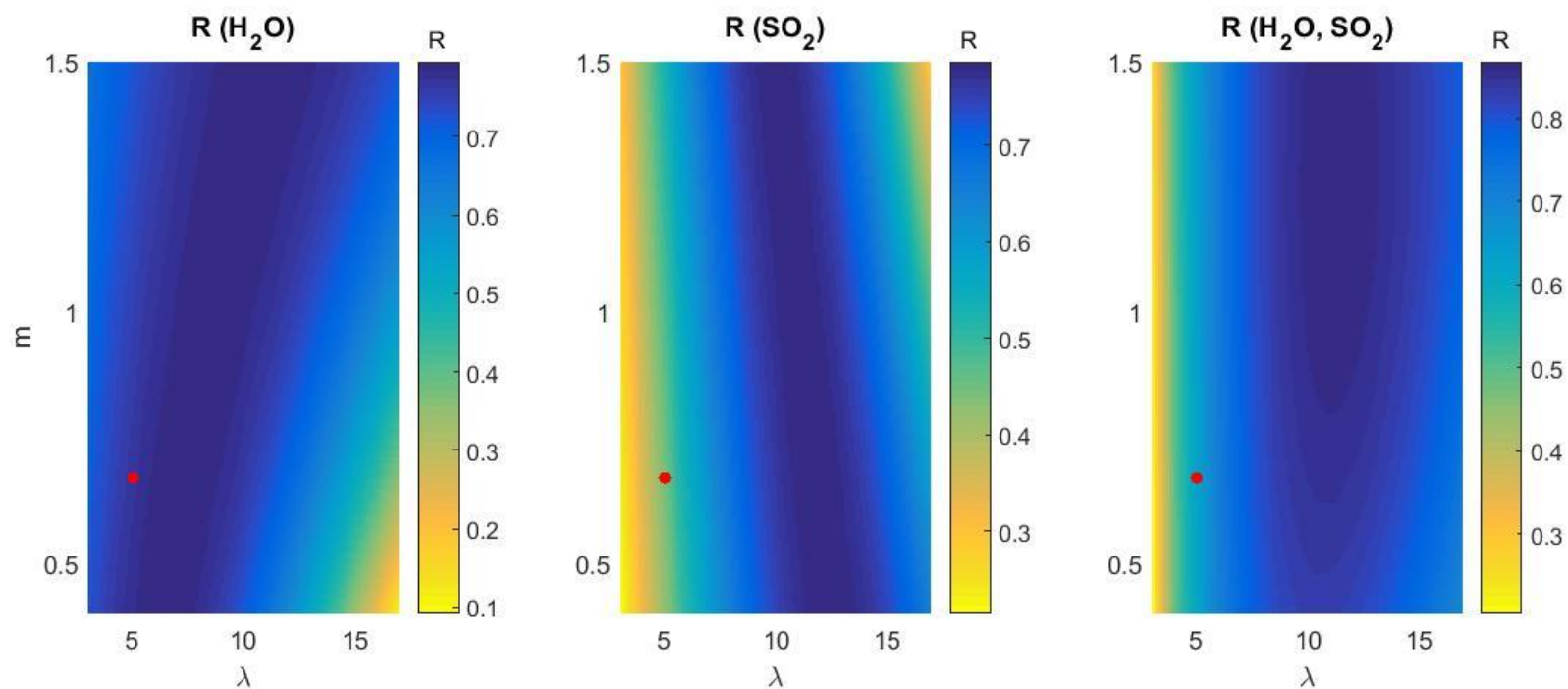
Figure 6.8 Contour plot of the coefficient of determination (R) for the comparison between experimental measurements of k from the Duck field study, and predicted values of k from the Duce *et al.* (1991) parameterization. Left panel: coefficient of determination for parameterizations and experimental measurements of k_{H2O}, Center panel: coefficient of determination for parameterizations and experimental measurements of k_{SO2}, Right panel: coefficient of determination for parameterizations and experimental measurements of both k_{H2O} and k_{SO2}. The red dot shows the values of λ and m in the Duce *et al.* (1991) model. Note the color scales are different for each subplot.

Comparison between Fairall et al. (2000) and experimental results

The comparison between observed and predicted k_{H2O} calculation yielded a "ridge"-shaped band of maxima in R, indicating a positive roughly linear relationship between λ and m (Figures 6.7). The actual values of the parameters given by Fairall *et al*. (2000) (λ=13.3 and m=0.5) were well within the 90% significance contours for the correlation coefficient ($\sim$ 0.2). This result is not surprising considering the Fairall *et al*. (2000) parameterization is tuned to fit water vapor flux measurements.

For sulfur dioxide, a similar "ridge"-shaped band of maxima was obtained, but in this case, it indicated an inverse relationship between λ and m (Figure 6.7). The actual values of λ and m were again well within the critical values of the correlation coefficient at the 95% confidence interval. The "ridge" of high correlation coefficient for the analysis comparing k_{SO2} from Fairall *et al*. (2000) and experimental measurements did not pass through λ=13.3 and m=0.5. This result indicates the Fairall *et al*. (2000) parameterization over-estimated k_{SO2}, which is consistent with the analysis comparing the regressions of k_{SO2} vs u_* from the parameterization and experimental results (Figure 6.1).

The correlation coefficients calculated when considering both k_{SO2} and k_{H2O} simultaneously resulted in a clear maximum when λ=16.6 and m=0.71 (Figure 6.7 panel 3). These values are larger than the COARE parameterizations values for λ and m which are 13.3 and 0.5 respectively. This result indicates the diffusive resistance in the interfacial layer is stronger than the COARE algorithm suggests. However, the values of λ and m in the COARE parametrization are well within the range of λ and m defined as $R < R_{critical}$ (95 %

confidence) meaning there is no statistical significant difference between the results of this analysis and the COARE parameterization (Figure 6.7).

Comparison between Duce et al. (1991) and experimental results

The analysis comparing k from the Duce *et al.* (1991) parameterization to experimental measurements had similar features to the analysis of the Fairall *et al.* (2000) parameterization. The band of high R for the comparison between experimental and predicted k_{H2O} did not exactly pass through λ=5 and m=0.67 (red dot in Figure 6.8), which are the values used in the Duce *et al.* (1991) parameterization but was relatively close compared to the k_{SO2} comparison. The maximum R-value was 0.86 when λ=11.1 and m=1.23 (Figure 6.8). These values are larger than the original values in the Duce *et al.* (1991) parameterization which are 5 and 0.67 for λ and m respectively. A value of m =1.47 would indicate diffusion rates faster than steady state conditions which is not physically possible.

7. Conclusions

Our knowledge of the physical processes controlling soluble trace gas deposition to the sea surface is limited and based almost entirely on micrometeorological theory and data for water vapor and sensible heat. In situ measurements of trace gas deposition to the sea surface have only recently become possible and this thesis represents one of the first such studies. The lack of trace gas deposition studies over the ocean contrasts with the much larger database for trace gas deposition to land surfaces.

The goal of this study was to determine if SO_2 fluxes are, 1) a plausible approach to studying air-side control and 2) in agreement with bulk parameterizations derived from water vapor flux measurements. This chapter is a brief overview of the outcomes of this study, what was learned about the physics controlling trace gas deposition, and the prospects for future work.

7.1. SO_2 as a tool for studying air/sea trace gas exchange

Real-time measurements of deposition of SO_2 to the sea surface were made in this study. These measurements represent a significant expansion of the current available soluble trace gas flux dataset. The quality of the SO_2 flux data is superior that of the more commonly measured latent and sensible heat fluxes. Thus, SO_2 flux measurements are a new tool for the study of soluble trace gas fluxes. The ability to measure deposition with increased precision using SO_2 fluxes will reduce the uncertainties in air-side transfer velocity calculations.

This work represents the first time in situ flux measurements have been used to quantify diffusive resistance in the air/sea interfacial layer. Understanding microphysics at the air/sea interface has a global scale impact considering the large quantity and variety of soluble gases in the atmosphere that exchange across the air/sea interface. The ability to measure diffusive resistance in the marine boundary layer is a fundamental step in formulating and testing physically based parametrizations of the transfer velocity. Such parametrizations must be able to predict fluxes of gases spanning a range of molecular diffusivities.

7.2. Future research goals related to soluble trace gas flux measurements

This study demonstrated the feasibility of SO_2 air/sea flux measurements, but it was limited in terms of both the quantity of data and the range of environmental conditions sampled. As a result, the diffusive resistance in model parameterizations could not be constrained with statistical confidence. Future studies should make these measurements; 1) across a broader range of wind speeds and 2) of gases spanning a broad range of diffusion rates. Such studies would improve our ability to constrain the diffusive resistance in model parameterizations.

Flux studies of soluble gases are highly challenging because of a lack of suitable analytical methodology and instrumentation to make high sensitivity, high frequency measurements. Specifically, compounds like nitric acid, ammonia, organic acids are air-side controlled and play a major role in biogeochemical cycles and climate. The instrumentation and methodology to measure fluxes of these gases needs to be developed and deployed in the field.

The transfer velocities derived from the SO_2 fluxes from this study were in reasonable agreement with existing bulk flux parameterizations derived from water vapor flux. The results of this work do not justify an adjustment of the strength of the diffusive resistance in the COARE parameterization. The current COARE parameterization is adequate for use in global chemistry models. Furthermore, it is unlikely that further work focusing on SO_2 flux measurements will result in drastic reconsiderations of global flux estimates of water vapor and latent heat.

Despite this there is a strong argument for continuing to make soluble trace gas flux measurements. For example, it cannot be assumed that SO_2 flux measurements are a suitable proxy for other soluble trace gases which may have different reaction kinetics, surface chemistry or liquid side chemistry. For example, the studies by Yang *et al.* (2013) and Marandino *et al.* (2005) suggested bulk seawater concentrations of VOC's have no impact on the air/sea concentration differential driving the flux. This result is in direct contradiction to all existing physical models. Furthermore, the fundamental physics probed in this study can be useful in other aspects of gas transfer research. One such example is the deposition of particles to the air/sea interface which is thought to be a highly diffusive driven process.

8. References

Andreas, Edgar L. (2005). "Handbook of Physical Constants and Functions for Use in Atmospheric Boundary Layer Studies." *Cold Regions Research and Engineering Laboratory* M-05-1.

Bandy, A. R., Scott, B. W., Blomquist, S. M., & Thorton, D.C. (1992). Low Yields of SO_2 from Dimethyl Sulfide Oxidation in the Marine Boundary Layer. *Geophysical Research Letters*, 19(11), 1125–1127.

Bowles, M. W., Mogollón, J. M., Kasten, S., Zabel, M., & Hinrichs, K. (2014). Global Rates of Marine Sulfate Reduction and Implications for Sub – Sea-floor Metabolic Activities. *Science*, 344(6186), 889–892.

Buckley, M. P., & Veron, F. (2016). Structure of the Airflow above Surface Waves. *Journal of Physical Oceanography*, *46*(5), 1377–1397. http://doi.org/10.1175/JPO-D-15-0135.1

Charlson, R. J., Lovelock, J. E., Andreae, M. O., & Warren, S. (1987). Oceanic Phytoplankton, Atmospheric Sulphur, Cloud Albedo and Climate. *Nature*, *326*, 655–661.

Clark, A. G., & Radojevic, M. (1984). Oxidation Rates of SO_2 in Sea-water and Sea-salt Aerosols. *Atmospheric Environment*, 18(12), 2761–2767.

De Bruyn, W. J., Dahl, E., & Saltzman, E. S. (2006). DMS and SO_2 Measurements in the Tropical Marine Boundary Layer. *Journal of Atmospheric Chemistry*, 53, 145–154. https://doi.org/10.1007/s10874-005-9000

Donelan, M. A., Curcic, M., Chen, S. S., & Magnusson, A. K. (2012). Modeling Waves and Wind Stress. *Journal of Geophysical Research: Oceans*, *117*(7), 1–26. http://doi.org/10.1029/2011JC007787

Donelan, M. A., Haus, B. K., Reul, N., Plant, W. J., Stiassnie, M., Graber, H. C., Brown, O. B., Saltzman, E. S. (2004). On the Limiting Aerodynamic Roughness of the Ocean in Very Strong Winds. *Geophysical Research Letters*, *31*(18), 1–5. http://doi.org/10.1029/2004GL019460

Duce, R. A., Liss, P. S., Merrill, J. T., Atlas, E. L., Hicks, B. B., Miller, J. M., Prospero J. M., Arimoto, R., Church, T. M., Ellis, W., Galloway, J. N., Hansen, L., Jickells, T. D., Knap, A. H. Reinhardt K. H., Schneider, B., Soudine, A, Tokos, J. J., Tsunogai, S., Wollast, R., Zhou, M. (1991). The Atmospheric input of Trace Species to the World Ocean. *Global Biogeochemical Cycles*, *5*(3), 193–259.

Edson, J. B., Jampana, V., Weller, R. A., Bigorre, S. P., Plueddemann, A. J., Fairall, C. W., Miller, S. D., Mahrt, L., Vickers, D., Hersbach, H. (2013). On the Exchange of Momentum Over the Open Ocean. *Journal of Physical Oceanography*, *43*(8), 1589–1610. http://doi.org/10.1175/JPO-D-12-0173.1

Fairall, C. W., Bradley, E. F., Rogers, D. P., Edson, J. B., & Young, G. S. (1996). Bulk Parameterization of Air-sea Fluxes for Tropical Ocean- Global Atmosphere Coupled-Ocean Atmosphere Response Experiment. *Journal of Geophysical Research*, *101*, 3747–3764.

Fairaill, C. W., Hare, J. E., Edson, J. B., McGillis, W. (2000). Parameterization and Micrometeorological Measurement of Air–Sea Gas Transfer. *Boundary-Layer Meteorology*, *96*(1), 63–105. http://doi.org/10.1023/A:1002662826020

Faloona, I., Conley, S. A., Blomquist, B., Clarke, A. D. Kamustin, V., Howell, S., Lenschow, D. H. Bandy, A. R. (2009) Sulfur Dioxide in the Tropical Marine Boundary Layer: Dry Deposition and Heterogeneous Oxidation Observed During the Pacific Atmospheric Sulfur Experiment. *Journal of Atmospheric Chemistry*. 63, 13–32.

Gallagher, M. S., King, D. B., Whung, P., & Saltzman, E. S. (1997). Performance of the HPLC/fluorescence SO_2 Detector During the GASIE Instrument Intercomparison Experiment. *Journal of Geophysical Research*, *102*(D13), 16,247-16,254.

Garbe, C., & Jahne, B. (2002). Measuring the Sea Surface Heat Flux and Probability Distribution of Surface Renewal Events. *Gas Transfer and Water Surfaces; Geophysical Monograph*, (3), 109–114.

Garratt, J. R., & Hicks, B. B. (1973). Momentum, Heat and Water Vapour Transfer to and from Natural and Artificial Surfaces. *Quarterly Journal of the Royal Meteorological Society*, *99*, 680–687.

Hicks, B. B., & Wesely, M. L. (1986). Proceedings of the NAPAP Workshop on Dry Deposition. Oak Ridge, Tenn: NOAA.

Hicks, B. B. (1972). Some Evaluations of Drag and Bulk Transfer Coefficients Over Water Bodies of Different Sizes. *Boundary-Layer Meteorology*, *3*(2), 201–213. http://doi.org/10.1007/BF02033919

Higbie, R. (1935). The Rate of Absorption of a Pure Gas into a Still Liquid During Short Periods of Exposure. *Transcripts of the American Institute of Chemical Engineers*.

Hoover, T. E., & Berkshire, D. C. (1969). Effects of Hydration on Carbon Dioxide Exchange across an Air-Water Interface. *Journal of Geophysical Research*, 74(2), 456–464.

Johnson, M. T. (2010). A numerical Scheme to Calculate Temperature and Salinity Dependent Air-water Transfer Velocities for any Gas. *Ocean Science*, *6*(4), 913–932. http://doi.org/10.5194/os-6-913-2010

Kaimal, J. C., Wyngaard, J. C., Izumi, Y., Cote, O. R. (1972). Spectral Characteristics of Surface-layer Turbulence. *Quarterly Journal of the Royal Meteorological Society.*, *98*, 563–589.

Kelly, R. T., Tolmachev, A. V, Page, J. S., Tang, K., & Smith, R. D. (2011). The Ion Funnel: Theory, Implementations and Applications. *Mass Spectrum Rev*, *29*(2), 294–312. http://doi.org/10.1002/mas.20232.

Kondo, J. (1975). Air-sea Bulk Transfer Coefficients in Diabatic Conditions. *Boundary-Layer Meteorology*, *9*, 91–112.

Kraus, E. B., & Businger, J. A. (1994). Impact of the Waves on the Sea Surface Roughness Length under Idealized Like-Hurricane Wind Conditions (Part II). *Atmosphere-Ocean Interaction* (2nd ed.). Oxford University Press.

Liss, P. S. (1973). Processes of Gas Exchange Across an Air-water Interface. *Deep-Sea Research*, *20*(3), 221–238. http://doi.org/10.1016/0011-7471(73)90013-2

Liss, P. S., & Slater, P. G. (1974). Flux of Gases Across the Air-Sea Interface. *Nature*, *247*.

Liu, W. T., & Businger, J. A. (1975). Temperature Profile in the Molecular Sublayer Near the Interface of a Fluid in Turbulent Motion. *Geophysical Research Letters*, *2*(9), 403–404. http://doi.org/10.1029/GL002i009p00403

Liu, W. T., Katsaros, K. B., & Businger, J. A. (1978). Bulk Parameterizatio of Air-sea Exchanges of Heat and Water Vapor Including the Molecular Constraints at the Interface. *Journal of the Atmospheric Sciences*, *36*, 1722–1735.

Lyman, W. J., Reehl, W. F., & Rosenblatt, D. H. (1990). Handbook of Chemical Property Estimation Methods: Environmental Behavior of Organic Compounds. Washington DC.: American Chemical Society.

Mackay, D., & Yeun, A. T. K. (1983). Mass Transfer Coefficient Correlations for Volatilization of Organic Solutes from Water. *Environmental Science and Technology*, *17*(4), 211–217. http://doi.org/10.1021/es00110a006

Marandino, C. A., De Bruyn W.J., S. D. Miller, M. J. Prather, and Saltzman E.J. 2005. "Oceanic Uptake and the Global Atmospheric Acetone Budget." *Geophysical Research Letters* 32:1–4. Retrieved August 20, 2014 (http://doi.wiley.com/10.1029/2005GL023285).

Millero, F. J., Hershey, J. P., Johnson, G., & Zhang, J.-Z. (1989). The Solubility of SO_2 and the Dissociation of H_2SO_3 in NaCl Solutions. *Journal of Atmospheric Chemistry*, *8*, 377–389.

Monin, A. S., & Obukhov, A. M. (1954). Basic Laws of Turbulent Mixing in the Surface Layer of the Atmosphere. *Contributions of the Geophysical Institute, Academy of Sciences. USSR*, *24*(151), 163–187.

Pond, S., Fissel, D. B., & Paulson, C. A. (1974). A Note on Bulk Aerodynamic Coefficients for Sensible Heat and Moisture Fluxes. *Boundary-Layer Meteorology*, *6*(1–2), 333–339. http://doi.org/10.1007/BF00232493

Reid, R. C., Prausnitz, J. M., and Poling, B. E. (1987). The Properties of Gases and Liquids, McGraw-Hill, Inc., New York.

Sander, R. (1999). Compilation of Henry ' S Law Constants for Inorganic and Organic Species of Potential Importance in Environmental Chemistry (Version 3). http:\\www.mpch-mainz.mpg.de\~sander\res\henry.html

Schwartz, S. E., Freiberg, J. E. (1981). Mass-transport Limitation to the Rate of Reaction of Gases in Liquid Droplets: Application to Oxidation of SO_2 in Aqueous Solutions. *Atmospheric Environment*, *15*(7), 1129–1144.

Schwarzenbach, R. P., Gschwend, P. M., & Imboden, D. M. (1993). Environmental Organic Chemistry. New York: Wiley Interscience.

Shahin, U. M., Holsen, T. M., & Odabasi, M. (2002). Dry Deposition Measured with a Water Surface Sampler: A Comparison to Modeled Results. *Atmospheric Environment*, *36*(20), 3267–3276. http://doi.org/10.1016/S1352-2310(02)00315-1

Sharqawy, M. H., Lienhard, J. H., Zubair, S. M. (2010). Thermophysical Properties of Seawater: A Review of Existing Correlations and Data. *Desalination and Water Treatment*, *16*, 354–380. http://doi.org/10.5004/dwt.2010.1079

Slinn, W. G. N., Hasse, L., Hicks, B. B., Hogan, A. W., Lal, D., Liss, P. S., Munnich, K. O., Sehmel, G. A., Vittori, O. (1978). Some Aspects of the Transfer of Atmospheric Trace Constituents Past the Air-sea Interface. *Atmospheric Environment*, *12*, 2055–2087.

Smith, S. D. (1988). Coefficients for Sea Surface Wind Stress, Heat Flux, and Wind Profiles as a Function of Wind Speed and Temperature. *Journal of Geophysical Research: Oceans*, *93*(C12), 15467–15472. http://doi.org/10.1029/JC093iC12p15467

Soloviev, A. V., & Schlüssel, P. (1994). Parameterization of the cool skin of the ocean and the air-ocean gas transfer on the basis of modeling surface renewal. *American Meteorological Society*, *24*, 1339–1346.

Tamir, A., & Merchuk, J. C. (1978). Effect of Diffusivity on Gas-side Mass Transfer Coefficient. *Chemical Engineering Sciences*, *33*, 1371–1374.

Thorton, D. C., Bandy, A. R., Tu, F. H., Blomquist, B., Mitchell, G. M., & Nadler, W. (2002). Fast airborne sulfur dioxide measurements by Atmospheric Pressure Ionization Mass Spectrometry (APIMS). *Journal of Geophysical Research*, *107*(D22). http://doi.org/10.1029/2002JD002289

Von Karman, T. (1930). Mechanische Ahnlichkeit and Turbulenz. *Nachrichten von Der Gesellschaft Der Wissenschaften Zu Gottingen*, *5*, 58–76.

Worsnop, D. R., Zahniser, M. S., Kolb, C. E., Gardner, J. A., Watson, L. R., Van Doren, J. M., Jayne, J. T., Davidovits, P. (1989). Temperature Dependence of Mass Accommodation of SO_2 and H_2O_2 on Aqeous Surfaces. *Journal of Physical Chemistry*. 1159–1172.